UNIVERSITÀ DEGLI STUDI DI SALERNO

Dipartimento di Fisica "E. R. Caianiello"

Corso di Dottorato XXXV Ciclo in Matematica, Fisica ed Applicazioni

Ph.D. Thesis in Physics

Transition Metal Dichalcogenides and Carbon Nanomaterials in Field Effect Devices and Photodetectors

Academic Year 2021/2022

Tutor:

Prof. Antonio Di Bartolomeo

Ph.D. Coordinator:

Prof. Patrizia Longobardi

Candidate:

Aniello Pelella

A thesis submitted in fulfilment of the requirements for the degree of Doctor of Philosophy

Contents

Introduction

This PhD thesis focuses on the electronic and optoelectronic characterization of devices based on low-dimensional materials and on a first approach to fabrication of 2D transition metal dichalcogenide (TMD) field effect transistors (FETs) and heterostructures. The aim of this research is to investigate the properties of several low-dimensional materials and how they can be affected by light, electron irradiation, and electric field. These effects can be also exploited for some applications, from simple photodetection to a new generation of transistors based on tuneable field emission current.

This work is structured into three chapters. In the first chapter, the fundamentals of devices, like FETs and Schottky diodes, are presented together with the state-of-the-art of some of the most studied low-dimensional materials, i.e. TMDs, graphene, and carbon nanotubes.

The other two chapters are focused on the results obtained during my three PhD years.

In particular, the second chapter is about TMD FETs. Molybdenum disulphide (MoS_2) is one of the most studied TMDs in literature. Nevertheless, the study of MoS_2 FET electron beam influence was something unreported. During the characterization of the materials, the scanning electron microscope (SEM) is a powerful tool to check the material flakes' morphology and to have full control in contacting the device. For this reason, a study about the role of electron beam irradiation is of great interest, especially if it causes dramatic changes in the material's conductivity[1] (***ACS Appl. Mater. Interfaces 2020, 12, 36, 40532–40540***).

On a similar device, field emission properties have been investigated. Using the Fowler-Nordheim theory, MoS_2 flakes show a low turn-on field which can be modulated by applying different voltages at the gate oxide under them. This behaviour can be exploited for the realization of new

generation transistors based on field emission phenomenon[2] (***Adv. Electron. Mater. 2021, 7, 2000838***).

In the second chapter, another TMD FET has been studied: Platinum diselenide FET. Among all the results, surely the coexistence of positive and negative photoconductivity is something unusual and of a great interest. Incident light increases its conductivity when it is in high vacuum (positive photoconductivity), while, in ambient pressure, the n-doping induced by the desorption of surface adsorbates prevails and decreases conductivity (negative photoconductivity)[3](***Adv. Funct. Mater. 2021, 31, 2105722***).

In the third Chapter, the focus shifts to carbon-based Schottky diodes and TMD heterostructures for photodetection. The fabrication of graphene-silicon Schottky diodes often involves the formation of a parallel metal-insulator-semiconductor (MIS) structure. This MIS structure affects the reverse current of the device, inducing a deviation (kink) from the standard current-voltage characteristic, because of a tunneling phenomenon occurring through the insulator[4] (***ACS Appl. Mater. Interfaces 2021, 13, 40, 47895–47903***). To exploit this structure behaviour, a platinum-titanium/Silicon junction has been fabricated in parallel to a MIS structure formed by carbon nanotubes (CNTs), silicon nitride (Si_3N_4) and bulk n-type Silicon. This device shows the same kink in the reverse current. However, when irradiated by light either on the MIS or the diode, the device shows a different photocurrent, also depending on the applied voltage bias. This behaviour can lead to different applications, from a voltage bias tuneable photodetector to a logic Boolean device with the position of the light and the applied bias as input variables[5] (***Adv. Electron. Mater. 2022, 2200919***).

Finally, in the last part of the third chapter, some examples of FET and heterostructures fabrication are reported. During the PhD course, I spent 6 months (Oct2021-Apr2022) in Aachen, Germany, at

the RWTH University, under the supervision of Prof. Max Lemme. During those months, I have learnt how to fabricate standard 2D field effect transistors and 2D TMD heterostructures. For instance, I show, in the last part of this work, some tungsten diselenide (WSe$_2$) FETs with an on/off ratio up to 10^5 and some MoS$_2$/WSe$_2$ heterostructures with a responsivity of about $1\mu A/W$.

1. Low-Dimensional Materials: Properties and Applications

1.1. Graphene

Graphene is a two-dimensional material formed by carbon atoms sp^2 bonded and arranged in a honeycomb lattice (**Figure 1.1(a-b)**). Each C atom is σ-bonded to three neighbours, while the fourth bond is z-oriented forming a π-bond. The remaining pz-electron per atom, not involved in the covalent bonding, is delocalized over the whole graphene lattice, and it is responsible for the electric conductivity. The hybrid $sp2$ bonds are responsible for the graphene's peculiar properties. The crystal lattice of graphene is formed by two triangular lattices (A and B) shifted with respect to each other, defining the hexagonal honeycomb array. Isolated graphene was first discovered in 2004 by Geim and Novoselov[6,7], using mechanical exfoliation, a simple technique that can be easily accessible to everyone. Owing to the strong covalent bonds, graphene has an extraordinary mechanical strength[8,9].

A plot of the graphene band structure is reported in **Figure 1.1(c)**. The energy dispersion is plotted as a function of the momentum kx and ky in a 3D plot. The energy-momentum relation was first calculated by Wallace in 1947[10] using the tight-binding approximation. The obtained $E(\boldsymbol{k})$ relation (see **Equation(1.4)** below) is plotted in **Figure 1.1(c)**, underlining a linear behaviour of the energy for small $k = (k_x, k_y)$ near to the Dirac points (K, K'). A magnification of the Dirac cone is reported in **Figure 1.1(d)**, showing a gapless band structure and highlighting the linear dispersion for small momenta. The linear-like behaviour is indicative of the fact that the charge carriers behave like relativistic particles with high Fermi velocity $v_F \sim 10^6 \; m/s$.
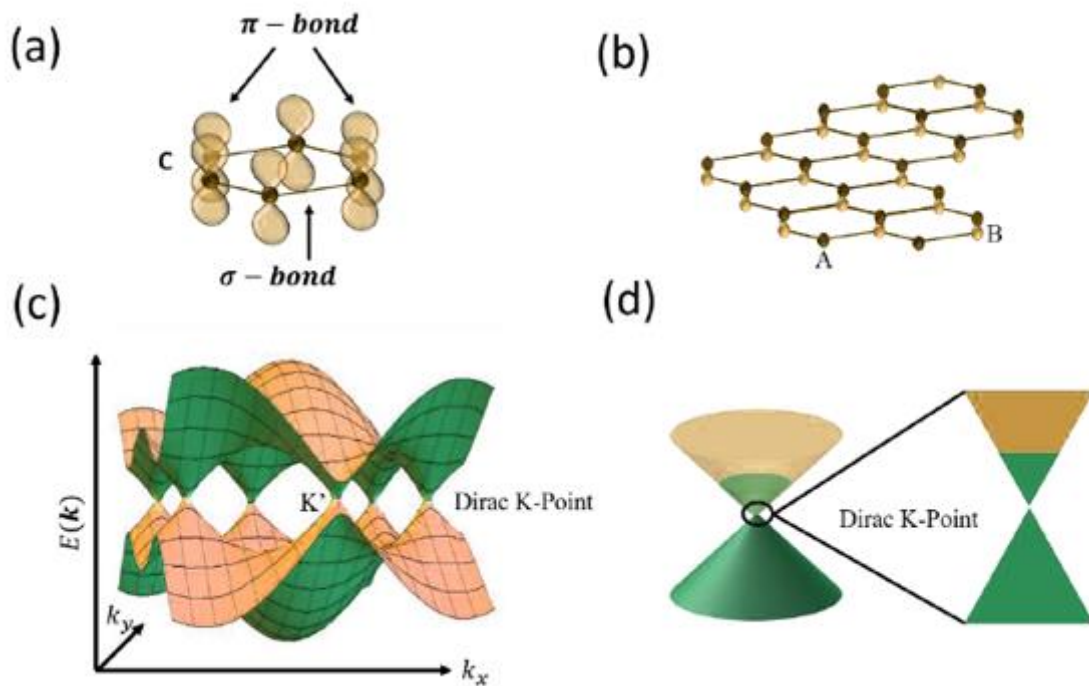
Figure 1.1 *– **(a)** Carbon atom orbitals. **(b)** Graphene honeycomb structure. **(c)** Graphene band structure. **(d)** Dirac cone and Dirac k-point graphic representation.*

The gapless structure and the possibility to change the doping through the Fermi level position make graphene very intriguing for applications in nanotechnology. For instance, given the 2D nature of graphene-based devices, they can be fabricated with a very thin channel (thickness of ~3Å for single-layer graphene). This constrains the electrons and holes to move in the plane, giving rise to extraordinary properties and diminishing the short-channel effects. Also, considering the peculiar band structure, in field effect transistor applications, graphene shows an ambipolar behaviour, dominated by a p-type and n-type conduction at negative and positive gate voltage[11], with carrier mobilities estimated up to $200.000 \ cm^2 V^{-1} \ s^{-1}$. The ambipolar conduction can be an important feature for complementary logic applications; however, the limited on/off ratio caused by the absence of intrinsic bandgap is a significant obstacle and requires delicate material

engineering for real applications[12,13]. Anyway, graphene is an excellent material for electronic devices not only for its high electron mobility, but also for its electric current carrying capacity ($\sim 10^8$ A/cm^2 on SiO$_2$/Si substrate)[14], high thermal conductivity ($\sim 5 \times 10^3$ Wm^{-1}K^{-1} for suspended graphene)[15], record mechanical strength (Young's modulus is~ 1 TPa)[9], resilience to high temperatures (melting temperature estimated as 4510K)[16] and humidity[17,18], resistance to molecule diffusion and chemical stability.

Graphene is also an ideal material for sensing applications: compared to any other material, it offers the largest detecting area, which favours interaction with the ambient. Further, as it is naturally compatible with thin film processing, graphene is easy to integrate into existing semiconductor device technologies. It is readily scalable, has low contact resistance with most common metals such as Ti, Cr, Ni, and Pa ($\sim 100\Omega\mu m$ contact resistance has been reported for Ni and Pa[19–22]), and can form rectifying junctions with several semiconductor materials. The graphene–semiconductor Schottky junction is one of the simplest conceivable devices in a hybrid graphene–semiconductor technology.

1.2. Carbon Nanotubes

In 1991 Iijima discovered carbon nanotubes (CNTs) in the soot created in an electric discharge between two carbon electrodes[23]. CNTs are arranged in hexagons and pentagons which are made up of carbon atoms with a diameter of 3–15 nm. CNT is the subfamily of the fullerene, which is its carbon allotropes, which was discovered by Kroto et al. in 1985[24]. The name is gotten from its size where the diameter of a nanotube is a request of a couple of nanometers. These are enormous macromolecules that are idiosyncratic in their size, shape, and properties. Carbon nanotubes are light since they are entirely made of the light element carbon (C). They are strong and have excellent elasticity and flexibility. In fact, carbon fibers are used to make tennis rackets, for

example. Their main advantages in this regard are their high chemical stability as well as their strong mechanical properties.

CNTs structure is a hollow cylindrical structure (**Figure 1.2(a)**), which is framed by the moving of single or multiple layers of graphene sheets (**Figure 1.2(b)**). Rely upon the quantity of the outer layer or wall CNTs are for the most part in two kinds that are single-single-walled carbon nanotubes (SWNTs) and multi-walled carbon nanotubes (MWNTs). When a graphene sheet is rolled at specific and separate angles then a proper structure of nanotube will be formed with a fixed inner radius. Due to the roll of a graphene sheet, by itself it forms various allotropes of carbon.

The term single-walled carbon nanotubes (SWNTs) were first described in 1993[25]. SWNTs are a single layer of graphene sheet with a diameter of 1–2 nm. **Figure 1.2(c)** shows the surface and internal view of an SWNT.

Multi-walled carbon nanotubes are made up of two or more nanotubes, distinguished from each other and whit the outer tubes enclosing the inner tube. Due to the presence of various rolled layers of graphene sheet, MWNTs have a diameter ranging from 2 to 50nm. The inner layer radius of the tube is 0.34 nm and the outer layer radius ranges from 2 nm up to 20–30 nm[26]. Depending on the presence of graphene sheets MWNTs are named and numbered too. **Figure 1.2(d)** shows the surface and internal view of multiwall carbon nanotubes.
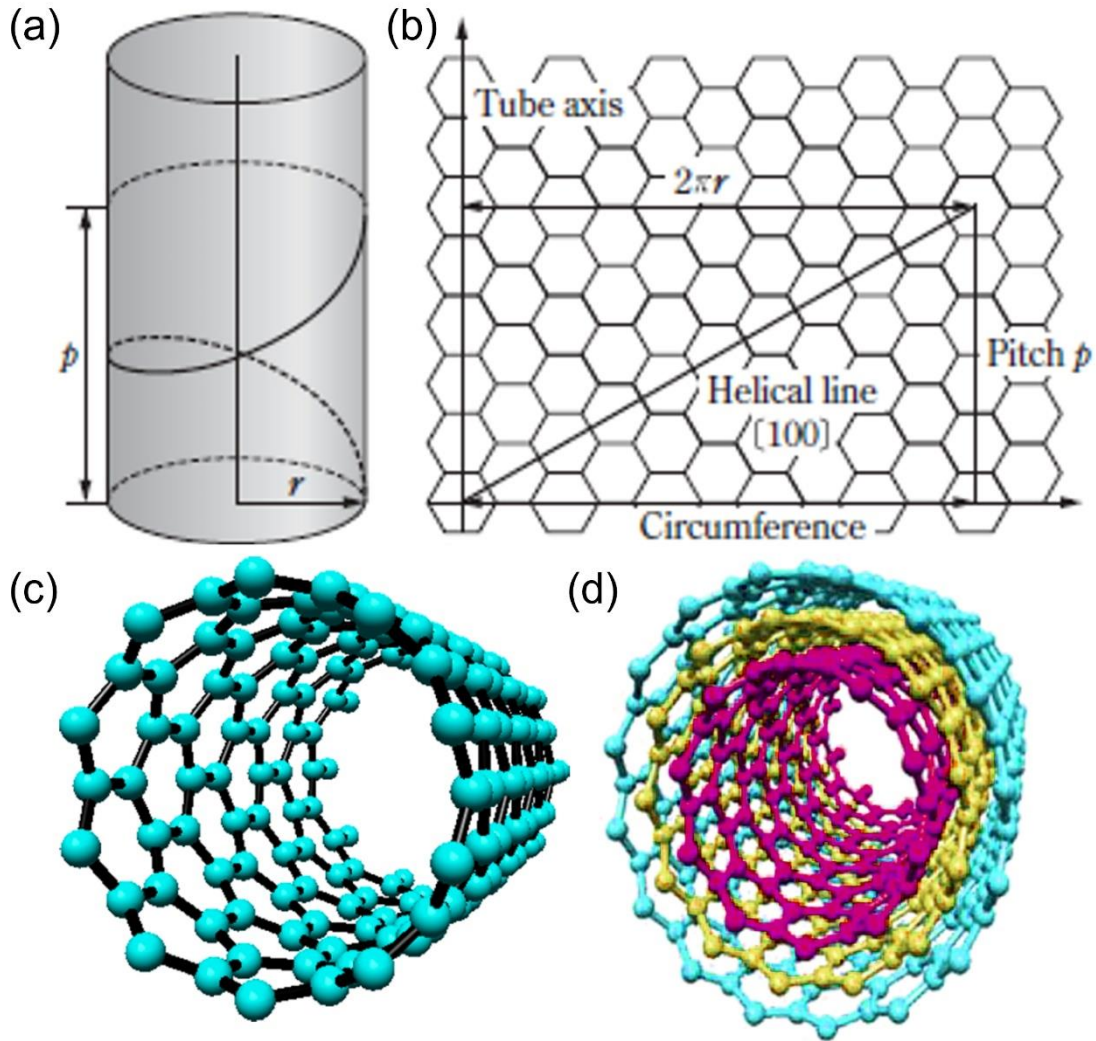
Figure 1.2 - *Schematic diagram showing (a) a helical arrangement of graphitic carbons and (b) its unrolled plane. The helical line is indicated by the heavy line passing through the centers of the hexagons. (c) Surface and Internal view of single-walled carbon nanotube and (d) a multiwall carbon nanotube.*

1.2.1. Chirality

As we are aware that CNT is nothing but a modified version of the graphene sheet, so to understand the CNT structure we should start from the structure of graphene. The graphene sheet shown below **Figure 1.3(a)** is the one plane sheet from graphite. Graphene lattice is formed by two basis vectors a_1 and a_2. The basis vectors are defined as $a_1 = a(\sqrt{3}, 0)$ and $a_2 = a(\sqrt{3}/2, 3/2)$ with $|a1| = |a2| = \sqrt{3}a$, where a is the $C-C$ bond length of value of $0.142\ nm$.

Carbon nanotubes can be classified into three main families, depending on the way the graphene sheet is folded. Each nanotube is defined by a chiral vector:

$$C = na_1 + ma_2 \equiv (n, m) \qquad\qquad (1.1)$$

Chirality is the main feature to know the electrical properties of CNTs. For, m = 0, the structure will be zigzag on the nanotubes. For n = m, instead, the nanotubes will show the armchair structure. For generic values of (n,m), the nanotube is just called chiral. The names zigzag and armchair refer to the arrangement of the carbon atoms along the circumference of the nanotube. CNT is a cylindrical structure which is forms after cutting the graphene sheet into the rectangular strip. The process of conversion of rectangular graphene sheet to a zigzag, armchair and chiral structure CNT is reported below in **Figure 1.3(b)**. Finally, **Figure 1.3(c-d-e)** show some examples of chiral, armchair, and zigzag nanotubes.

The chiral angle ϑ is defined as the angle between vector a_1 and vector C. It is possible to express ϑ in terms of integers n and m:

$$cos\vartheta = \frac{2m + m}{2\sqrt{n^2 + m^2 + nm}} \qquad\qquad (1.2)$$

where $\vartheta = 0$ and $\vartheta = 30°$ correspond to zigzag and armchair nanotubes respectively. The diameter of the nanotube, d, is given by:

$$d = \frac{a_c}{\pi}\sqrt{3}(n^2 + nm + m^2)^{\frac{1}{2}} \qquad\qquad (1.3)$$

where a_c is the distance between adjacent carbon atoms in the hexagonal lattice.
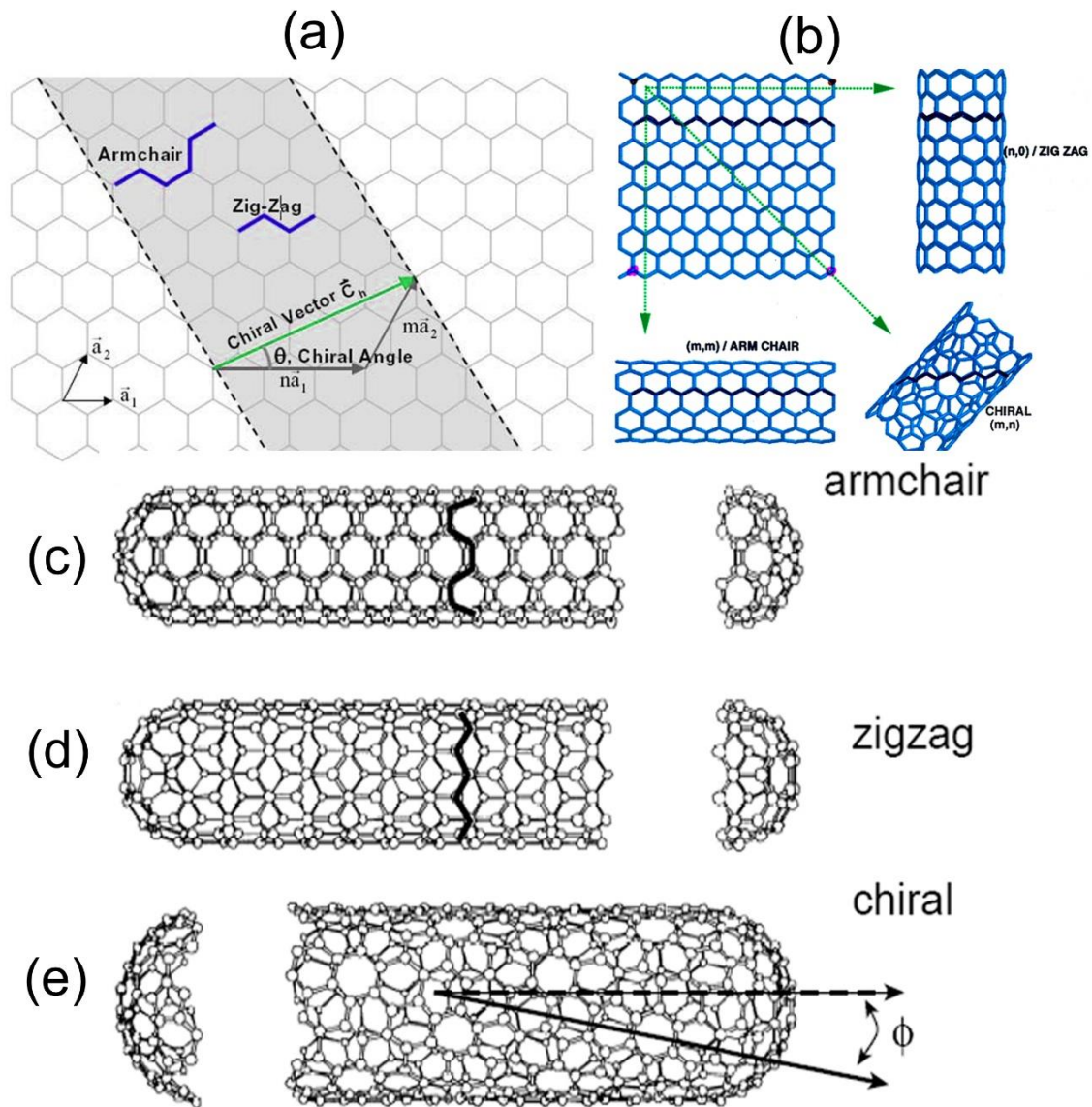
Figure 1.3 – **(a)** *Schematic representation of graphene sheets with chiral vector (n, m) and chiral angle ϑ.* **(b)** *Strip of a graphene sheet rolled into a tube.* **(c)** *Armchair chirality with (n,m) = (5,5).* **(d)** *zigzag chirality with (n,m) = (9,0).* **(e)** *Chiral nanotube with (n,m) = (10,5).*

1.2.2. CNTs' Electronic Structure

The electronic one-dimensional structure of carbon nanotubes can be derived from that of a two-dimensional graphene sheet with periodic boundary conditions along the direction of the nanotube circumference[27]. **Figure 1.4(a-b)** show the graphene lattice in real and reciprocal space. The shaded areas correspond to the unit cell and the first Brillouin zone.
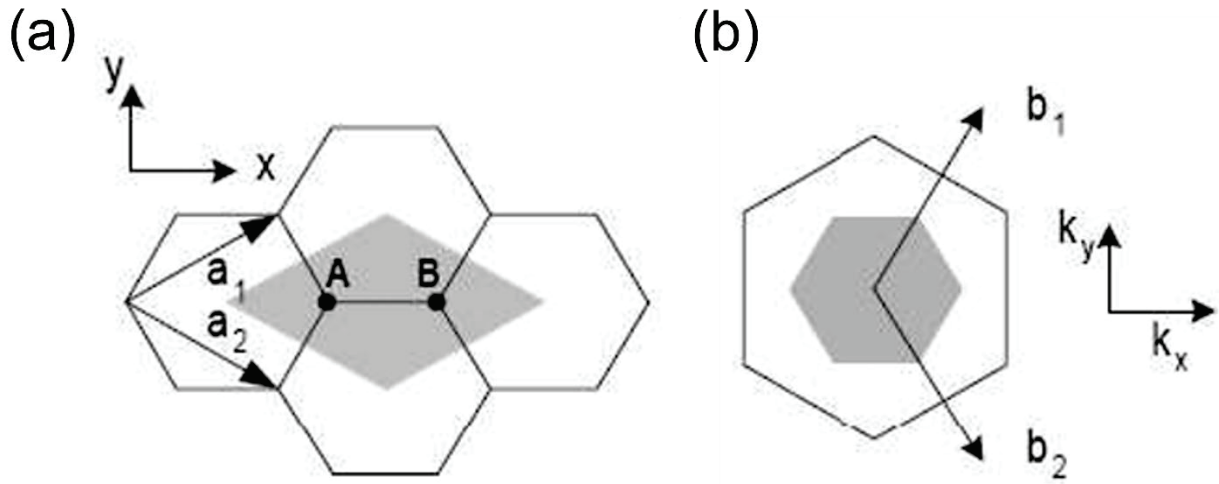
Figure 1.4 - *Fragments of graphene in real (a) and reciprocal (b) space. The shaded areas correspond to the unit cell and the Brillouin area. a_i and b_i (i = 1,2) are respectively the basis vectors and the vectors of the reciprocal lattice.*

Carbon atoms have four valence electrons: three of them form a strong sp^2 bond, while the other one occupies a π orbital, perpendicular to the graphene lattice. Since π bonds are much weaker than σ bonds, the electronic properties of graphite and carbon nanotubes can be determined by considering only π electrons. The energy dispersion for π electrons in a graphene sheet is[27]:

$$E\left(k_x, k_y\right) = \pm\gamma_0 \left[1 + 4\cos\left(\frac{\sqrt{3}k_x a}{2}\right)\cos\left(\frac{k_y a}{2}\right) + 4\cos^2\left(\frac{k_y a}{2}\right)\right]^{1/2} \qquad (1.4)$$

where γ_0 is the integral energy of superposition between the closest neighbors. **Figure 1.5** is the 3D representation of the energy dispersion that results in the bonding and antibonding bands. The lower and upper bands degenerate at the corners of the first Brillouin zone, called K points. At 0 K, the lower band is completely occupied, and the upper band is empty, this makes graphene a 'zero gap' conductor.
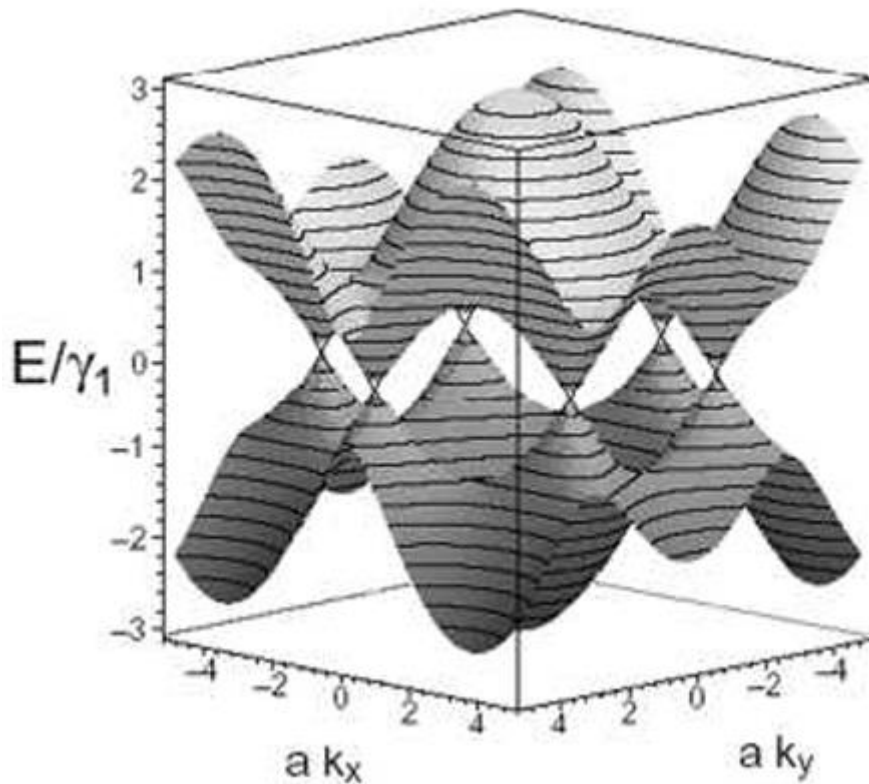
Figure 1.5 - *Dispersion energy for graphite[28]. The lower and upper bands meet at the K points.*

The band structure of carbon nanotubes can be detected by imposing periodic boundary conditions along the tangential. The amount of energy available in the direction of the circumference is quantized as:

$$k * C = 2\pi q (q = 0,1,2, \dots) \qquad\qquad (1.5)$$

Due to this quantization, a fair number of equidistant parallel lines appear, representing the modes of k allowed in the reciprocal space. **Figure 1.6(a-b)** show the quantized reciprocal space for an armchair nanotube and a zigzag nanotube. Energy dispersion for π electrons in carbon nanotubes is obtained by taking sections along the k lines in the diagram of **Figure 1.6**.

If for a particular nanotube (n,m) one of these lines passes through the point K of the two-dimensional Brillouin zone, the nanotube is metallic. Otherwise, there will be a gap between the valence and conduction bands and the nanotube is therefore semiconductor.
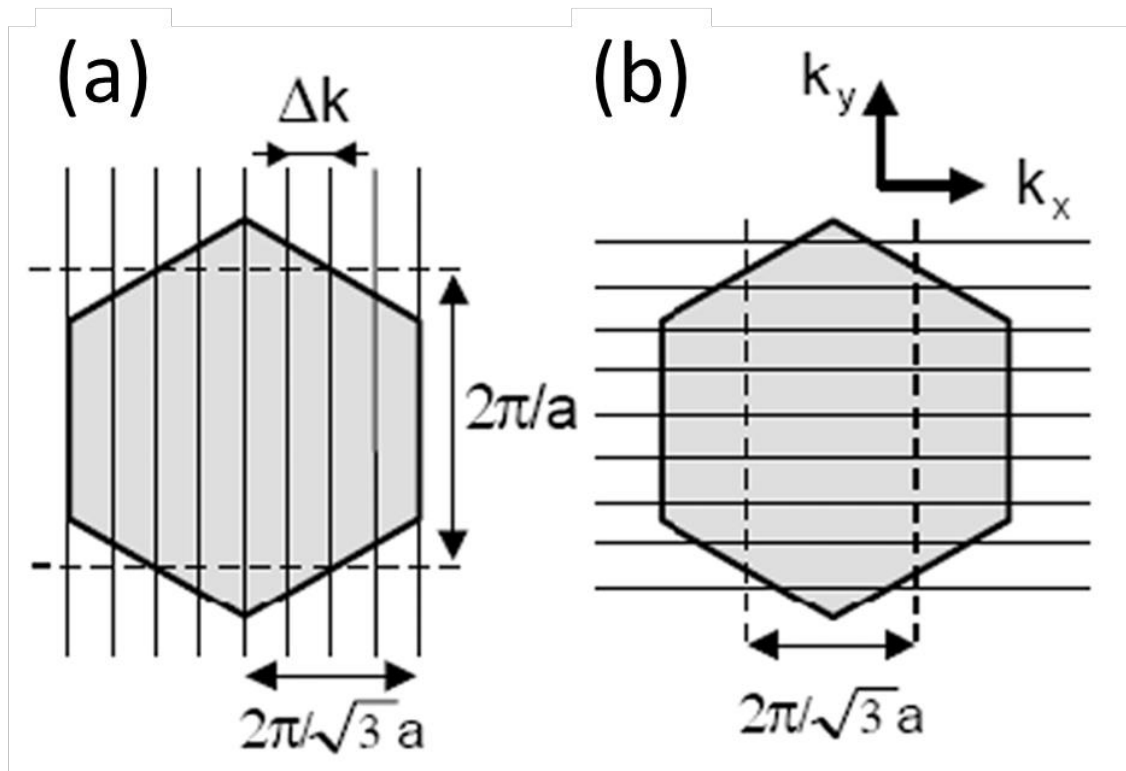
Figure 1.6 - *Reciprocal space for an armchair* *(a)* *and a* *(b)* *zigzag nanotube. The parallel lines represent the values of k.*

It can be shown that the electronic properties of carbon nanotubes are dependent on the structural parameters: they can be metallic or semiconductor depending on their diameter and their chirality. A nanotube is metallic if (n,m) is a multiple of 3. Moreover, Armchair nanotubes (n,n) are always metallic and that the zigzag ones (n,0) are metallic only if n is a multiple of 3. Therefore, about one third of the CNTs are metallic and the other two thirds are semiconductors. It is also shown that the gap of a semiconductor nanotube is inversely proportional to its diameter. Calculations indicate that large nanotubes (diameter > 15 nm) are always metallic whatever their chirality[27].

In the case of multi-walled carbon nanotubes, each concentric cylinder can be seen as a single-walled nanotube, with its own chirality. For nanotubes less than 15 nm in diameter, one third of these will be metallic. When the diameter is larger than 15 nm, the gap of the semiconductor

nanotubes becomes so small that the nanotubes at room temperature can be considered metallic[29]. In MWNTs, all concentric cylinders with a diameter greater than 15 nm will be conductive.

1.3.   Transition Metal Dichalcogenides

The group 16 of the periodic table, chalcogen elements, is extremely reactive to large number of metals, defining a plethora of different combinations of metal chalcogenides defined by various stoichiometric ratios. The transition metal chalcogenides (TMDs) are described by the chemical formula MX_2, where M is a transition metal (Mo, W, V, Nb, Ti, Pt, Pd etc.) and X a chalcogen (S, Se, Te).

Either semiconducting or metallic, TMDs basic block consists in a sandwiched structure (see **Figure 1.7(a-d)**) based on two main configuration H-phase or T-phase (see **Figure 1.7(b-e)**), where a transition metal atomic layer is wrapped by two chalcogen atomic layers. Each layer is bonded to another by van der Waals forces, which permits an easy exfoliation of the bulk material. The *X-M-X* atoms, instead, are covalently bonded[30].

Independently on the electrical nature of the material, the two main configurations are the H-phase and the T-phase. Both phases consist of two tetrahedron (**Figure 1.7(b-e)**) arranged symmetrically (or 180° rotated) respect to the M atom (or TM as labelled in the figure, yellow ball) at the vertex. The blue balls, at the vertices, represent the chalcogen atoms. The two structures form a trigonal prismatic (octahedral) configuration which describes the H (T) phase. A top view representation of the hexagonal crystal lattice is shown in **Figure 1.7(c-f)**, for both phases.

The physical properties of the material, i.e. the band diagram, the electrical conduction, the optical properties, the metal or semiconducting nature, depend on the way the chalcogen atoms are arranged[31,32].

Both phases are stable and can appear depending on the chalcogen-transition metal combination, but they may define really different material properties. For instance, monolayer molybdenum disulphide (MoS_2), in the 2H-tetrahedral phase, is a n-type semiconductor with a direct tuneable bandgap, while its corresponding 1T-octahedral phase leads to a metallic behavior.
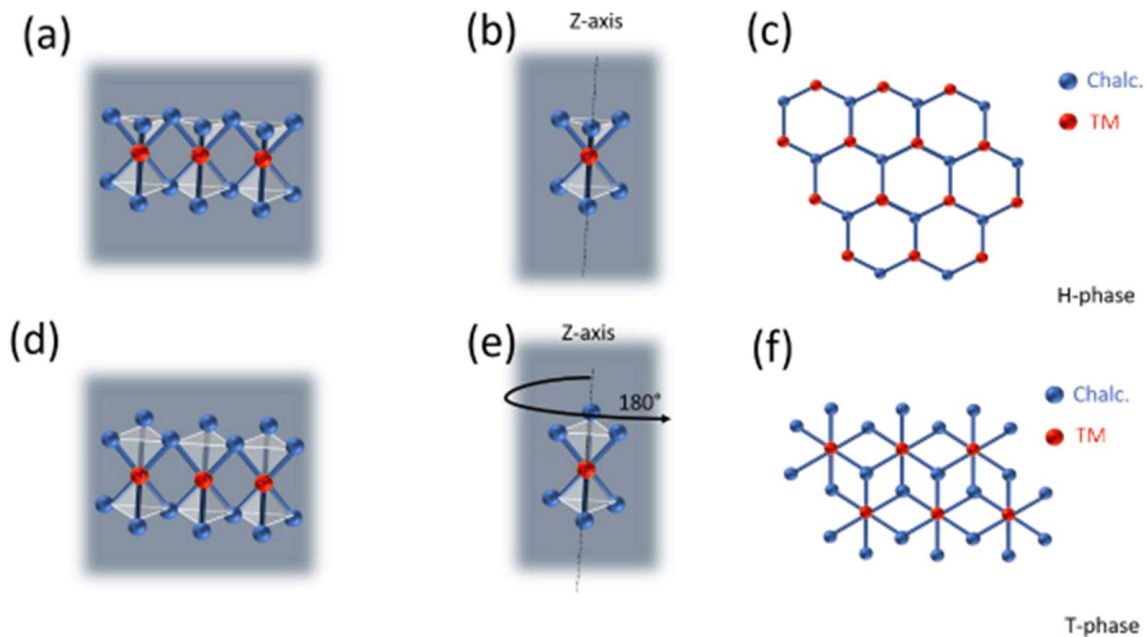
Figure 1.7 – **(a-d)** *TMD crystalline structure,* **(b-e)** *primary phases and* **(c-f)** *hexagonal in plane array of single* MX_2 *layer for the 2H-phase and 1T-phase respectively.*

1.4. Applications

1.4.1. Field Effect Transistors

A transistor is a multifunction device, largely used in integrated circuits, which with other circuit elements acts as current, voltage and signal-power gain. It is referred as an active device, and its main action is the two terminals current control and an ON-OFF switch controlled by applying a voltage potential on a third electrode.

The first transistor was realized in 1925 and then patented in 1934. The dimension was about 130-50 μm with channel of high pure n-type germanium.

During the years many materials have been used for both channel transistor and encapsulation but, in the last couple of decades, the silicon technology has been the leader in this field.

Different types of transistors can be realized, like junction field effect transistors (JFETs), metal-semiconductor FET (MESFET) and metal-oxide-semiconductor field effect transistors (MOSFETs). In this paragraph, the focus is on the MOSFET technology.

A field effect transistor is a three terminals device, where the current flows in a semiconductor region, called the channel, between two terminals, the drain and the source. The channel current flow is modulated by the gate electrode, under the application of an electric field (gate voltage potential, V_{gs}) orthogonal to the channel direction. In a MOSFET, to prevent current losses through the gate (gate leakage), an insulator layer is placed between the conductive channel and the gate electrode.

The main part of the MOSFET is the metal-oxide-semiconductor (MOS) structure. As displayed in **Figure 1.8**, usually a high-conductive silicon polycrystal is heavily opposite doped under the source/drain contacts.
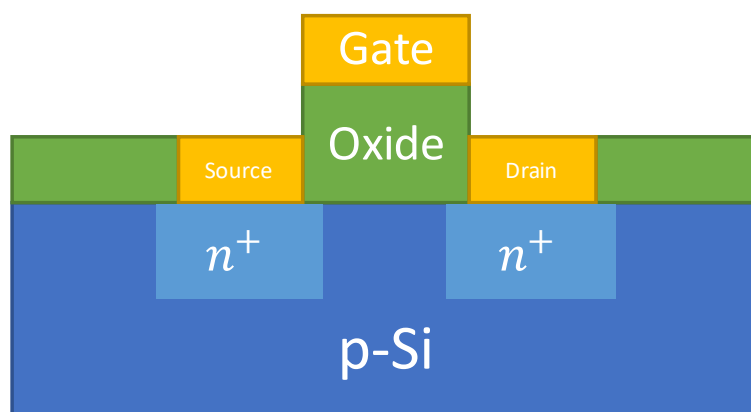
Figure 1.8 – Simple layout of a n-type MOSFET structure.

The MOS channel is covered by an insulator layer (silicon dioxide, SiO_2, for instance), contacted by the gate electrode. **Figure 1.8** reports an example of a n-type MOSFET, with a p-type silicon slice,

heavily n-type doped under the contact, covered by an oxide layer. It also shows that the channel conductance can be modulated through an applied gate voltage.

Consider a p-type semiconductor substrate, as the one reported in **Figure 1.8**. When a negative voltage is applied on the gate, the Si-substrate behaves as a capacitance. Therefore, the free holes are attracted by the gate and accumulate at the semiconductor-insulator interface **Figure 1.9(a)**. No current can flow between the two isolated n-regions, so the transistor is OFF.
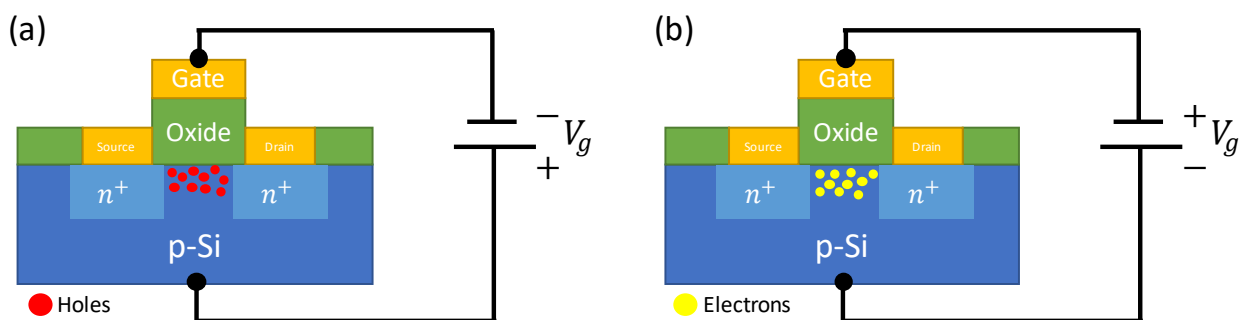
Figure 1.9 – *N-mos capacitor with applied* *(a)* *negative and* *(b)* *positive gate bias.*

When a positive gate voltage is applied, instead, it sweeps away the major charge carriers of the p-type silicon substrate, leaving a net negative charge at the oxide interface (**Figure 1.9(b)**).

At some point, $V_{gs} = V_T$ (threshold voltage), the region under the gate has attracted so many electrons that their accumulation in the silicon channel defines a link between the source and drain electrodes, doped of the same kind. Therefore, the application of a bias voltage (V_{ds}) gives rise to a current flow. This situation is called threshold inversion point and V_T is the minimum voltage to be applied to turn the transistor ON.

Current-Voltage characteristics

When $V_{gs} > V_T$ the charges accumulate at the interface, leading to the formation of an inversion layer between source and drain and the transistor channel, for small drain-source voltages, behaves like a resistance

$$I_{ds} = g_d V_{ds} \qquad\qquad (1.6)$$

where the channel current and the bias voltage are related by the channel conductance g_d, defined as:

$$g_d = \frac{W}{L} \mu_n C_{ox} \qquad\qquad (1.7)$$

where μ_n is the electron mobility (if the MOSFET is p-type, the hole mobility μ_p should be considered), W and L are the channel width and length, and C_{ox} is the oxide/insulator gate capacitance.

Assuming that these parameters are constant, for small voltage bias values the current-voltage ($I-V$) characteristic is linear and dependent on the applied gate voltage, which modulates the current flow between drain and source. An example of some I-V curves by varying V_{gs} is reported in **Figure 1.10(a)**. As mentioned before, for $V_{gs} < V_T$ the drain-source current is zero, as the transistor is set OFF and no channel is formed yet.

The thickness of the channel region depends on V_{gs}. Applying a V_{gs}, the channel region starts to become thinner near the drain electrode. Increasing V_{ds}, V_{gs} becomes lower than V_T and the conductive channel thickness goes to zero (see **Figure 1.10(b)**).
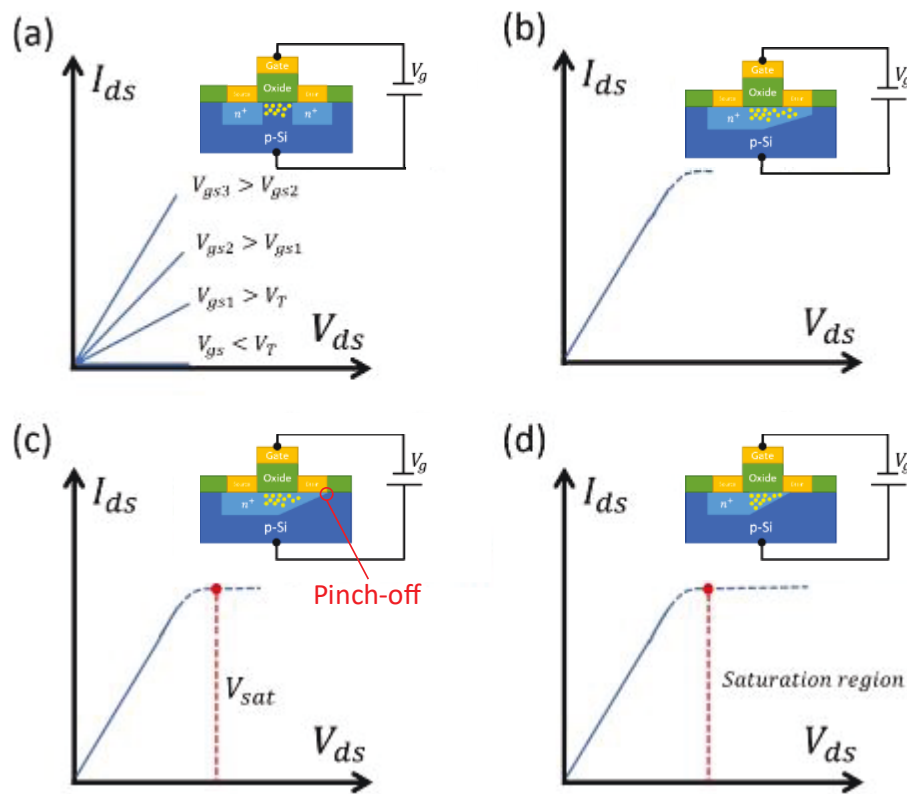
Figure 1.10 – (a) *Current voltage characteristics for small V_{ds} bias (for different gate voltages).* **(b)** *Current voltage characteristic at higher bias value for $V_{ds} < V_{sat}$,* **(c)** *for $V_{ds} = V_{sat}$ and* **(d)** *for $V_{ds} > V_{sat}$. The insets report a scheme of the n-type mosfet device channel modification varying V_{ds}.*

Keeping increase V_{ds}, the current keeps increasing with a slope different from the previous linear region. When V_{ds} reaches the saturation voltage $V_{sat} = V_{gs} - V_T$, the so-called pinch-off of the channel appears (see **Figure 1.10(c)**). For $V_{ds} > V_{sat}$, current reaches then a plateau, letting the device enter the saturation region (see **Figure 1.10(d)**). It is important to highlight that this is an ideal situation, not taking into account non-ideal effects for which the current can have a slightly increase. This behavior is described by:

$$I_{sat} = \frac{I_0\left(V_{gs} - V_T\right)^2}{2} \tag{1.8}$$

Equation(1.8) highlights that the saturation voltage is a function of the gate potential, so that it is possible to create a set of curves varying V_{gs}, for which the current is constant. The total I-V output characteristic is reported in **Figure 1.11(a)**.
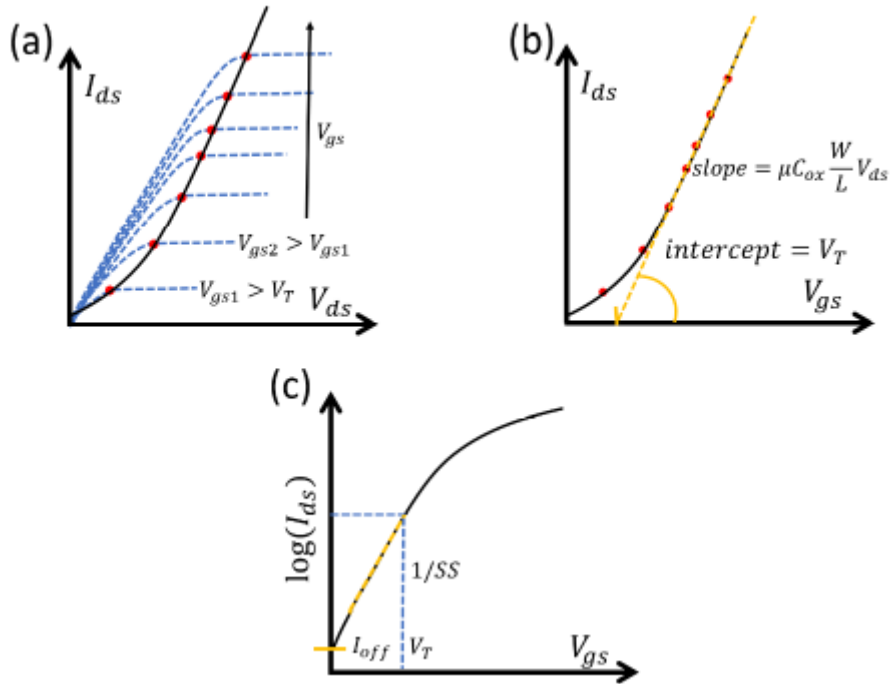
Figure 1.11 – (a) Output characteristic at different gate voltages. (b) Transfer characteristic on linear and (c) semi-logarithmic scale.

For $V_{gs} > V_T$ and $V_{ds} < V_{sat}$, the transistor is in its active mode, where the charge carriers inside the channel can be modulated by the gate voltage. The channel current is thus described by the following equation

$$I_{ds} = \frac{W}{L} \mu C_{ox} \left[(V_{gs} - V_T)V_{ds} - \frac{V_{ds}^2}{2} \right] \qquad (1.9)$$

which, for fixed V_{ds} bias, describes the transfer characteristic of a transistor.

For small V_{ds}, **Equation(1.9)** becomes

$$I_{ds} = \frac{W}{L}\mu C_{ox}\left(V_{gs} - V_T\right)V_{ds} \qquad\qquad (\ 1.10\ )$$

Equation(1.10) is plotted in **Figure 1.11(b)**. **Equation(1.10)** can be used to determine the carrier

mobility and the threshold voltage. Indeed, the linear plot reported in **Figure 1.11(b)** simulates

Equation(1.10), from which mobility and threshold voltage can be extracted. In fact, from the

slope:

$$\mu = slope\,\frac{L}{W C_{ox} V_{ds}} \qquad\qquad (\ 1.11\ )$$

while the x-axis intercept provides the threshold voltage (V_T). Deviation from the straight line at

low and high V_{gs} values are related to the subthreshold conduction and the mobility dependence

on V_{gs}, respectively.

When the MOSFET is in the OFF state a small-negligible but non-zero current flows between the

source and the drain. The OFF current is determined by the circuit design. Of course, lower is the

OFF-state current, less power dissipation occurs when the device is in standby. **Figure 1.11(c)**

shows the transfer characteristic in semi-logarithmic scale, highlighting that the MOSFET OFF-state

current has an exponential behaviour (linear in semi-logarithmic scale). This current is called

subthreshold current (I_{sub}), and it is defined as:

$$I_{sub} = \frac{W}{L}\,exp\left[\frac{q\left(V_g - V_T\right)}{\eta kT}\right] \qquad\qquad (\ 1.12\ )$$

As said before, the ideal situation is to keep the OFF current at the lowest value possible. Looking

at the **Equation(1.12)**, the subthreshold current can be reduced adjusting the channel dimension,

increasing the threshold voltage, decreasing the η factor and/or letting the device work at lower

temperature. At given channel length and width, the only possible way to achieve a lower OFF

current, without negatively affect the device performance, is to reduce the η factor. Indeed, a high

threshold voltage also reduces the ON-state current and degrades the device operation while low cryogenic working temperature requires considerable costs.

To reduce the η factor, one possible thing is to vary the gate oxide thickness. This can be seen from capacitance considerations:

$$\eta = 1 + \frac{C_{dep}}{C_{ox}} \tag{1.13}$$

A reduction of the oxide capacitance, related to the oxide thickness, permits to reduce the η factor and so the OFF-current.

The η factor is otherwise connected to another important transistor parameters, called subthreshold swing (SS):

$$SS = \eta \; 60 \; mV \frac{T}{300K} \tag{1.14}$$

which indicates how rapidly in the subthreshold regime the transistor current is switched off.

The ideal SS value, at room temperature ($300K$), is $60 \; mV/decade$, i.e. with $\eta = 1$.

1.4.2. Schottky Diodes

The intimate contact between a metal and a semiconductor can result in two ideal devices: the ohmic junction or the rectifying (also called Schottky) junction.

In an ideal ohmic junction, the current I varies linearly with the applied voltage V, following the Ohm's rule, and the ratio V/I is the combination of the contact (R_c) and the series (R_s) resistances:

$$V \, I = R_c + R_s \tag{1.15}$$

A good quality ohmic contact has very low contact resistance. Achieving ohmic junctions with low

R_c is a critical point to gain good performance in high-speed semiconductor devices.

In contrast, ideal Schottky junctions act as a perfect diode with high current and very low contact

resistance in one direction (the so-called forward direction, which correspond to the "on" state of

the diode) and negligible current or infinite resistance in the opposite direction (reverse direction

or "off" state).

Figure 1.12 introduces the Schottky model for the metal/semiconductor junction and some

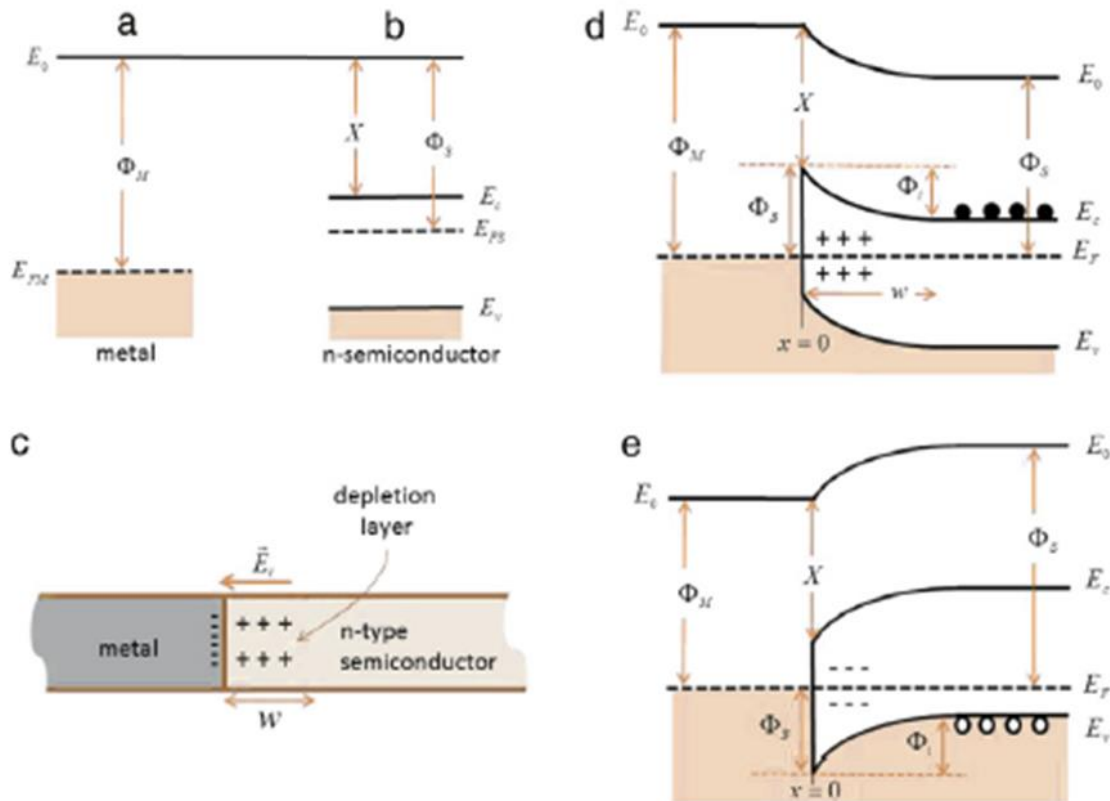relevant quantities.

Figure 1.12 –Energy diagrams of (a) a metal, (b) a n-type semiconductor, (d) a n-type Schottky diode, (e) a p-type Schottky diode. (c) Formation of depletion layer at the interface metal-semiconductor.

Here, a n-type substrate is considered as example. For p-type semiconductors everything works in

a similar manner, with electrons replaced by holes and reversed energy axis.

In **Figure 1.12**, the vacuum level or the free-electron energy, E_0, is the energy state of electrons with zero kinetic energy outside the material, either metal or semiconductor. The difference between E_0 and the Fermi level E_F in any material defines the workfunction ϕ:

$$\phi = E_0 - E_F \qquad (1.16)$$

The Fermi energy E_F represents the highest occupied electron energy state at $T = 0\,K$ in a metal; in a similar way, in a non-degenerate semiconductor, it lies in the gap between the valence and the conduction band, as reported in **Figure 1.12(b)**, i.e. it separates the occupied from the unoccupied states at $T = 0\,K$.

The probability that an electron occupies a state with energy E at the absolute temperature T is described by the Fermi–Dirac distribution function:

$$f(E) = \frac{1}{1 + e^{\frac{(E-EF)}{kT}}} \qquad (1.17)$$

where $k = 8.62 \times 10^{-5}\,eV/K$ is the Boltzmann constant. For $T > 0K$ electrons can occupy levels above the Fermi level with a rapidly decreasing probability as the energy moves away from E_F.

For metals, the workfunction $\Phi_M = E_0 - E_{FM}$ (see **Equation(1.16)**) represents the energy required to remove an electron from the Fermi level E_{FM} to the vacuum. Its value depends only on the type of metal and their workfunctions, which are usually comprised between $\sim$2 and 6 eV.

In each semiconductor, instead, the position of E_{FS} (semiconductor Fermi level) depends also on the doping: E_{FS} is closer to E_c (the lowest allowed energy level of the conduction band) for a n-type semiconductor or closer to E_V (the highest allowed energy level of the valence band for p-type doping. **Figure 1.12(d-e)** show, respectively, the band diagram of a Schottky diode with a n-type and a p-type semiconductor.

The electron and hole densities in a semiconductor (denoted by n and p respectively) are in fact related to the Fermi energy by the following relations:

$$n = N_c e^{-\frac{E_c - E_{FS}}{kT}} \qquad (1.18)$$

$$p = N_V e^{-\frac{E_{FS} - E_V}{kT}} \qquad (1.19)$$

where $N_c = 2\left(2\pi m_e^* \frac{kT}{h^2}\right)^{\frac{3}{2}}$ and $N_V = 2\left(2\pi m_p^* \frac{kT}{h^2}\right)^{\frac{3}{2}}$ are the effective densities of states in the conduction and valence band, and m_e^* and m_p^* are the effective masses of electrons and holes, respectively (with $h = 4.136 \times 10^{-15} \, eV \cdot s$ the Planck constant).

This means that the workfunction in a semiconductor varies according to the doping, as the Fermi level is not fixed. To characterize a semiconductor, therefore, the electron affinity χ is introduced, defined as:

$$\chi = E_0 - E_c \qquad (1.20)$$

This is a constant quantity and express the difference between the vacuum level and the conduction band edge. Here some notable examples of electron affinity are reported: 4.05 eV for Si, 4.07 eV for gallium arsenide (GaAs), 4.0 eV for germanium (Ge).

Schottky Barrier

When a metal-semiconductor contact is established, Fermi levels align at equilibrium. Charge transfer occurs. For a n-type semiconductor and $\phi_M > \phi_S$, electrons flow into the metal, due to the disparity in average energy, higher in the semiconductor rather than in the metal. The transfer of charge results in the formation of a layer at the semiconductor interface depleted of free charge carriers, called depletion layer. The removal of electrons (and similarly of holes for p-type substrates) leaves behind the space immobile charge of the uncompensated dopant ions; for this

28

reason, the depletion layer is also called the space charge region (**Figure 1.12(c)**). The formation of such layer confirms that a Schottky junction has been formed.

If $\phi_M < \phi_S$, instead, electrons inject from the metal to the semiconductor. No depletion layer forms in this case, since the metal can be considered an infinite electron reservoir, and the junction is ohmic (unless some pinning of the Fermi level takes place, see paragraph below).

In a Schottky junction, the space charge formed in the depletion layer is also mirrored by a very thin layer of opposite-sign charge at the metal surface (**Figure 1.12(c)**). This situation, quite similar to a parallel plate capacitor, gives rise to an electric field E_i and a potential ϕ_i at the junction, which prevent further net charge diffusion between the semiconductor and the metal. ϕ_i is called built-in potential and its corresponding energy $\Phi_i = e\phi_i$ is the energy barrier seen by electrons from the semiconductor to the metal. It is defined as:

$$\Phi_i = \Phi_M - \Phi_S \qquad\qquad (1.21)$$

The corresponding electric field formed at the junction is called built-in electric field and opposes to the motion of electrons from the semiconductor to the metal. It has the maximum value at the physical metal-semiconductor interface ($x = 0$ in **Figure 1.12(d)**) and decreases with distance until it vanishes at the edge of the depletion layer ($x = W$). The formation of an energy barrier at the metal/semiconductor interface, Φ_B, as the result of a discontinuity of the allowed energy states in the energy diagram, is known as Schottky barrier. It plays a similar role as Φ_i, with a simple, very important, difference. Φ_i can be modulated by the application of an external voltage bias. On the other hand, Φ_B is not directly affect by the voltage bias (apart for second order effects). The Schottky barrier height is related to the semiconductor electron affinity:

$$\Phi_B = |\Phi_M - \chi| \qquad\qquad (1.22)$$

Equation(1.22) is known as the Schottky–Mott relation. As Φ_M and χ are both intrinsic properties of the crystal lattice, so it is the Schottky barrier height: it cannot be modified by doping or applying voltage bias.

For a p-type substrate, with $\Phi_M > \Phi_S$, a similar barrier forms for the flow of holes from the metal to the semiconductor, and the Schottky/Mott relation becomes:

$$\Phi_B = E_g - |\Phi_M - \chi|$$
(1.23)

where

$$E_g = E_C - E_V$$
(1.24)

is the bandgap of the semiconductor.

Experimental measurements show that the Schottky-Mott relations are only qualitatively valid, with SBH often nearly independent of metal workfunction[33–36]. Indeed, the simple Schottky model neglects certain effects which arise at a junction between two dissimilar materials.

Surface non-ideal effects

The semiconductor surface contains surface (or interface) states, with energies within the semiconductor bandgap, due to incomplete covalent bonds (called Shockley–Tamm states) and other effects (as foreign atoms bonded at the surface and crystal defects). This favours the piling up of charges at the metal-semiconductor interface. J. Bardeen pointed out the importance of surface states in determining the SBH[37].

Usually, there is a thin interfacial layer which is neither semiconductor nor metal, so that the contact is very rarely an atomically sharp discontinuity between the two materials. Silicon crystals for example are usually covered by a thin (10–20 Å) oxide layer even after etching or cleavage in atmospheric conditions. Although electrons can tunnel through it, this thin layer can affect the

30

properties of the junction. Considering a n-type semiconductor, the occupation of some of the surface states by electrons induces a positive depletion layer in the silicon near the surface, causing the energy bands to bend upwards near the surface (**Figure 1.13(a)**). When a junction with a metal with $\Phi_M > \Phi_S$ is formed (**Figure 1.13(b)**), the transfer of electrons from the semiconductor to the metal further bends the conduction band away from the Fermi level and removes negative charge trapped in the surface. Indeed, electrons trapped in the acceptor like interface states contribute to the overall charge transfer from the semiconductor to the metal needed to establish the thermal equilibrium. The larger the density of surface states, the more the trapped charge is removed for each incremental increase of the band bending near the contact. However, if the density of surface states is very large, just a negligible movement of the Fermi level at the semiconductor surface is sufficient to establish thermal equilibrium. In this case the Fermi level is said to be pinned by the high density of states.

The pinning of the Fermi level happens any time many electronic states is clustered near the Fermi level. The pinning of the Fermi level and the presence of a thin interfacial layer at the junction also result in a reduced Schottky barrier height. The interfacial layer of atomic dimensions can contain impurities and added interface states and, more important, can sustain a voltage drop. Otherwise stated, there is an electric field in the extra thin gap between the metal and the semiconductor. The electric field in the gap layer in this case is supported by a negative charge on the metal surface that, together with the negative charge of the occupied acceptor surface states, mirrors the positive charge of the depletion layer in the semiconductor. **Figure 1.13(b)** shows that the gap layer and the interface states originate a reduced Schottky barrier height defined as:

$$\Phi_B = |\Phi_M - \chi - 1|$$
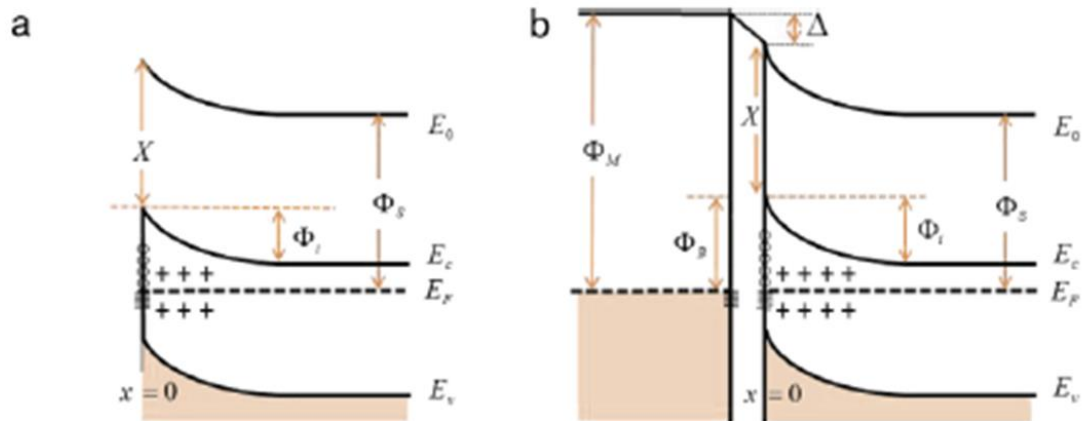
Figure 1.13 – (a) The effect of acceptor like surface states on a n-type semiconductor and (b) on a Schottky junction.

1.4.3. Heterostructures

Two-dimensional (2D) heterostructures have been investigated theoretically and experimentally in the past years. Their innovative properties provide many potential applications. Mainly, 2D heterostructures can be identified into two different types, according to their structures[38–40]:

- Vertical 2D heterostructures, composed of different stacked layers. In vertical 2D heterostructures, the isolated atomic component can be assembled to form new layered materials stacked in a precisely selected sequence. The different layers in vertical heterostructures are generally combined by van der Waals (vdW) interaction. They show some novel electronic[41] and optical properties[42], such as high carrier mobility[43] and good photoresponse performance[44], which can be exploited to design transistors[45,46] and photoelectronic devices[47].

- Lateral 2D heterostructures, where different 2D atomic panels are stitched in a single atomic layer because of the similar structure and small lattice mismatch. Many devices fabricated with lateral heterostructures have demonstrated good performances and shown unique properties. Based on monolayer WSe_2–WS_2 heterojunctions, for example, high-mobility field-effect transistors (FETs), p–n diodes with large rectification behaviour, photovoltaic devices and CMOS inverter with

large current gain have been demonstrated[48]. Also, a photodetector based on MoS$_2$–MoSe$_2$ lateral heterostructures has been reported with responsivity, detectivity, and external quantum efficiency reaching 1.3 A/W, 2.6×10^{11} Jones, and 263.1%, respectively[49]. Moreover, Ming-Yang Li et al have fabricated a light-emitting device designed with lateral WSe$_2$–MoS$_2$ heterostructure which exhibits a conversion efficiency of 1 m% (the ratio of the emitted photon to the injected carriers) in 70 kW cm^{-2}, higher than a homojunction device based on simple monolayer MoS$_2$[50]. These devices built with LHSs can potentially be used in future electronic circuits and device applications.

1.4.4. Field Emission

The electrons emission from a conductive (metallic or semiconductor) surface under the application of an electrostatic field is called field emission. It is also called cold cathodes emission, to differentiate it from the thermionic emission, where electrons are extracted by raising the sample temperature. For long time this effect has not been fully understood and only in the late 1920s Fowler and Nordheim gives to it an explanation. They demonstrated that field emission could be described considering electron tunneling through a triangular potential barrier. Indeed, the applied electrostatic field gives to the electron sufficient energy to overcome the surface-vacuum barrier.

Fowler and Nordheim proposed a simple equation to describe the current-voltage relationship which regulates the field emission for semiconductors:

$$I = \frac{AaE_s^2}{\varphi} \, e^{\frac{-b\varphi^{\frac{3}{2}}}{E_s}} \tag{1.25}$$

where A is the emitting area, E_s is the local electric field, ɸ is the workfunction of the semiconducting material and $a = 1.54 \cdot 10^{-6} \; A \; eV \; V^{-2}$ and $b = 6.83 \cdot 10^{9} \; V \; m^{-1} \; eV^{-\frac{3}{2}}$ are constants. Although **Equation(1.25)** refers to flat surfaces, it has been successfully used to

describe the field emission current of different nanostructured materials, just considering some minor adjustments to consider their 2D or 1D nature.

In the first place, the field emission was considered an undesirable effect, as it could cause vacuum breakdown and discharge phenomena. Nowadays, instead, several applications are based on this phenomenon, from the field of microscopy and spectroscopy to the use of field electron emitters as electron-gun sources or as active components for vacuum electronics. Anyway, a great boost to the research in such field was given by the discovery of 2D and 1D materials. In fact, their large aspect ratio allows to intensify the fields at their edges, favouring the electrons emission from the surface. Nowadays, a great research effort is still needed to optimize the performance of field emitting devices and their figures of merit such as the turn on field (the minimum electric field from which it is possible to extract electrons), and the max current density (the maximum field emission current that can be recorded without damaging the material).

2. 2D Materials Based Field Effect Transistors

In this chapter the results of several experimental studies concerning the electrical properties of different 2D materials, used as FETs' channels, are reported. The aim of these works was to investigate the intrinsic transport properties of these materials under different conditions, such as temperature and pressure variations and light or electron irradiation. Even if referring to a specific 2D material, most of the results are also valid when applied to other layered materials that present similar characteristics.

Despite MoS_2 has been widely investigated by the scientific community, there are still some interesting unexplored features. Here, in the first part of this chapter, two different MoS_2 properties are investigated. In the first paragraph, it is reported how an electron beam can affect a MoS_2-based FET. It is shown that the exposure of Ti/Au source/drain electrodes to an electron beam reduces the contact resistance and improves the transistor performance. The electron beam conditioning of contacts is permanent, while the irradiation of the channel can produce transient effects. It is demonstrated that irradiation lowers the Schottky barrier at the contacts because of thermally induced atom diffusion and interfacial reactions. The simulation of electron paths in the device reveals that most of the beam energy is absorbed in the metal contacts. The study demonstrates that electron beam irradiation can be effectively used for contact improvement through local annealing. The results derive from a study conducted in collaboration with the University of Duisburg-Essen and Università degli Studi dell'Aquila, and they have been published with the title "Electron Irradiation of Metal Contacts in Monolayer MoS_2 Field-Effect Transistors" by Pelella et al in ACS Applied Materials and Interfaces (2020)[1].

In the second paragraph, MoS_2 nanosheets, obtained via chemical vapor deposition onto SiO_2/Si substrates, are exploited to fabricate field-effect transistors with n-type conduction, high on/off

ratio, steep subthreshold slope, and good mobility. Local field emission measurements from the edges of the MoS₂ nanosheets are performed in high vacuum using a tip-shaped anode. It is demonstrated that the voltage applied to the Si substrate back-gate modulates the field emission current. Such a finding, that it is attributed to gate-bias lowering of the MoS₂ electron affinity, enables a new field-effect transistor based on field emission. This study also derives from the same collaboration and resulted in another work entitled "Gate-Controlled Field Emission Current from MoS₂ Nanosheets" by Pelella et al, published in Advanced Electronic Materials in 2020[2].

Finally, in the third paragraph, the electrical properties of platinum diselenide (PtSe₂), another member of the TMDs family, are investigated. The research focuses on investigating the electrical response of the material when exposed to supercontinuum white laser irradiation. It is demonstrated that the external pressure is responsible for different response to light of the material, leading to positive or negative photoconductivity in vacuum and at a room pressure, respectively. The research on the electrical properties of PtSe₂ was conducted in collaboration with the Tyndall National Institute of Cork and Trinity College of Dublin, which resulted in the publication of the paper "Coexistence of negative and positive photoconductivity in few-layer PtSe₂ field-effect transistors" published in Advanced Functional Materials in 2021[3].

2.1. MoS₂ Field Effect transistor – Effect of Electron Beam Irradiation

Molybdenum disulphide (MoS₂) is one of the most studied transition metal dichalcogenides, owing to its layered structure and useful mechanical, chemical, electronic and optoelectronic properties. Despite the lower field-effect mobility than graphene [51,52], ranging from few tenths to hundreds of $cm^2 V^{-1} s^{-1}$[21,53–55], MoS₂ field effect transistors (FETs) have recently become very popular as alternatives to graphene FETs[21,53–57] for next generation electronics based on 2D-materials[58–65].

The fabrication and characterization of devices based on 2D materials greatly rely on the application of electron beam (e-beam) lithography (EBL) or focussed ion beam processing as well as on scanning (SEM) or transmission electron microscopy (TEM), which imply irradiation by charged particles. From the literature, we know that the exposure to low-energy electrons and/or ions can modify the electronic properties of the 2D materials or their interfaces[57,66,67]. Indeed, structural defects can locally modify the band structure and behave as charge traps, thereby changing the device characteristics. It can happen both in the case of e-beam[68,69] and ion beam irradiation[70,71]. On the other hand, e-beam, ion irradiation and plasma treatments can be intentionally used for nano-incisions[72], pores[73], or to purposely create defects, for instance to reduce the contact resistance[74–76]. Choi et al. reported the effects of 30 keV e-beam irradiation of monolayer MoS_2 FETs, showing that irradiation-induced defects act as trap sites reducing the carrier mobility and concentration and shifting the threshold voltage[77]. A study of point defects in MoS_2 using SEM imaging and first-principles calculations, by Zhou et al., demonstrated that vacancies are created by e-beam irradiation at low energies[78], below 30 keV. Durand et al. studied the effects of e-beam on MoS_2-based FET reporting an increase of the carriers density and a decrease of the mobility explained as irradiation-induced generation of intrinsic defects in MoS_2 and as Coulomb scattering by charges at the MoS_2/SiO_2 interface, respectively[79].

In this paragraph, the electrical characterization of monolayer MoS_2-based FETs, with Schottky Ti/Au contacts, is presented, focusing on the effects of low-energy e-beam irradiation. The long exposure of the metal contacts to 10 keV e-beam in a SEM chamber enhances the transistor´s on-current. Such an improvement can be explained by radiation-induced lowering of the Schottky barrier at the metal contacts. Monte Carlo simulation has been also performed to track the e-beam through the device, showing that, when the beam is focussed onto the contacts, most of the beam energy is absorbed within the metal. The local heat can induce atomic diffusion and

interfacial reactions that change the chemical composition and structure of the metal/MoS$_2$ interface or can generate or release tensile strain. Both effects cause the lowering of the Schottky barrier and the consequent increase of the transistor current.

This study shows that e-beam exposure during SEM imaging has non-negligible effects on MoS$_2$ devices; however, it also highlights that a suitable exposure, with the e-beam focused on the contact region, can be conveniently performed to reduce the contact resistance of the transistor. Compared to thermal annealing, it provides a way to improve the contact resistance by local conditioning, which avoids the exposure of the entire wafer to a high thermal budget.

2.1.1. Fabrication And Experimental Methods

The MoS$_2$ monolayer flakes were grown via chemical vapour deposition (CVD) in a three-zone split tube furnace, purged with 1000 Ncm^3/min of Ar gas for 15 min to minimize the O$_2$ content. The growth SiO$_2$/Si substrate was spin coated with a 1% sodium cholate solution. Then, a saturated ammonium heptamolybdate (AHM) solution was first annealed at 300 °C under ambient conditions, to turn AHM into MoO$_3$, which was used as the source for molybdenum. The target material was placed in a three-zone tube furnace along with 50 mg of S powder, positioned upstream in a separate heating zone. The zones containing the S and AHM were heated to 150 °C and 750 °C, respectively. After 15 min of growth, the process was stopped, and the sample was cooled rapidly.

Field-effect transistors have been realized using the SiO$_2$/Si substrate (SiO$_2$ thickness: 285 nm) as the back-gate. On top, drain and source electrodes have been evaporated and patterned (through standard photolithography and lift-off processes) on the selected MoS$_2$ flakes. The contacts were made of Ti (10 nm) and Au (40 nm), used as adhesion and cover layers, respectively. Titanium was

deposited in high vacuum, which could not exclude the formation of TiO_2 contributing to the resistance and Schottky barrier at the contacts.

Figure 2.1(a-b) show the SEM top view of the device and its schematic layout and measurement setup. Raman spectrum and photoluminescence (PL, see **Figure 2.2** below) tell us that the channel is made up from a 20x4 µm monolayer flake. Atomic force microscope (AFM) images displayed in **Figure 2.1(c-d)** show that the flake has an average height of 1.0 – 1.3 nm, confirming the single layer, and it appears to be extremely flat (with a roughness rms < 0.25 nm) and structurally intact. Contacted and non-contacted flake areas do not differ with respect to contamination density – spectroscopic data should thus be comparable.

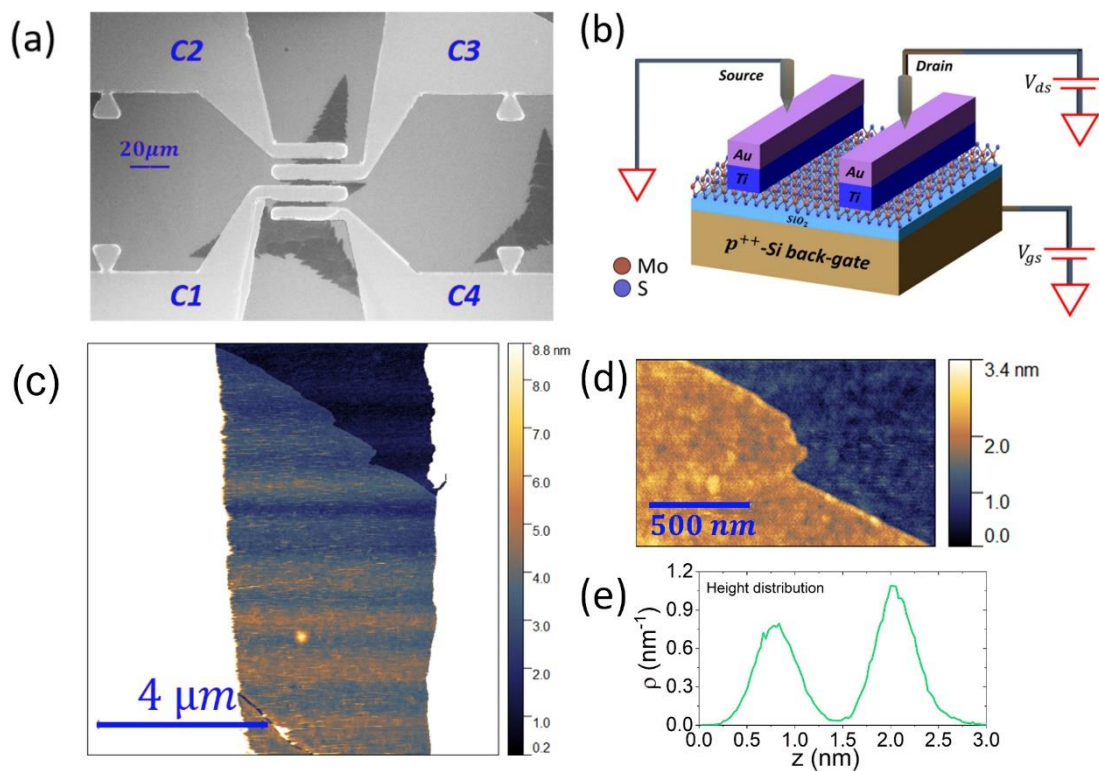*Figure 2.1- (a) SEM image and contact labels of the MoS₂ device. (b) MoS₂ FET layout and schematic of the common source configuration used for the electrical characterization. (c) AFM image of the MoS₂ flake between the electrical contacts (white) (d) A zoom-in into the upper region of (c) showing that the flake is flat and structurally intact. (e) Height distribution taken from image (d) yielding a height of ∼1.2 nm.*

A total of seven MoS$_2$ channels of identically prepared FETs have been characterized by Raman and PL spectroscopy just after processing. The measurements were performed with a Renishaw InVia Raman microscope at ICAN (Interdisciplinary Center for Analytics on the Nanoscale). The excitation laser wavelength was 532 nm and the power density was kept below 0.1 mW/µm² to avoid damage to the MoS$_2$ flake. **Figure 2.2** shows exemplary spectra of the Raman characterization. The shape of the PL spectra (**Figure 2.2(a)**) and the difference of the Raman modes (**Figure 2.2(b)**) differ significantly. The PL intensity (sum of all excitons and trions) for non-contacted MoS$_2$ flakes is higher by a factor of 1.7 ± 0.8 than for contacted MoS$_2$. The mode difference for non-contacted and contacted MoS$_2$ is 21.3 ± 0.7 cm^{-1} and 19.7 ± 0.7 cm^{-1}, respectively. Both the changes in PL and Raman mode difference can be attributed to built-in strains or changes in the electronic properties and band structure of the MoS$_2$ sheets[80–84]. From the linear dependencies of Raman mode positions on doping and strain[80,81], we find a reduction of tensile strain by (0.46 ± 0.28) % and an increase in the electron doping of 0.44 ± 0.36 × 1013 electrons per cm² for the contacted 2D material in comparison with non-contacted MoS2 (details of the calculation method can be found in reference[85]). Hence, the significant alterations in the spectroscopic pre-characterization of the MoS$_2$ channels can be clearly attributed to electronic and structural changes at the metal contact.
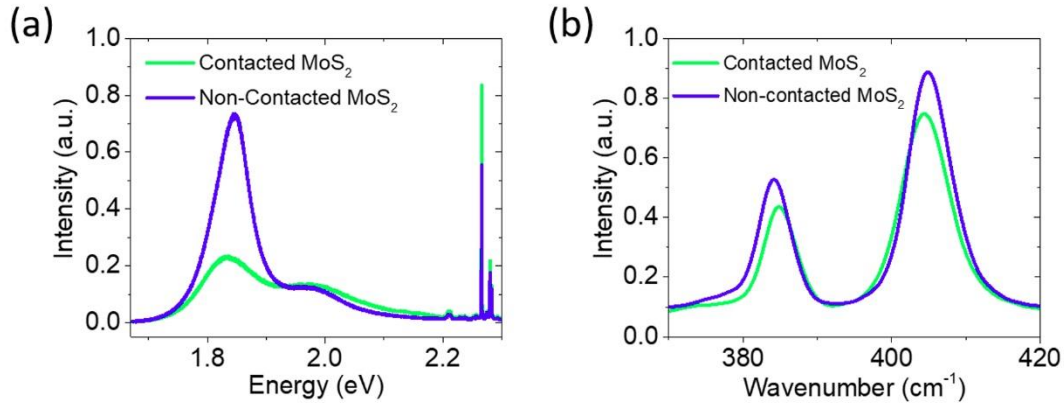
Figure 2.2 – (a) *Photoluminescence and* **(b)** *Raman spectrum of monolayer MoS₂ after FET processing. Green: contacted MoS₂ monolayer flake, blue: non-contacted monolayer MoS₂ flake.*

In the following, most of the electrical characterization refers to the transistor between the contacts labelled as C2 and C3 in **Figure 2.1(a)**. The contact C3 was used as the drain and C2 as the grounded source. The electrical measurements were carried out inside a SEM chamber (LEO 1530, Zeiss), endowed with two metallic probes with nanometer positioning capability, connected to a Keithley 4200 SCS (source measurement units, Tektronix Inc.), at room temperature and pressure of about 10^{-6} mbar. Finally, the e-beam of the SEM, set to 10 keV and 10 pA, was used for the time-controlled irradiation of specific parts of the device.

2.1.2. Standard characterization

The standard characterization of a transistor requires the measurement of the current I_{ds} flowing in the channel as a function of the voltage V_{ds} applied between drain and source (output characteristic) and of the voltage V_{gs} applied between gate and source (transfer characteristic). **Figure 2.3(a-b)** report the output and the transfer characteristics. The output current shows its forward branch at negative voltages, typical of a p-type Schottky diode. Transfer characteristic shows high current for high positive voltages, telling us the current flows is due to electrons and the device is a n-type transistor. Although it seems a contradiction, this behaviour has been previously reported in literature for MoS₂ and WSe₂, and it is explained by the formation of two

back-to-back Schottky diodes at the contacts[86,87]. The asymmetric output characteristic is caused not only by the different contact areas, but also by the different image force barrier lowering of the contact junctions. Indeed, image force barrier lowering of the forced junction (the drain, C3) is higher, as the voltage is directly applied to it. Also, the reverse current at positive voltages is limited by the grounded junction at the source contact (C2).
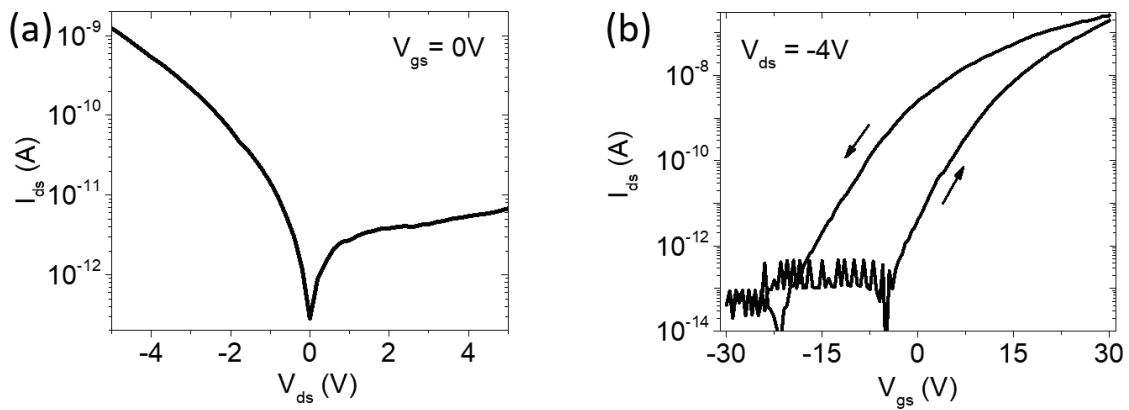
Figure 2.3 - Output **(a)** and transfer **(b)** characteristics of the device between C2 and C3 contacts, with C3 used as the drain and C2 as the grounded source.

2.1.3. Electron beam irradiation on metal contacts

During the characterization of samples or live viewing through SEM, devices are irradiated by electron beam. In this section the effect of electron beam irradiation on metal contacts is under study.

Two set of exposures to the SEM e-beam has been performed, first focusing the beam on the drain contact C3, then on the grounded source C2. Each exposure lasted 300s, with a fluence of $\sim 180 \frac{e^-}{nm^2}$, over a surface of ~ 100 µm^2. A final exposure of the MoS2 channel to the e-beam was performed as well.

Figure 2.4 - ***(a)*** *Output characteristics at* $V_{gs} = 0V$ *performed after each exposure. Electron beam irradiates first contact C3, then contact C2.* ***(b)*** *Rectification ratio and* ***(c)*** *maximum forward and reverse current, at* $V_{ds}=\pm5$ *V, as a function of the irradiation number.* ***(d)*** *Zero-bias Schottky barrier variation at the contact C2 and C3 as a function of the irradiation number.*

Figure 2.4 summarizes the obtained results. The output curves were measured at the end of each irradiation, ~120 s a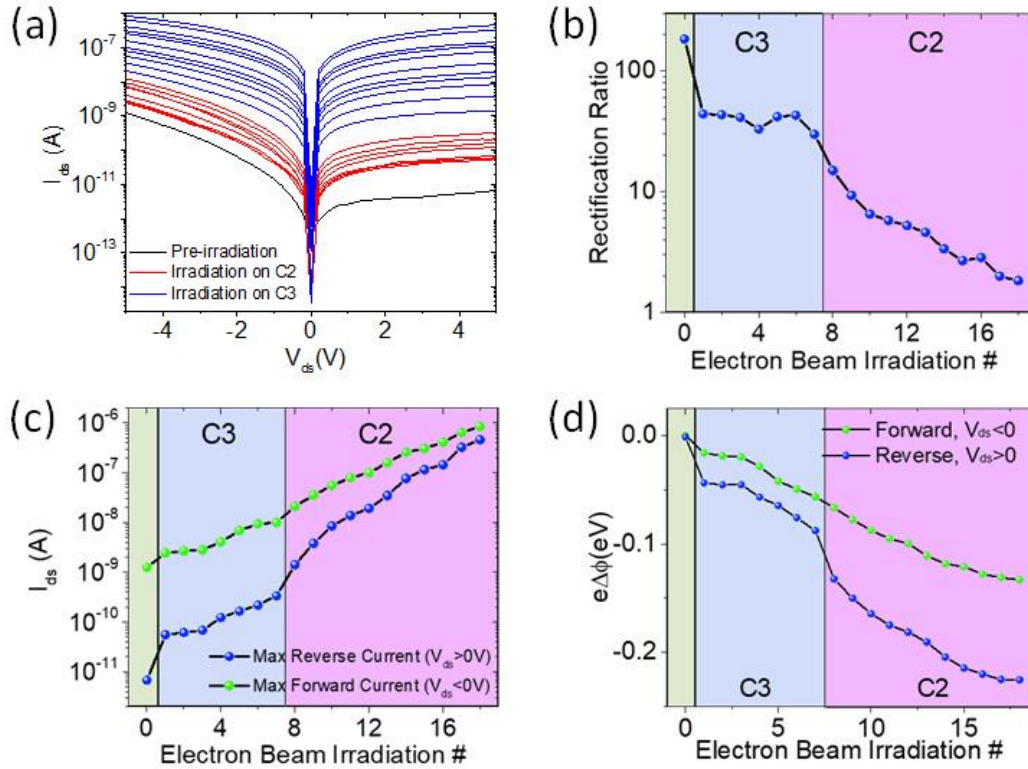fter the blanking of the e-beam, to allow cooling down. Starting from the bottom (black) line in **Figure 2.4(a)** representing the output curve of the unexposed device, the current increases with the e-beam exposures. At the start of each irradiation set, the sequence of the output curves shows a discontinuity. These two gaps have been caused by the uncontrolled exposure of the whole device during the selection of the contacts area (C3 and C2) for the next irradiation set. Moreover, there are two distinct effects of the irradiations on the drain and on the grounded source. Indeed, while, irradiating the drain, current increases both in forward and in the reverse, resulting in a rectification ratio almost constant (see **Figure 2.4(b)**) , the irradiation of the source, instead, make the reverse current increase in a faster way, rendering the output curves more symmetric. This results in a dramatically decrease of the rectification ratio (at $V_{ds}=\pm5$ V)

while the ground source contact is irradiated. Besides, maximum reverse and forward currents at $V_{ds}=\pm5$ V (displayed in **Figure 2.4(c)**) have different variation rates depending on which contact is irradiated. **Figure 2.4(c)** also shows that the increase of both the reverse and forward current is an exponential function of the fluence, which is proportional to and can be parametrized by the irradiation number. These results point to radiation induced Schottky barrier lowering. Indeed, the shape and the current intensity of the output characteristics are related to Schottky barrier heights at contacts, and both the exponentially increasing current and the changing rectification ratio suggest that something is changing. The energy release in the metal contacts can modify the chemistry of the metal/MoS$_2$ interface or create stress and defects that can lead to a lowering of the barrier and a consequent contact resistance reduction.

In the literature, the reduction of the contact resistance by chemical reactions between the metal contacts and the MoS$_2$ has been reported[81,88]. It is also possible that diffusion of Au atoms to the interface with MoS$_2$ occurs under the energetic e-beam irradiation. Au does not react with MoS$_2$ but reduces the contact resistance and therefore the Schottky barrier height[89]. Similarly, tensile strain has been demonstrated to induce considerable Schottky and tunneling barrier lowering[90].

Moreover, a Schottky barrier of ~0.2 eV is formed by several metals on MoS$_2$ because of Fermi level pinning below the MoS$_2$ conduction band[91–93]. Density functional theory calculations have indicated that the pinning at metal-MoS$_2$ interface is different from the well-known Bardeen pinning effect, metal-induced gap states, and defect/disorder induced gap states, which are applicable to traditional metal-semiconductor junctions. At metal-MoS$_2$ interfaces, indeed, the Fermi level is pinned either by a metal work function modification, due to interface dipole formation arising from the charge redistribution, or by the production of gap states (mainly Mo d-orbitals), characterized by the weakened intralayer S-Mo bonding due to the interface metal-S interaction[94,95]. The observed decrease of the Schottky barrier by e-beam irradiation, up to its

complete disappearance, supports the occurrence of interface modifications that cause Fermi level depinning.

Schottky barriers as a function of the fluence (i.e. the e-beam irradiation number) can be extracted from **Figure 2.4(a)**, considering that at negative and positive voltages, current is limited by the Schottky barrier respectively at the drain (C3) and at the source (C2) contact. The device output characteristic encloses two revers-biased junctions. Therefore, let us consider the thermionic current through a reverse biased Schottky barrier:

$$I_n = I_{sn}\left[e^{\frac{eV_a}{nkT}}-1\right] = \left[SA_{2D}^* \; T^{3/2} e^{\frac{e\varphi_{Bn}}{kT}}\right]\left[e^{\frac{eV_a}{nkT}}-1\right] \approx -SA_{2D}^* \; T^{3/2} e^{\frac{e\varphi_{Bn}}{kT}} \qquad (\;2.1\;)$$

where ϕ_{Bn} and I_{sn} are the barrier height and the reverse saturation current at the n-th e-beam irradiation, S is the junction area and A_{2D}^* is the 2D Richardson constant, k is the Boltzmann constant, T is the temperature, n is the ideality factor, and V_a is the negative voltage across the barrier that makes $e^{\frac{eV_a}{nkT}} \approx 0$. Let us define I_0 as the reverse saturation current before e-beam exposure, i.e., associated to the maximum barrier height ϕ_{B0}. Both I_n and I_0 are obtained by extrapolating the measured currents at zero bias to avoid the effect of bias which can induce image-force barrier lowering[96]. Then, **Equation(2.1)** can be used to evaluate the variation of the Schottky barrier, $\Delta\phi_{Bn}=\phi_{Bn}-\phi_{B0}$, as a function of the irradiation number:

$$ln\left(\frac{I_n}{I_o}\right) = -\frac{e\Delta\varphi_{Bn}}{kT} \rightarrow \Delta\varphi_{Bn} = -\frac{kT}{e} ln\left(\frac{I_n}{I_o}\right) \qquad (\;2.2\;)$$

The zero-bias Schottky barrier variation, $\Delta\phi_{Bn}$, is shown in **Figure 2.4(d)** for both source (C2) and drain (C3) contacts. The overall reduction of both barriers is comparable to the expected initial barrier height based on Fermi level pinning. It confirms that a long enough irradiation let the barriers disappear. However, the plot indicates that irradiation on C2 and C3 affect the two

barriers in different ways. Indeed, the barrier decrease is faster when the grounded source is irradiated. Moreover, when the source contact C2 is irradiated, the Schottky barrier at the source contact decrease is more sloping than the Schottky barrier at the C3 contact.

2.1.3.1. Explaining model

To explain these results, we propose the model based on the energy band diagrams shown in **Figure 2.5**. When a voltage is applied to the drain contact C3, an upward ($V_{ds} < 0\,V$) or a downward ($V_{ds} > 0\,V$) shift of the energy bands in the drain region is caused. The red dashed lines in **Figure 2.5** show how e-beam irradiation of the contact lowers the Schottky barrier and the relative built-in potential. The irradiation of one contact also affects the unexposed barrier, which can experience a stronger potential drop due to the reduced contact resistance of the irradiated contact, lowering itself.

Figure 2.5(a) represents the situation in which the e-beam is focussed on the biased drain contact (C3). At $V_{ds} < 0\,V$, the current is limited mainly by the drain contact barrier, which is lowered by the successive irradiations, causing the exponential increase of the maximum forward current. At $V_{ds} > 0\,V$, the current is limited by the unirradiated source contact (C2) barrier, and its dependence on the irradiation cycle is caused by the lowering of the built-in potential at the drain (C3). As the barrier and built-in lowering are almost the same, the rectification ratio remains about constant. When the grounded source C2 is irradiated (**Figure 2.5(b)**), the current increases due to the same mechanism. However, for $V_{ds} > 0\,V$, the drain contact barrier limits the current to a lesser extent, having been already irradiation-lowered. Therefore, the reverse current increases faster with the repeated irradiation and the rectification ratio decreases.
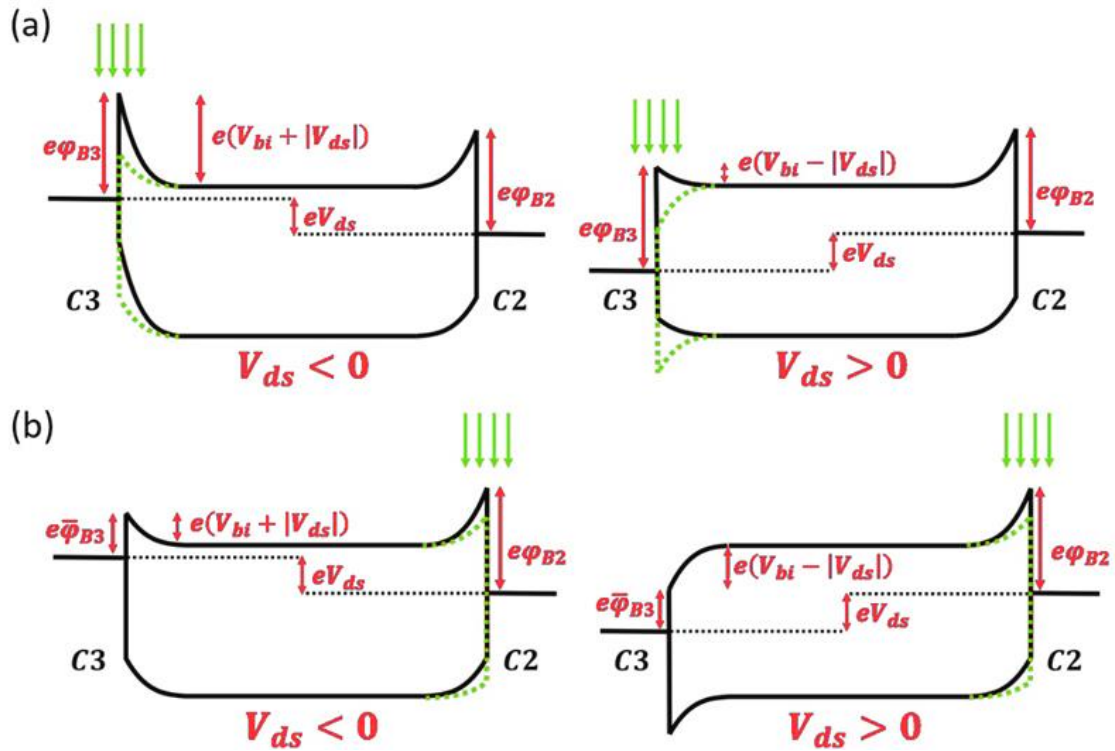
Figure 2.5 - *Low-bias energy band diagrams (black) and their modification under electron irradiation (red) of C3 **(a)** and of C2 **(b)** contact resulting in barrier lowering ($\bar{\varphi}_B$).*

2.1.3.2. The effect of the irradiation on the transfer characteristic

Figure 2.6 shows the effect of the irradiation on the device transfer characteristic. It confirms the radiation-induced increase of the channel current. Moreover, **Figure 2.6(a)** shows that the e-beam, wherever it is focussed on, causes a left shift of the transfer curve. The transfer curves are taken at the end of the two irradiation sets on the drain (C3) and grounded source (C2), and after two successive irradiations on the channel region.

Such a shift corresponds to a decrease of threshold voltage, defined as the x-axis intercept of the linear fit of the transfer curve on linear scale. **Figure 2.6(b)** shows the threshold voltage as a function of the irradiation. The observed negative shift of the threshold voltage has been reported and discussed before[68]. Indeed, positive charges pile up in trap states of the SiO_2 gate dielectric or

at the SiO_2/Si interface. The e-beam irradiation produces electron-hole pairs in the SiO_2 oxide and in the Si substrate. The applied bias can easily sweep the mobile electrons away, while positive charges can be stored for longer times[68]. These positive charges act as an extra gate and enhances the n-type doping of the channel, thus resulting in a left shift of the transfer curve.

Confirming this, a slight recovery of the threshold voltage after 12 h annealing at room temperature is reported in **Figure 2.6**. However, the maximum channel current, which is limited by the contact resistances, remains unchanged after the annealing (**Figure 2.6(a)**), demonstrating that the irradiation-induced improvement of the contacts is permanent.
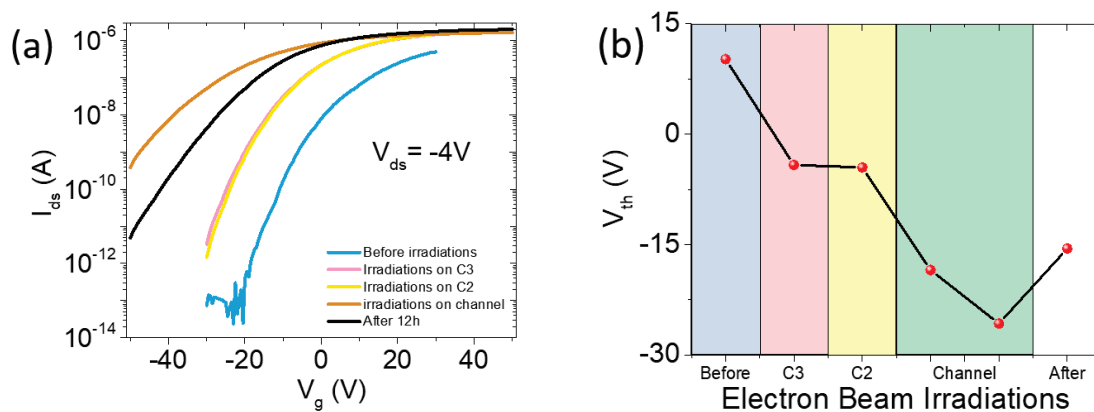
Figure 2.6 - (a) FET transfer characteristics at V_{ds} = -4 V before and after e-beam irradiations of contacts C3 and C2 as well as of channel. (b) Left shift of the threshold voltage extrapolated from the transfer characteristics over the e-beam exposure.

2.1.3.3. Monte Carlo simulation

To further confirm our model, a Monte Carlo simulation has been performed (CASINO software package[97–99] to keep track of the electrons path under the contacts and in the channel region (**Figure 2.7(a-b)**). The software simulates a 10 keV beam with one million electrons and a radius beam of 10 nm. The cathodoluminescence spectrum and the penetration depth of electrons are reported in **Figure 2.7(c)**. It shows that, when the e-beam is focused on the contacts, electrons

lose their energy and are stopped mostly in the Ti/Au metal stack. Instead, when the irradiation is performed directly on the channel, they can reach the Si substrate, where they are absorbed in. The high release of energy in the metal contacts, similarly to thermal annealing[100,101], induces Ti/MoS$_2$ reactions and creates contact with reduced Schottky barrier and contact resistance. Conversely, when we directly irradiate the MoS$_2$ channel, energy is prevalently adsorbed in the Si bulk, and its effect manifest only through the positive charge traps generated in the SiO$_2$ layer.
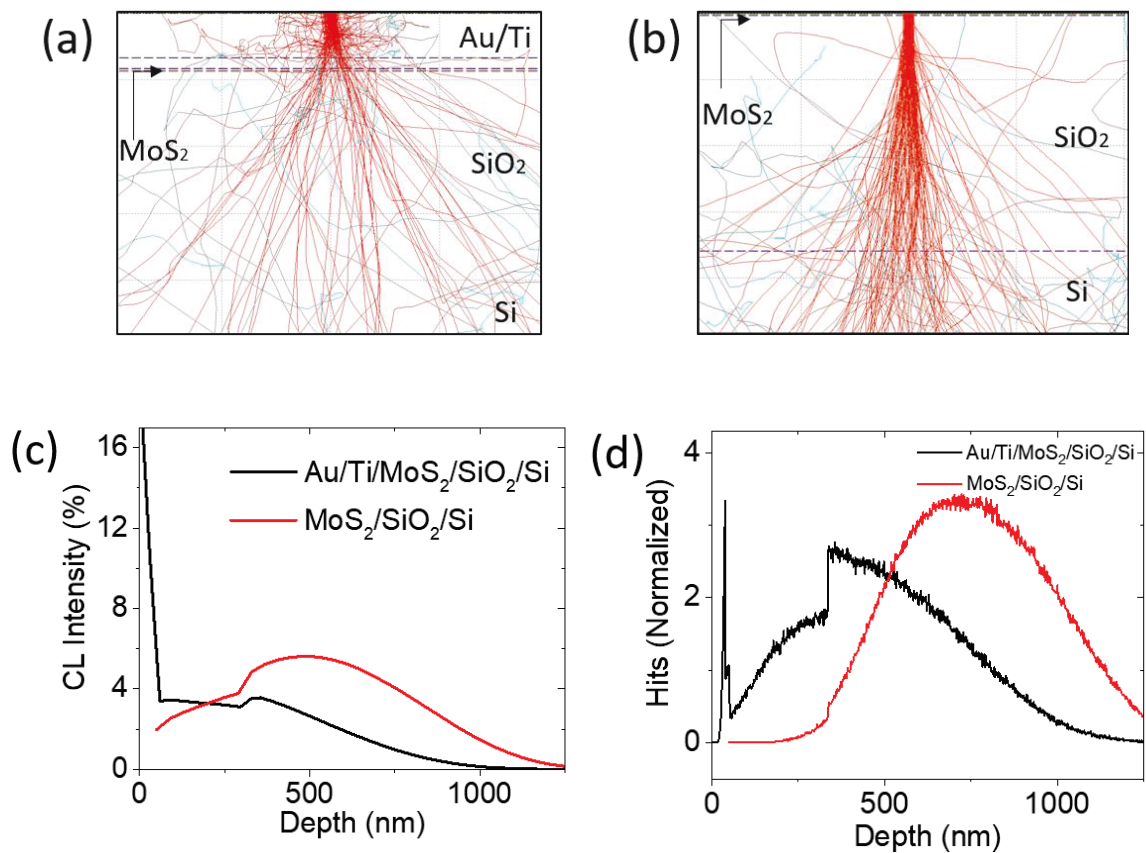

Figure 2.7 - *Monte Carlo simulation using CASINO v2 of e-beam irradiation of the device (a) contacts and (b) of the MoS$_2$ channel. (c) Simulated cathodoluminescence intensity through the sample, with the e-beam focused onto contacts and onto the flake. (d) Simulation of the electron´s penetration depth through the sample.*

2.2. MoS$_2$ Gate controlled field emission

MoS$_2$ have been considered a good candidate for field emission devices. In general, all TMDs possess atomically sharp edges and localized defects that enhance the local electric field and enable the extraction of a field emission current at low turn-on voltage. As discussed in Chapter 1, Field emission (FE) is a quantum mechanical phenomenon in which electrons, extracted from a conductor or a semiconductor surface under application of an intense electric field, move in vacuum from a cathode to an anode. Examples of field emission applications are electrically-operated floating-gate memory cells[102,103], electron microscopy[104] and e-beam lithography[105], display technology[106] and vacuum electronics[107]. FE current from MoS$_2$ flakes with a low turn-on field and a high field enhancement factor has been reported from both the edges and the flat part of few-layer MoS$_2$ flakes[108,68,109,110]. The intrinsic n-doping of MoS$_2$, possibly controlled by a back gate[111], paves the way for future MoS$_2$ FE applications.

As a parallel result, the MoS2 FET has been analysed as a gas sensor. The electrical properties of two-dimensional (2D) materials are sensitive to ambient gases and pressure variation[112]. Indeed, it has been reported that the adsorbed gases on the MoS2 channel of FETs result in degradation of device conductance, in enhanced hysteresis and in threshold voltage shifting[113,112,114]. Conversely, vacuum annealing can increase the MoS$_2$ device conductance by desorbing the gas molecules.

2.2.1. Fabrication, schematic layout and material characterization

Following the fabrication process described in paragraph 2.1.1, MoS$_2$ flakes have been synthesised and then selected to fabricate FET through standard photolithography and lift-off processes. **Figure 2.8(a-b)** show the SEM top view of a typical device and its schematic layout and biasing circuit. The Si substrate is the back-gate while the evaporated Ti/Au (10/40 nm) electrodes are the source and the drain of the FET. The flakes are monolayer according to the PL and Raman characterization performed before metal deposition. The spectra of **Figure 2.8(c-d)** show a PL peak at 1.85 eV and a separation about 20 cm^{-1} between E^1_{2g} and the A_{1g} Raman mode typical of the

monolayer. Raman and electrical measurements have been carried out using the same tools and settings described in paragraph 2.1.1.
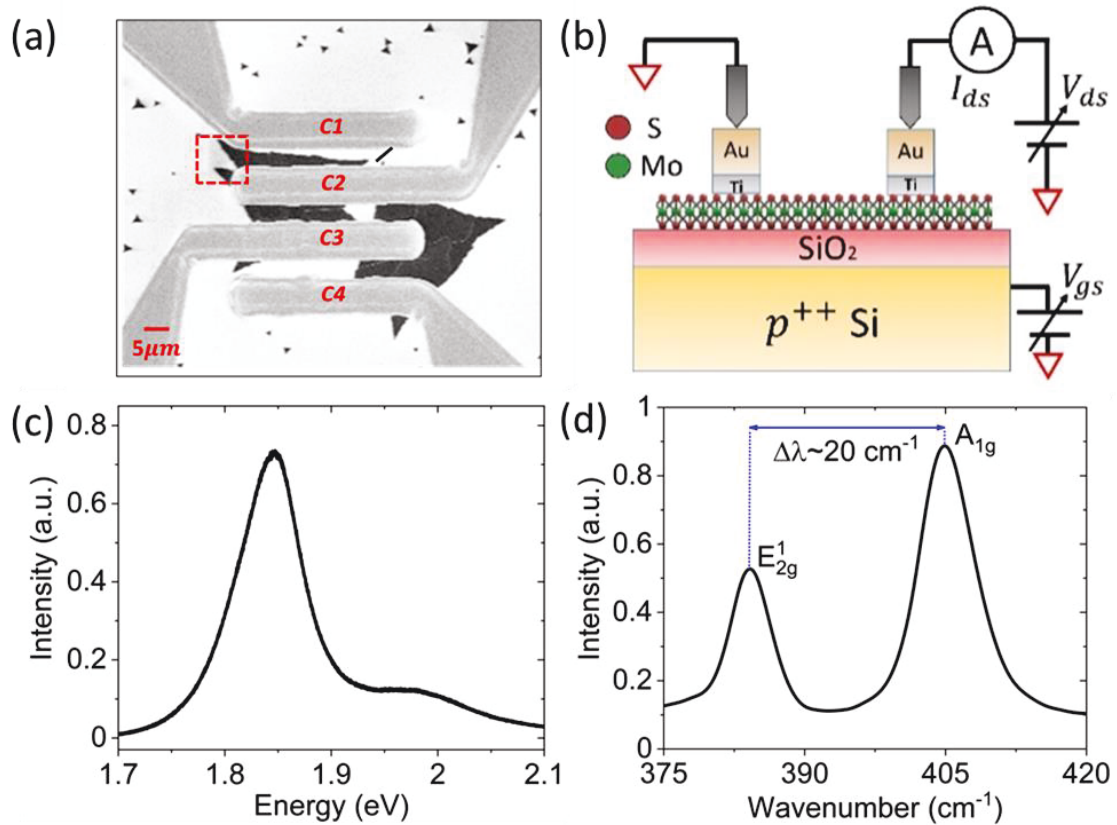
Figure 2.8 - (a) SEM images of the MoS₂ device. (b) MoS₂ FET layout and schematic of the common source configuration used for the electrical characterization. (c) Photoluminescence and (d) Raman spectra of monolayer MoS₂ before metal deposition.

In the following, the electrical characterization refers to the transistor between the contacts labelled as C2 and C3 in **Figure 2.8(a)**, where two flakes in parallel are involved. The contact C3 constitutes the drain and C2 the grounded source (**Figure 2.8(b)**). The red-dashed square in **Figure 2.8(a)** highlights the edge of the MoS₂ flake that was used for field emission measurements with the electrode C2 as the cathode and one of the SEM tips as the anode.

2.2.2. The effect of pressure

To prove the device as a pressure/gas sensor, the MoS2 FET has been standard characterized, measuring an output and a transfer characteristic in high vacuum (about 10^{-6} Torr). **Figure 2.9(a)**,

showing the output characteristic, suggests the formation of Schottky barriers at contacts, probably due to Fermi level pinning above the midgap of MoS_2 [115–117]. Besides, the device shows a n-type behavior, as displayed in **Figure 2.9(b)**, revealing an on/off ratio higher than five orders of magnitude, a subthreshold slope SS = 7.6 V/decade and carrier mobility up to 20 $cm^2V^{-1}s^{-1}$.

The n-type conduction is a well-known MoS_2 feature in literature, and it has been attributed to the Fermi level pinning as well as to the intrinsic n-doping of MoS_2 due to defects such as S vacancies.[116,118]
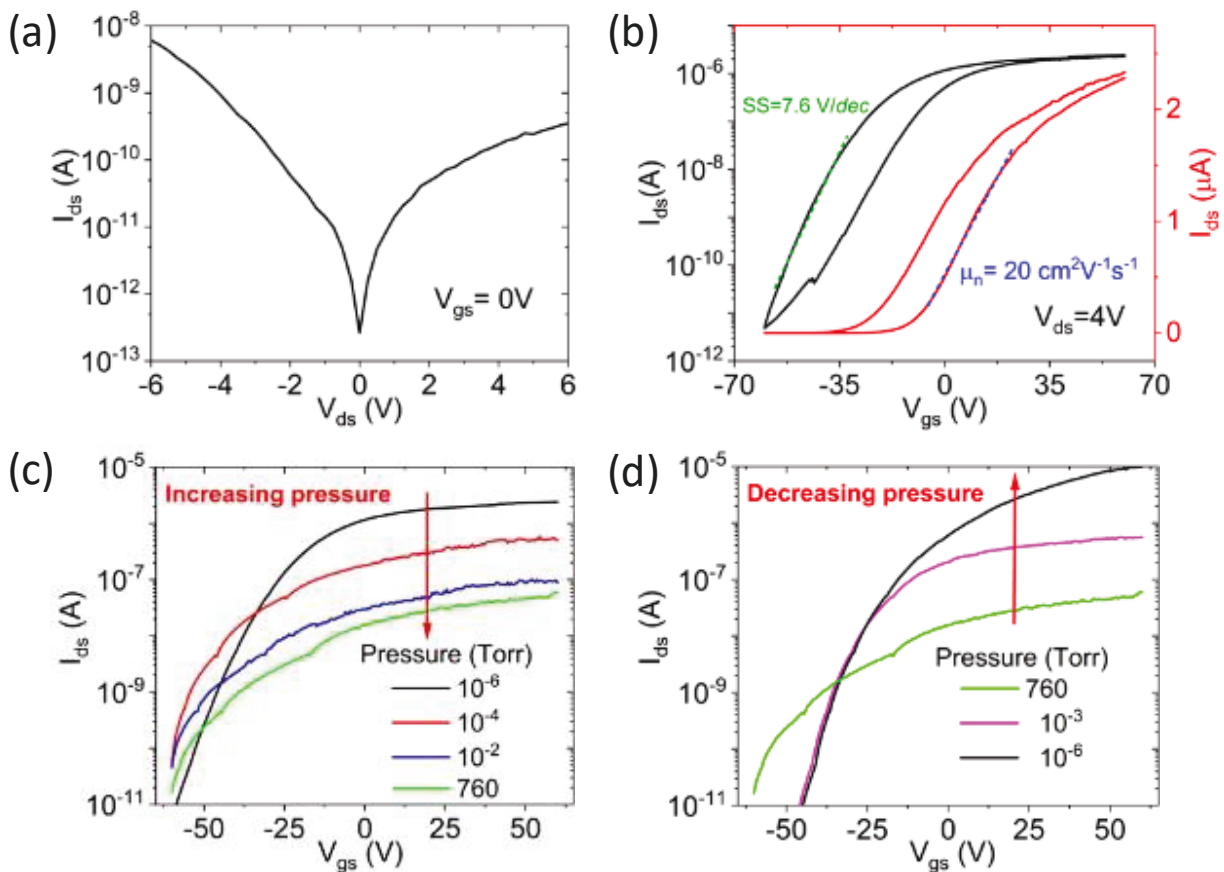
Figure 2.9 - Output (a) and transfer (b) characteristics of the device between C3 and C2 contacts, with C3 used as the drain and C2 as the grounded source. The transfer characteristic is shown on both logarithmic and linear scale. Transfer characteristics for (c) increasing and (d) decreasing air pressure.

If air is letting enter the chamber, air pressure raises, and it has effects on the current flowing in the channel. Going from 10^{-6} Torr to atmospheric pressure, the on current decreases, as reported

in **Figure 2.9(c)**. The effect of pressure is reversible as demonstrated by the set of curves of **Figure 2.9(d)**, measured for decreasing pressure. The degradation of conductance with increasing pressure, in some cases resulting in the dramatic transformation from n-type to p-type conduction, has been mainly attributed to adsorbed oxygen and water that act as interface traps and scattering centers with a density in the order of 10^{12} cm^{-2} eV^{-1} , reducing the n-type doping of the channel.[119–123]

2.2.3. Fowler-Nordheim Field Emission

Using a tip as anode and the contact C2 as the cathode (**Figure 2.10(a)**), a field emission current flows into the device. The tip was positioned at fixed distances from the edge of the flake, and the voltage on the tip was increased monitoring the current.

Figure 2.10(b) shows two sets of field emission current measurements performed at different anode-cathode distances, using the setup reported in the inset. They show repeatable FE current occurring with a 100-120 $V\mu m^{-1}$ turn-on field, defined as the field to which the current emerges from the noise floor.

According to the Fowler–Nordheim (FN) model, the FE current from a semiconductor can be described as:[124]

$$I_{FE} = Sa\frac{E_S^2}{\chi}e^{-b\frac{\chi^{3/2}}{E_S}} \qquad\qquad (2.3)$$

where S is the emitting surface area, $a = 1.54 \times 10^{-6}\ A\,V^{-2}\text{eV}$ and $b = 6.83 \times 10^7\ V\,cm^{-1}\ eV^{-3/2}$ are constants, $E_S\ (Vcm^{-1})$ is the electric field at the emitting surface and χ is the electron affinity of the emitting material. The electric field $E_S = \beta\frac{V}{k\cdot d}$, with β the so-called

field enhancement factor, i.e. the ratio between the electric field at the sample surface and the applied field $V/(k \cdot d)$, and $k \sim 1.6$ a phenomenological factor accounting for the spherical shape of the tip.[125,126]

The Fowler–Nordheim equation (**Equation(2.3)**) leads to the linear behaviour of the so-called FN plot of $ln(I_{FE} V^{-2}) \, vs. \, V^{-1}$ of **Figure 2.10(c)**, which allows estimating the β factors as 16.5 and 17.0 for 200 nm and 400 nm distances, respectively. FE current stability is demonstrated for about 25 minutes in **Figure 2.10(d)**, with a standard deviation of about 15%.
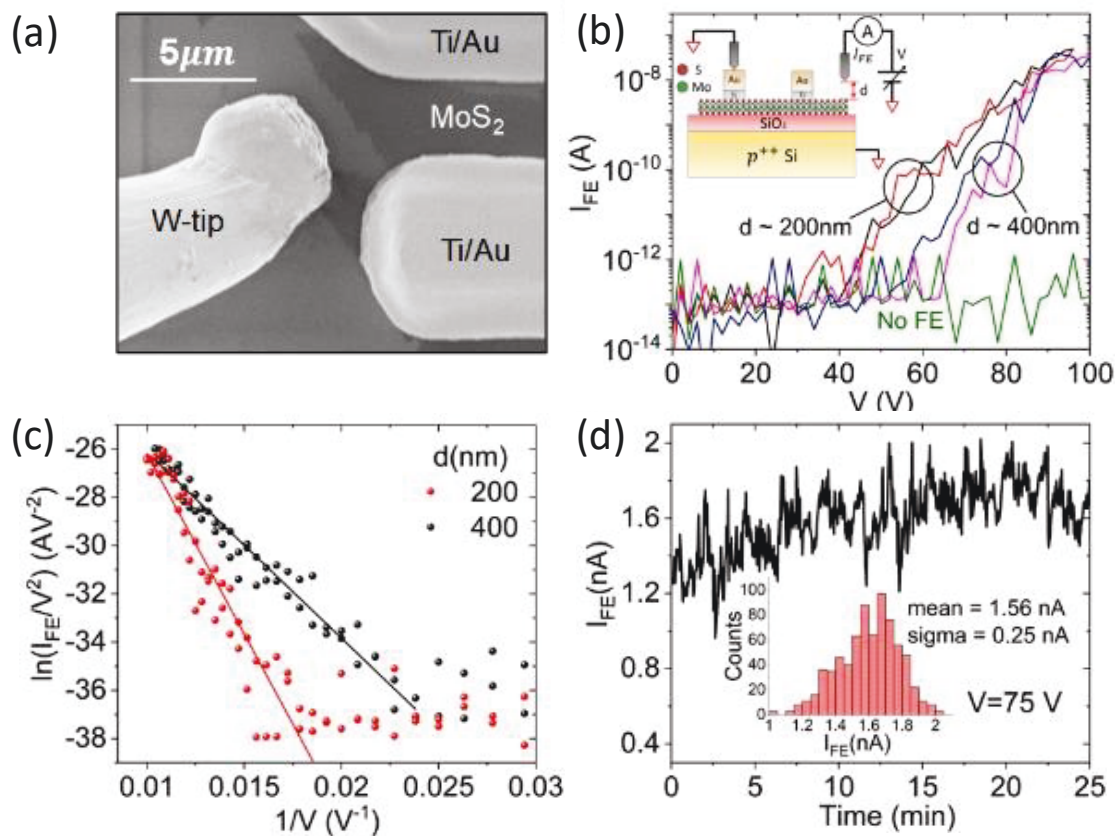
Figure 2.10 - (a) SEM image of the MoS2 flake used for the measurement of field emission. The W-tip works as the anode while the Ti/Au lead is the cathode. (b) Field emission measurements performed at two different distances using the setup in the inset. (c) Fowler-Nordheim plot reveals a field enhancement factor of about 16.5 and 17.0 at distances 200 nm and 400 nm distances, respectively. (d) Field emission current stability with the tip anode at distance d=200 nm and with 75 V bias. In the inset the histogram with standard deviation of about 15%.

2.2.4. Gate controlled Field Emission

The MoS2 channel can be electrically n-doped by applying a positive voltage on the back gate. If conduction electrons increase, the tunneling probability also increases, thus increasing the field emission current.

Figure 2.11(a) confirms an increasing field emission current for increasing gate voltages.
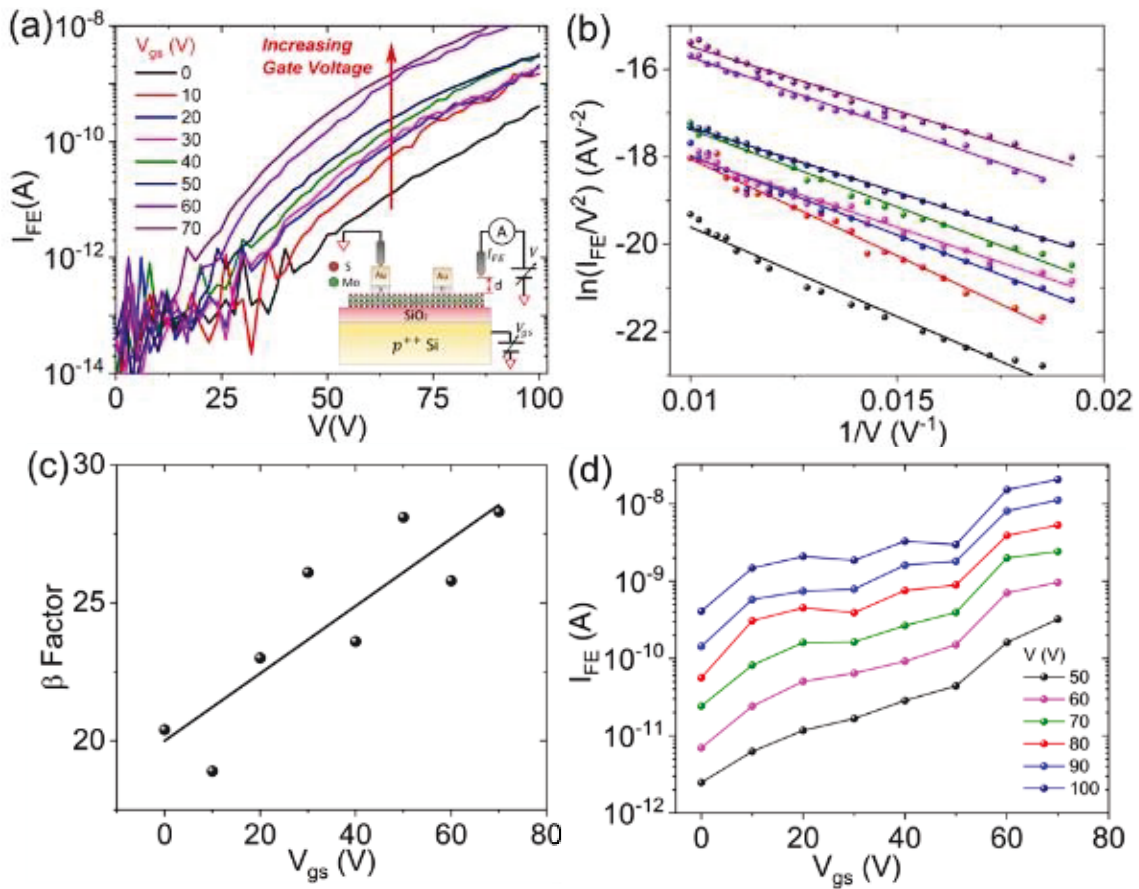
Figure 2.11 - (a) *Field emission current measured at d=200 nm for increasing gate voltage. A schematic of the used setup is shown in the inset. (b) Corresponding Fowler-Nordheim plot showing linear behaviour of the $ln(I_{FE}V^{-2})$ vs. V^{-1} curves. (c) Field enhancement factor as a function of the gate voltage. (d) Transfer characteristics at various anodic voltages V showing the exponential growth of the FE current for increasing V_{gs}.*

Figure 2.11(b-c) show the corresponding FN plot and the extracted field enhancement factor, respectively. The field enhancement factor grows with increasing V_{gs}, but it is an artifact related to the enhanced MoS$_2$ doping level rather than to a real field enhancement. These results provide

the proof-of-concept of a new MoS$_2$ FET based on FE. The transfer characteristic of the device, at different anode voltages V, are shown in

Figure 2.11(d).

These results can be explained considering that the applied gate and anode voltages lower the MoS$_2$ electron affinity, as follows:

$$\chi' = \chi - CV_{gs} \qquad (2.4)$$

where $\chi = 4.2\ eV$ is the electron affinity at zero bias, and C is a constant which accounts for the gate efficiency. The applied voltage also reduces the barrier width, as displayed in Figure 2.12(a).

Substituting **Equation (2.4)** in **Equation(2.3)**, the FE current can be written as:

$$I_{FN} = A \left(\frac{1}{\chi - CV_{gs}} \right) e^{-B(\chi - CV_{gs})^{\frac{3}{2}}} \qquad (2.5)$$

where we have introduced the new constants $A = Sa\beta^2/(kd)^2$ and $B = bkd/\beta$ for simplicity. **Figure 2.12(b)** confirms the consistency of the model, showing how **Equation(2.5)** fits the experimental data.
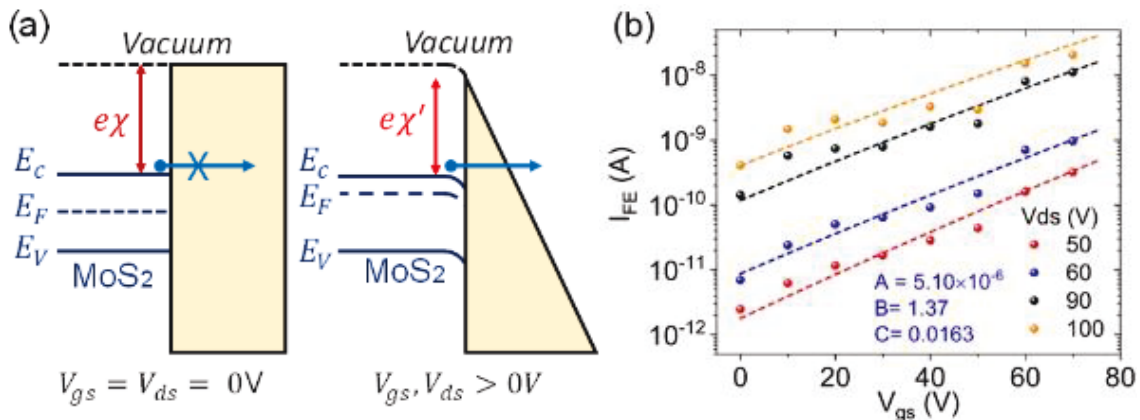

Figure 2.12 - (a) MoS$_2$-vacuum band diagram at zero bias and at positive gate and anode bias. The applied voltages reduce the MoS2 electron affinity as well as the barrier width (coloured shapes) enabling electron tunneling. *(b)* Subset of data of

56

Figure 2.11(d) with fit provided by *Equation(2.5*), demonstrating the consistency of the proposed model.

2.3. Platinum diselenide FET

$PtSe_2$ falls within the so-called noble TMDs formed by Group-10 noble elements (Pt, Pd, and so on) and chalcogens (S, Se, or Te). The main peculiarity of noble TMDs is that d-electrons completely occupy their d-orbitals, resulting in the highly hybridized P_z orbitals and strong interlayer interaction. Therefore, they present relatively small and widely tuneable bandgaps compared to traditional TMDs, which combined with high mobility and environmental stability make them of great interest for possible optoelectronic applications. For these reasons, $PtSe_2$, is currently the subject of intense research activity.[127–129] Bulk $PtSe_2$ is a gapless semimetal[130] for which theoretical studies have predicted a band gap emergence when reduced to monolayer.[131] Wang et. Al. through epitaxial growth by direct selenization of the material experimentally demonstrated that monolayer $PtSe_2$ has a band gap of $1.2\ eV$.[132] Due to its thickness-dependent semimetal-to-semiconductor transition, $PtSe_2$ is a suitable candidate for electronic[133] and optoelectronic applications.[134] Nowadays, $PtSe_2$ is attracting great research attentions due to its high carrier mobility[129], high chemical activity,[135] and low formation temperature.[136] Yim et al. have shown that $PtSe_2$ films, transferred onto silicon substrates, form diodes working as both photodetectors and photovoltaic cells.[137] Furthermore, theoretical studies have indicated that $PtSe_2$ has adsorption energy for gases like NO_2 and NH_3 lower than MoS_2 and graphene.[138] Su et al. have recently reported stable gas sensing performance of $PtSe_2$ under strains induced by different selenization temperatures.[139] $PtSe_2$ has weak chemical reactivity with oxygen that is physically adsorbed on its surface and can be removed by vacuum annealing, heating, or irradiation.[140] The interaction of O_2 with $PtSe_2$ is an important process to understand because it can deeply affect the transport properties of the material. The adsorption process does not lead to structural or chemical changes of the material but induces p-type doping as electrons can transfer to oxygen molecules and cause hole formation inside $PtSe_2$.

In the next paragraphs, the effect of temperature, air pressure, and light irradiation on the transport properties of multilayer $PtSe_2$ back-gated field-effect transistors are reported. The devices show p-type conduction and electrical conductivity that increases with the rising temperature and air pressure. They exhibit both negative and positive photoconductivity, depending on the air pressure. Negative photoconductivity (NPC) is observed at atmospheric pressure as light irradiation by a white source reduces the $PtSe_2$ conductance. Conversely, in high vacuum, the material exhibits positive photoconductivity (PPC). The physical origin of this mechanisms is the pressure- or light-induced desorption of oxygen, which acts as a charge transfer dopant, affecting the $PtSe_2$ conductance. To provide atomistic insight, first principles calculations have been performed to study the interaction of physisorbed oxygen molecules with semiconducting $PtSe_2$. They demonstrate that adsorption of oxygen on $PtSe_2$ surface induces holes in the $PtSe_2$ material, increasing its conductivity, consistently with the experimental observations.

2.3.1. Sputtering and selenization processes

Sputtering has been used to obtain a homogeneous Pt film (nominal thickness $0.7\ nm$). Pt was directly sputtered over an Si/SiO_2 substrate (85 nm thermally grown oxide on p-type silicon, $\rho \sim 0.001 - 0.005\ \Omega cm$). After that, a direct selenization process inside a two-zone furnace was performed. The upstream zone with Se pellets was heated to $220\ °C$ while the downstream zone housed the Pt film at $400\ °C$ for the selenization process.[137] The obtained Se vapor was carried to the downstream zone through an $Ar{:}H_2$ (90%:10%) flow at 150 sccm, where it reacted with the Pt films for 2 hours to completely convert it into a $PtSe_2$ ultrathin film. During the process, the Se infiltrated into the Pt film causing the formation of $PtSe_2$ and a film thickness expansion by a factor of ~ 3.5– 4.[141] Then, the compound was cooled down to room temperature. The final

thickness of the $PtSe_2$ film, as revealed by TEM analysis, is about $3\,nm$ corresponding to 6 layers.[142]

A polymer-based process was used to transfer the obtained $PtSe_2$ film onto a fresh Si/SiO_2 substrate. Hence, SF_6-based inductively coupled plasma etching process with photoresist masking was performed to obtain the desired pattern. Standard photolithography and lift-off processes were carried out to fabricate $Ni{:}Au$ ($20\,nm{:}150\,nm$) metal contacts. The highly doped Si substrate was used as the gate electrode. An optical image of the device is shown in the inset of Figure (2.1 d).

2.3.2. Photoconductivity measurements and DFT calculation setups

For the electrical characterization, devices were measured in two- and four-probe configurations in a Janis Probe Station (Janis ST-500 probe station) equipped with four nanoprobes connected to a Keithley 4200 SCS (semiconductor characterization system), working as source-measurement unit with current sensitivity better than 1 pA. The electrical measurements were performed by lowering the pressure from $1\,bar$ (room pressure) to $10^{-5}\,mbar$ and at different temperatures from 292 K to 392 K. The air in the chamber was evacuated by a rough and a turbo pump. The photoconductivity was tested by irradiating the devices with a super-continuous white laser source (NKT Photonics, Super Compact, wavelength ranging from $450\,nm$ to $2400\,nm$, at $50\,mW/mm^2$).

First-principles calculations were performed within the framework of density functional theory (DFT) as implemented in QuantumATK.[143] Linear combination of numerical atomic-orbital (LCAO) basis set and generalised gradient approximation (GGA) with norm-conserving pseudopotentials from PseudoDojo[144] were employed in the simulations, where the semi-core 2s, 2p and 3d states for oxygen, 5s, 5p, 5d, 4f, 6s and 6p states for Pt, and 4s, 4p, 4f, and 3d states for Se have been

retained as valence electrons. Brillouin-zone integrations were performed over a grid of k points

generated according to the Monkhorst-Pack scheme[145] with a density of approximately 12 k-points

per angstrom. Energy cut-off of 125 Ha has been considered for discretized grid and all structural

relaxation was performed with the maximum force of less than $0.005 \, eV \, Å^{-1}$.[146] Van der Waals

correction to the GGA functional[147] to correct the London dispersion is adopted for analysing the

oxygen functionalization of $PtSe_2$. To analyse the effects of the oxygen adsorbate on $PtSe_2$

surface, a single oxygen molecule on a 3 × 3 × 1 bilayer $PtSe_2$ supercell, corresponding to the

density of ~$9 \times 10^{13} \, cm^{-2}$, has been considered. The slab in the supercell is infinite and periodic

in the x- and y-directions (parallel to the slab surface) and is finite along the z-direction (normal to

the slab surface). The thickness of the vacuum region along z-direction is larger than 20 Å to avoid

any interaction between the periodic images of the neighbouring films. In the slab model

calculation with adsorbate on the surface, an artificial macroscopic electrostatic field exists due to

the periodic boundary conditions.[148] In order to avoid this artificial field in the $PtSe_2$ slab with

oxygen molecule on the surface, we considered mixed Neumann and Dirichlet boundary

conditions at the oxygen and $PtSe_2$ sides of the slab, respectively, which provides an alternative

approach for the dipole correction in the slab calculations.[143]

2.3.3. Basic transistor characterization

Among the typical TMDs morphologies discussed in the Chapter 1, $PtSe_2$ presents a 1T crystal

structure with octahedral coordination (in which six selenium atoms are bonded to a platinum

atom located at the centre, as shown in **Figure 2.13(a)**), resulting in a Pt layer sandwiched

between Se layers.[149] Transmission electron microscope (TEM) was used to collect an image of the

$PtSe_2$ flake used for the electrical characterization, as shown in **Figure 2.13(b)**, revealing a

thickness of about 3 nm corresponding to 6 atomic layers.[142]

First, to investigate the basic properties of the transistor at room temperature, output and transfer characteristics have been measured. They are reported in **Figure 2.13(c-d).**

The output characteristics exhibit a linear behaviour (**Figure 2.13(c)**). The application of the gate voltage affects the overall conductance of the transistor, showing a typical p-type behaviour with higher conductance at negative V_{gs}. This is reported in the transfer characteristic (**Figure 2.13(d)**), where the gate voltage range (from $-2V$ to $+2V$) was intentionally limited to avoid leakage or breakdown of the 85 nm gate oxide.
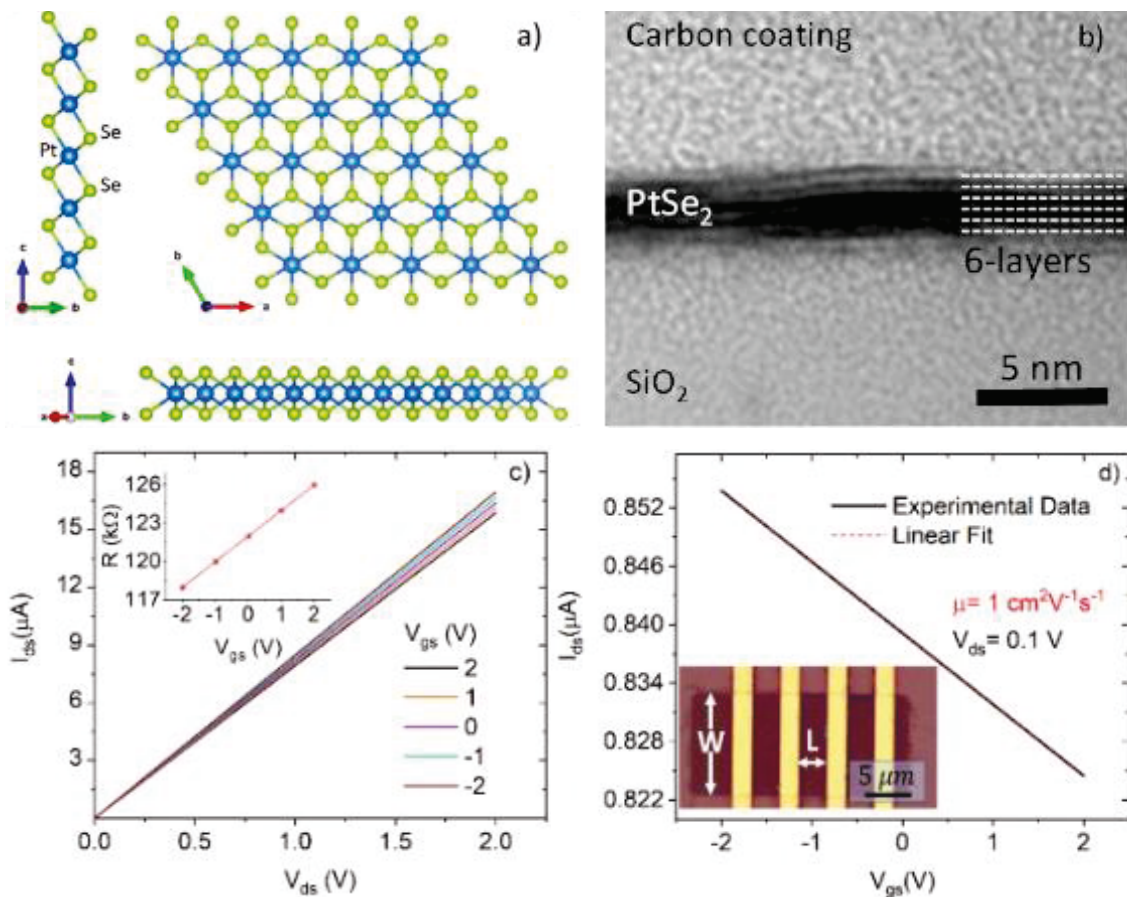
Figure 2.13 - *(a) Crystal structure of two-dimensional $PtSe_2$ showing an octahedral geometry with six selenium atoms bonded to a platinum atom located at the centre. (b) TEM image of a $PtSe_2$ film revealing a thickness of about 3 nm corresponding to 6 layers. (c) Output characteristics acquired in 2-probe configuration for different gate voltages. The inset shows the channel resistance as function of the gate voltage. (d) Transfer characteristic recorded at $V_{ds} = 0.1\,V$. The dashed red line shows the linear fit used to obtain the field-effect mobility. The inset shows an optical image of the device. W and L represent the width and the length of the selected channel, respectively.[3]*

The intrinsic p-type doping has been reported in previous works and can be attributed to Pt or Se vacancies and to the effect of oxygen adsorbates on the channel surface.[133,140,141] Furthermore, the use of Ni as the contact material facilitates hole injection as the Ni Fermi level aligns to the top of the valence band of $PtSe_2$. The field-effect mobility, defined in **Equation(1.11)**, has been obtained through the linear fit of the transfer curve (where $L = 4\,\mu m$ and $W = 10\,\mu m$ were channel length and width, respectively, $C_{ox} = \frac{\epsilon_0 \cdot \epsilon_{SiO_2}}{t_{SiO_2}} = 4.06 \cdot 10^{-8} \frac{F}{cm^2}$ was the capacitance per unit area of the gate dielectric with $\epsilon_0 = 8.85 \cdot 10^{-14} \frac{F}{cm}$, $\epsilon_{SiO_2} = 3.9$ and $t_{SiO_2} = 85\,nm$ the vacuum permittivity, the SiO_2 relative permittivity and thickness, respectively; $V_{ds} = 0.1\,V$ is the voltage bias between drain and source). The obtained $\mu_{FE} \approx 1\,cm^2 V^{-1} s^{-1}$ is comparable with the other fabricated $PtSe_2$ devices.[141,150]

2.3.4. Temperature and pressure dependent electrical properties

To investigate how temperature and pressure influence the $PtSe_2$ electrical transport properties, output and transfer characteristics were measured in the $292 - 392\,K$ temperature range and at different air pressures of 10^3, 1 and $10^{-5}\,mbar$. An increasing current/conductance with both rising temperature and air pressure was found, without any other apparent change in the behaviour of the device. **Figure 2.14(a)** shows that the conductance G increases as the temperature rises, confirming a semiconducting behaviour. The air pressure also affects the conductance of the device. Indeed, the device is more conductive at atmospheric pressure than in vacuum. This effect is caused by oxygen that acts as a p-type dopant for the material,[151] but it will be further discussed in the next paragraphs.
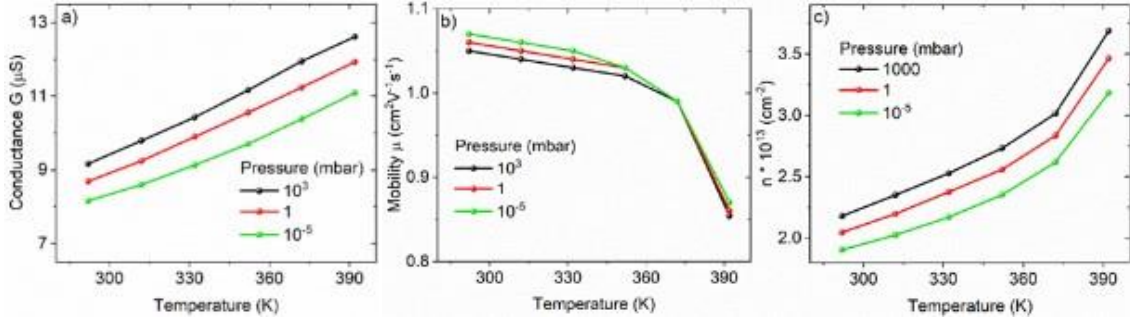
Figure 2.14 – **(a)** Channel conductance, **(b)** field-effect mobility and **(c)** carrier density as a function of temperature for $1\ bar$ (black dots), $1\ mbar$ (red dots), $10^{-5}\ mbar$ (green dots).[3]

Figure 2.14(b) shows that the mobility depends weakly on environmental pressure below 350 K and also depends on temperature[152]. When the temperature rises beyond 350 K, ionized impurity scattering and phonon scattering balance each other with a slight predominance of phonon scattering, which becomes relevant.

Having obtained $\mu_{FE}(T)$ and $G(T)$ at each of the considered pressures, it is possible to estimate the carrier density per unit area n (in cm^{-2}) as a function of temperature for each pressure from the following equation:

$$n(T) = \frac{1}{q\rho(T)\mu(T)}$$

(2.6)

The carrier density, reported in **Figure 2.14(c)**, shows the typical semiconductor behaviour, as it increases with the rising temperature. The obtained carrier concentration of about $10^{13}\ cm^{-2}$ is comparable with the one reported from Hall measurements carried out on similar devices.[133] Moreover, at atmospheric pressure, the carrier density is larger than in high vacuum. This could be due to enhanced adsorption of oxygen on the channel surface at higher pressure that leads to increased p-type doping.

2.3.5. Light irradiation response: negative photoconductivity

Apart from the standard characterization, the investigation was focused on the $PtSe_2$ electrical response to light irradiation. **Figure 2.15(a)** shows $I_{ds} - V_{ds}$ characteristics measured at air pressures of $1\ bar$ and $10^{-5}\ mbar$ both in dark and under white light irradiation. In high vacuum the light irradiation causes an increase in the conductivity as expected for a semiconducting material. Conversely, at atmospheric pressure, a reduction in conductivity, i.e., a negative photoconductivity, is observed under illumination.

The linearity of the output characteristics of **Figure 2.15(a)** indicates and ensures that the current is not reduced by the formation of a Schottky barrier at metal/$PtSe_2$ interface but rather by a decrease in channel conductivity.

To further investigate the optoelectronic behaviour of $PtSe_2$, the electrical conduction of the device under light irradiation at different air pressures was measured. The super-continuous light source power was set to $20\ mW/mm^2$ and switched on and off every 3 minutes.

Figure 2.15(b) shows the device channel current under irradiation, measured at $V_{ds} = 0.1\ V$ and $V_{gs} = 0\ V$. At the pressure of 10^{-5} mbar, the device exhibits a photocurrent of $\sim 80 nA$. At this pressure regime, photocurrent is likely dominated by extrinsic photoexcitation, i.e. transitions involving deep trap states, which increases the material conductivity with a characteristic time of $72\ s$. Photoexcitation from deep trap states can result in long response times[153]. Indeed, photocurrent with rising and falling times of dozens seconds have been reported in similar devices with 2D materials such as MoS_2[154,155] or ReS_2[153,156]. From first-principles calculations, it has been demonstrated that the formation of deep trap states can be caused by Se antisites at Pt sites, as well as by Pt and Se vacancies[142].
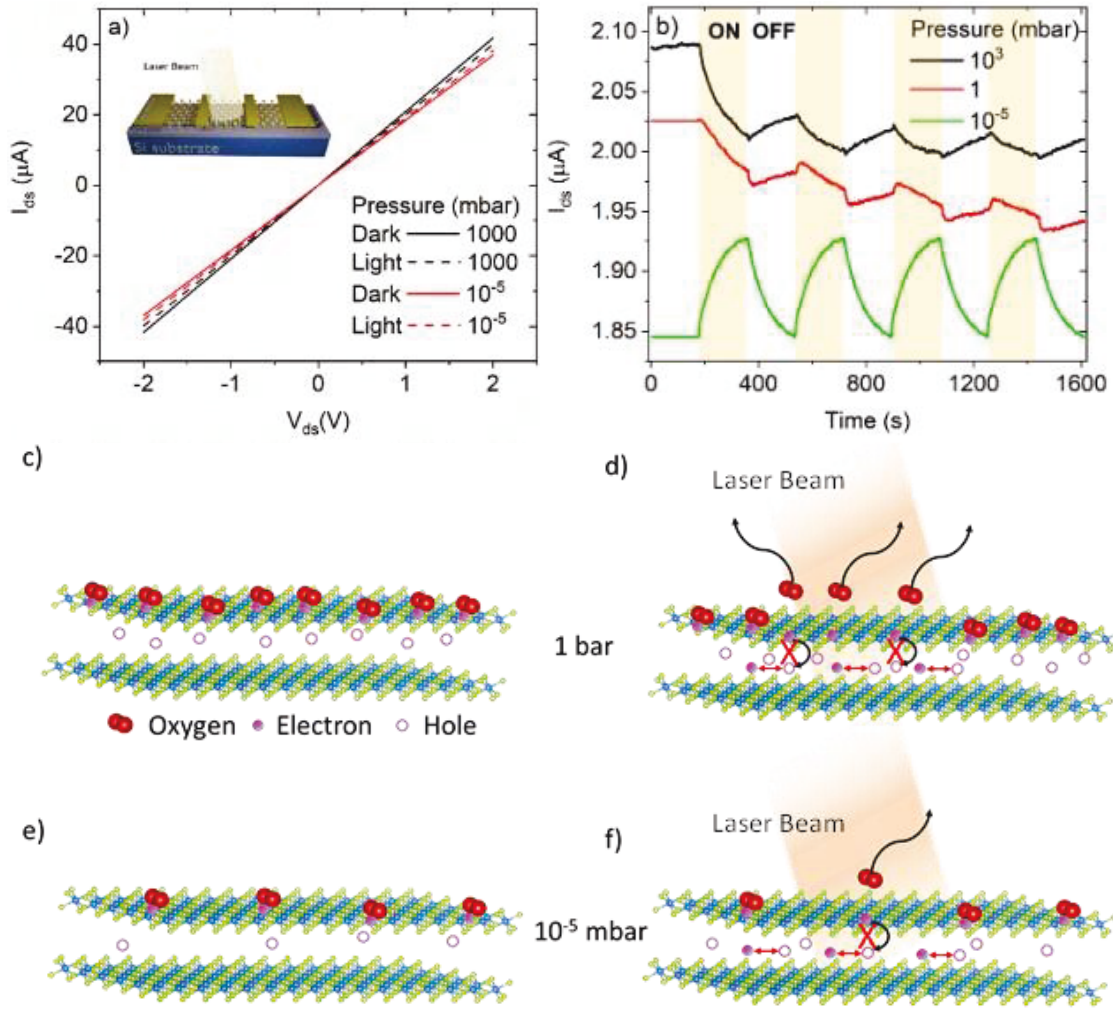
Figure 2.15 – (a) $I_{ds} - V_{ds}$ *characteristics in dark (continuous lines) and under super-continuous 450-2400 nm light source irradiation (dashed lines), recorded at* $1\ bar$ *(black lines) and* $10^{-5}\ mbar$ *(red lines). The inset shows a schematic of the device under light irradiation. The laser spot of about* $1\ mm^2$ *was located between the two contacts to completely cover the channel.* ***(b)*** *Current vs time characteristics at* $10^3\ mbar$ *(black line),* $1\ mbar$ *(red line),* $10^{-5}\ mbar$ *(green line) under switching light. The laser was switched on (yellow zone) and off (white zone) every 3 minutes.* ***(c)*** *At* $1\ bar$*, in dark, the large amount of oxygen adsorbed on* $PtSe_2$ *traps electrons at the surface and induces p-type doping in the material.* ***(d)*** *When the device is exposed to light, oxygen is removed from the surface. Free electrons are trapped or recombine with holes reducing the density of available carriers and resulting in a negative photoconductivity.* ***(e)*** *At* $10^{-5}\ mbar$ *the amount of adsorbed oxygen is limited and so is the p-type doping of the material.* ***(f)*** *When the device is exposed to light, the photogenerated electron-hole pairs and charge-carrier detrapping increase the conduction in the material, leading to a positive photoconductivity.[3]*

When the light is switched off, recombination and carrier trapping make the current to return to

its initial value. The photoresponsivity R of the device (defined in the following paragraph 3.2.1)

(with $P_\lambda = 0.8\ \mu W$) is $\sim 0.2\ \frac{A}{W}$, comparable with similar phototransistor realized with both $PtSe_2$

and different 2D materials. Indeed, Wang et al.[157] reported a low photoresponsivity of $0.19 \frac{mA}{W}$ for $PtSe_2$ phototransistors measured under incident light at $1550 \, nm$ and when $V_D = 5 \, V$, mainly ascribed to insufficient absorption of incident light of the material. Yu et al. showed that such absorption, and thus the photoresponsivity, can be improved by hybridizing $PtSe_2$ with a photonic waveguide.[158] A good way to enhance the photoresponsivity is the use of different substrates. Indeed, Li et al.[159] reported that few-layer $PtSe_2$ on $h - BN$ substrate can reach a photoresponsivity as high as $1.56 \cdot 10^3 \, A \, W^{-1}$. Similar studies, conducted on other 2D materials, have demonstrated that the photoconductivity can range from few $\frac{mA}{W}$ from graphene-based devices[160] until to $10^6 \frac{A}{W}$ for black-phosphorus photodetectors.[161]

At the pressure of $1 \, mbar$, a different behavior is observed. The higher dark current can be ascribed to the interaction between the material surface and the environmental oxygen. When the light is switched on, a sudden increase, appearing as a small step-up, is observed in the current. Such a step is followed by a steady decrease. When the light is switched off, the current suddenly drops with an analogous small step-down and then increases slowly, without attaining its initial value. The successive light pulses result in a further overall decrease of the current.

A similar, but more dramatic behaviour, is observed at atmospheric pressure. In this case, when the device is illuminated, the current decreases faster and recovers only partially when the light is switched off.

The reduction of current during illumination is known as negative photoconductivity and has been observed in other materials.[162,163] Its origin has not yet been fully understood although most studies attribute it to a photogating effect,[151] an electronic transition to the defect state levels[164] or interaction with adsorbates.[165,166]

The photogating effect is observed when electron-hole photogeneration occurs in Si or $PtSe_2$ followed by charge trapping at the interface with SiO_2. Indeed, favoured by the vertical up-bending of the Si bands, photo-generated holes can be trapped at the Si/SiO_2 interface acting as a positive gate that lowers the channel conductance.[151] However, this phenomenon should be independent of the external pressure.

Even if rise and fall time are quite long, the conductance modulation cannot be due to light induced heating and cooling. Indeed, **Figure 2.14(a)** shows that the conductivity of the device increases with the temperature independently from the external pressure, hence a thermal effect would not be able to explain the negative photoconductivity at atmospheric pressure. Although the photogating and the thermal effects could play a role, the results of **Figure 2.15(b)** suggest that other mechanisms take place and dominate the optoelectronic behaviour of $PtSe_2$. The dependence on pressure suggests that such mechanisms involve adsorption and desorption of air molecules.[140]

Figure 2.15(c-d-e-f) display the physical mechanisms behind this phenomenon. At atmospheric pressure there is a large amount of oxygen molecules adsorbed on the material surface, as shown in **Figure 2.15(c)**. Such adsorbates attract free electrons from $PtSe_2$ leaving holes inside the material. These holes are responsible for the p-type conductivity and the higher carrier density measured at atmospheric pressure. When the material is exposed to light, oxygen is easily removed from the surface[167] and the free electrons can recombine with the holes in the material, as shown in **Figure 2.15(d)**. A similar behaviour has been already reported for MoS_2 phototransistors.[168] Indeed, it has been shown that the use of sufficiently short wavelength light source causes desorption of water and oxygen molecules affecting both the responsivity and the response time of the devices. Moreover, although not explicitly shown in **Figure 2.15(d)**, the presence of environmental humidity, which can be removed through light illumination[168], can also

affect the conductivity of the device acting as positive dopants. The outcome of the process is a decrease in the total concentration of carriers which results in the observed decrease in the conductivity of the material.

When the pressure is decreased to $10^{-5}\ mbar$, adsorbed oxygen is partially removed from the surface resulting in the reduced conductivity of the material, as shown in **Figure 2.15(e)**. In this case, when the channel is exposed to light, the dominant process is the photogeneration of electron-hole pairs and charge detrapping. The excess carriers increase the conductivity of the material, leading to the observed positive photoconductivity (**Figure 2.15(f)**).

At the intermediate pressure of $1\ mbar$ both processes coexist. Indeed, when the light is first turned on, a step-up in conductivity is observed due to the photogeneration of electron-hole pairs, which is a fast process. Then, the neutralization and desorption of oxygen, which is a slower process, induces a slow decrease of current. When the light is switched off, a step-down in the current is caused by excess electron-hole recombination, followed by a slower current increase due to oxygen re-adsorption on the $PtSe_2$ surface.

2.3.6. DFT calculations: the effect of physisorbed oxygen

In this paragraph, the results from DFT calculations that were used to clarify the impact of physisorbed oxygen molecules on the semiconducting $PtSe_2$ surface are reported. A single oxygen molecule on a bilayer $PtSe_2$ supercell has been considered. Although the experimental film is composed by 6-layers, the DFT calculations was performed on bilayer $PtSe_2$ because of the well-known underestimation of the bandgap in DFT-based calculations.[133] Thinner (bilayer) $PtSe_2$ was considered in the DFT calculations to be consistent with the experiments in achieving semiconducting film with comparable bandgap values. As the size of the supercell is larger than the primitive cell, the corresponding first Brillouin zone is smaller. Hence, the $PtSe_2$ slab plus

oxygen molecule band structure (supercell structure) is "folded" into the first Brillouin zone. Consequently, to be able to directly compare the folded bands with the reference band structure of the $PtSe_2$ primitive cell, i.e. $PtSe_2$ unit cell without oxygen adsorbate, a procedure known as "unfolding" has been employed to unfold the primitive cell Bloch character hidden in the supercell eigenstates.[169,170] The unfolded band structure of the $PtSe_2$ slab plus oxygen molecule is displayed as a contour plot in **Figure 2.16(a)**. The primitive $PtSe_2$ band structure is shown by white dashed lines as reference in this figure and the energies are referenced to the Fermi energy (E_F). As can be conspicuously seen by comparing the two band structures, the unfolding method reveals a rather remarkable shift of the E_F towards lower energies, i.e., p-type characteristic, due to the presence of the oxygen adsorbate, while the band structure of the $PtSe_2$ is rather unperturbed.

Figure 2.16(a) also shows the oxygen molecule-induced states are created near the EF closer to the $PtSe_2$ valence band edge. The nature of these states can be identified through the unfolded band structure, where these states exhibit expected almost dispersionless energy states in the band structure. The density of states (DoS) at the same energy window, with and without the oxygen molecule on the $PtSe_2$ surface, are presented in **Figure 2.16(b)**, illustrating the band alignment of the two structures. The occupied double states shown in green are associated with the physisorbed oxygen molecule.
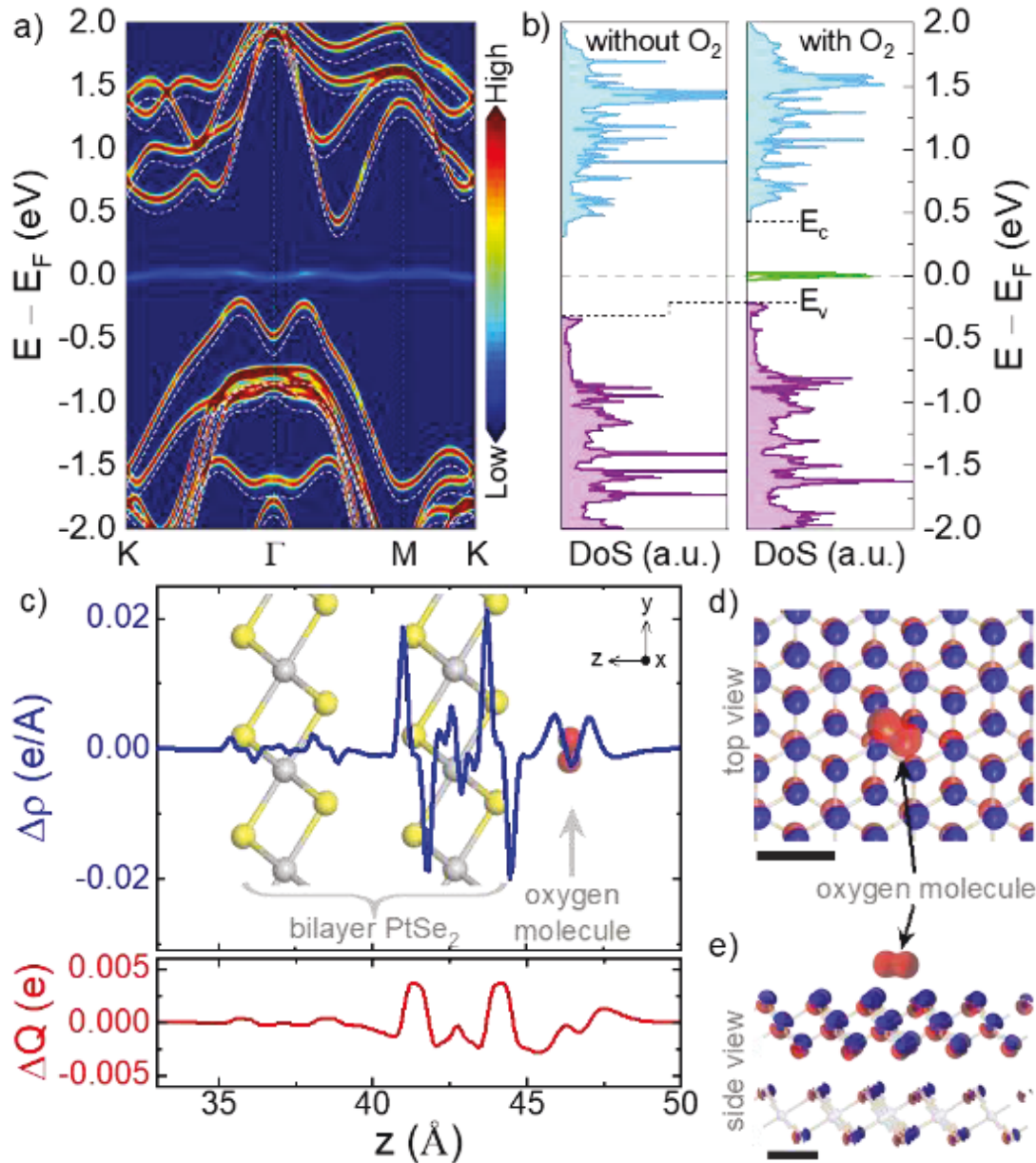
Figure 2.16 - ***(a)*** *Unfolded band structure of the semiconducting $PtSe_2$ with a physisorbed oxygen molecule on the surface using a contour plot of total weight intensity as a function of wave vector in the two-dimensional Brillouin zone. Red (blue) represents high (low) spectral weights. The band structure of the $PtSe_2$ without an oxygen molecule is shown using white dashed lines. Energies are referenced to the Fermi energy.* ***(b)*** *DoS of the $PtSe_2$ film with and without oxygen adsorbate on the surface. The Fermi level is at the zero of energy as shown by the grey dashed line. The p-type character of the system with an oxygen molecule is evident. The energy states illustrated in green correspond to the oxygen molecule.* ***(c)*** *Plane-averaged charge difference density ($\Delta\rho$) superimposed on the $PtSe_2$ atomic structure with an oxygen molecule, aligned to the z-direction (x-axis) (upper panel in blue) and charge transfer (ΔQ) (lower panel in red) of the structure referenced to the PtSe2 supercell without oxygen molecule.* ***(d)*** *and* ***(e)*** *Top-view and side-view of the $0.07\ e/Å^3$ CDD isosurface, demonstrating the effects of oxygen adsorbate on the charge distribution in the lateral direction (x-y plane) and along the z-direction, respectively. Red (blue) represents accumulation (depletion) of electrons referenced to the $PtSe_2$ supercell without oxygen molecule. Scale bars in d) and e) are 3.78 Å.[3]*

To quantify the charge transfer to/from the molecule, plane-averaged charge difference density (CDD), $\Delta\rho(z)$, along the z-direction is calculated by integrating $\Delta\rho(r)$ within the x-y plane. Accordingly, for a plane located at distance z normal to the $PtSe_2$ plane, the amount of charge transfer is obtained using $\Delta Q(z) = \int_{-\infty}^{z} \Delta\rho\,(z')\,dz'$. To analyse the charge interaction between the oxygen adsorbate and the semiconducting $PtSe_2$ film, the plane-averaged $\Delta\rho(z)$ referenced to the $PtSe_2$ supercell without oxygen adsorbate, is plotted together with the amount of charge transfer $\Delta Q(z)$ in the upper and lower panel of **Figure 2.16(c)**, respectively. As can be seen, the oxygen molecule acts as an electron acceptor by gaining $\sim 0.004\ e$ at the interface from $PtSe_2$ (e is the elementary charge of an electron). The top-view and side-view of the iso surface of the CDD, referenced to the $PtSe_2$ supercell without oxygen adsorbate, are depicted in **Figure 2.16(d-e)**, respectively, where red (blue) represents accumulation (depletion) of electrons. Notably, although the lateral redistribution of charges upon oxygen adsorption is quite negligible (see top-view image in **Figure 2.16(d)**, there is a distinct charge redistribution, particularly between the oxygen molecule and the top layer of the bilayer $PtSe_2$ as can be seen in the side-view (**Figure 2.16(e)**).

3. Schottky Diodes and Heterostructures for photodetection

In this chapter Schottky diodes and heterostructures made for photodetection application are taken under study. First, some general theory about photogeneration is presented, relying on how Schottky diode can be used as photodetectors and also introducing some useful figures of merit like responsivity and external quantum efficiency.

Then, a simple Gr-Si junction is put under examination, resulting in something more complex than a Schottky diode. The fabrication of a Gr-Si junction often leads to a parallel structure which can affect the device's output characteristic. The results of this study have been published and are reported in reference [4].

Moreover, a CNT-Si based heterostructure is analysed. Exploiting the previous results, this device is investigated to be used for several applications, from bias tuneable photodetector to Boolean logic device. This study has been published and it is reported in reference [5].

Finally, in the very last part of this chapter, a brief exposure of some results obtained from the collaboration with the RWTH Aachen University and AMO, where I spent 6 months (Oct2021-April2022) learning fabrication processes. Here I present some optical images of self-fabricated TMD FETs and a MoS_2/WSe_2 heterostructure, including some standard electrical characterization.

3.1. Photogeneration

According to the well-known wave-particle duality principle, light waves could be treated as particles, which are referred to as photons. The energy of a photon is $E = h\nu$ where h is Plank's constant and ν is the frequency. Photons can interact with a semiconductor in several ways; they can interact with the lattice, with the impurity atoms or with the defects. Anyway, interaction with valence electrons is the most interesting basic interaction process. In this interaction, indeed,

colliding photons can impart enough energy to let valence electrons jumping into the conduction band. This process generates electron-hole pairs and creates excess carrier concentrations.

Not all the photons can be absorbed in the semiconductor (**Figure 3.1**). The absorption depends on the incident photon energy E and on the semiconductor energy bandgap E_g. If the photon energy is less than E_g, the photons cannot be absorbed and the light is transmitted through the material, hence the semiconductor appears to be transparent. If the photon energy is greater than E_g, instead, it can be absorbed and can interact with a valence electron, elevating it into the conduction band. This process has high probability, as valence band contains many electrons, and the conduction band is consisted of many empty states. This interaction results in an electron – hole pair generation: for each generated electron in the conduction band, there is a hole left into the valence band. Any eventual excess energy may give the electron or hole additional kinetic energy, which will be dissipated as heat in the semiconductor.
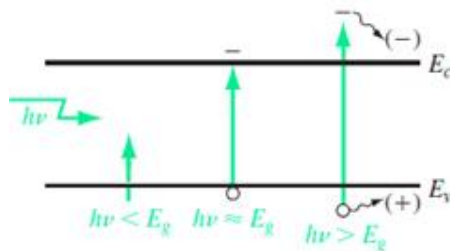
Figure 3.1 – *Photons can be absorbed if they have enough energy to jump into the conduction band.*

When excess electrons and holes are generated in a semiconductor, there is an increase in the conductivity of the material. Besides, if electrons and holes are generated within the space charge region of a pn junction, they can be separated by an applied electric field resulting in a current flow. This change in conductivity can be exploited to detect the presence of photons. Such a device is known as photodetector, i.e., a device that convert optical signals into electrical signals.

Although pn junction is the basis of several photodetector devices such as photodiodes and phototransistors, Schottky diodes have higher current drive capability and, depending on the SBH, several order of magnitude larger I_0. This makes of Schottky diodes the preferred rectifying devices when applications require high current at low voltage. Another greatest advantage of using Schottky diodes in photodetection is that they avoid limitations related to minority carrier recombination time, as they don't involve at all minority carriers. For this reason, high-speed Schottky photodiodes are found in optical communications or optical measurements. Moreover, Schottky junctions are also used as low-cost photovoltaic cells, converting light into current (or voltage) at zero voltage (or current) bias.

3.2. Schottky diodes for photodetection

Photodetectors convert light in an electric signal. The reader can look at some examples of Schottky photodetectors in **Figure 3.2**.
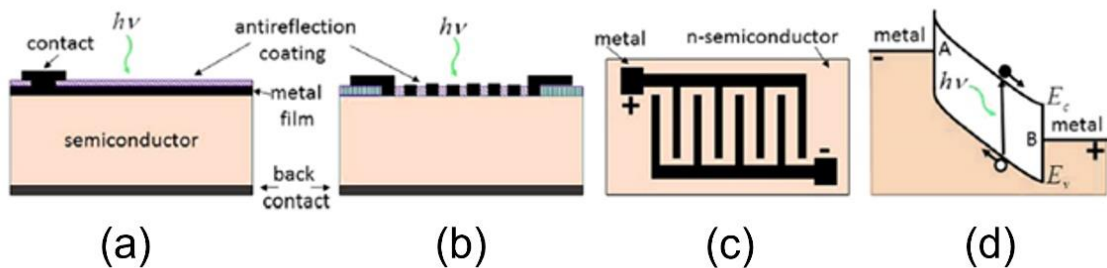
Figure 3.2 – Different layout of Schottky photodiodes, with (a) a semi-transparent thin film or (b) with a metal grid. (c) Interdigital electrode structure is used to improve the device performance and applying a sufficient large voltage (d) all the carriers photogenerated in the semiconductor will contribute to the photocurrent.

They are essentially fabricated depositing a metal layer on top of a semiconductor wafer. Then, to increase the sensitivity of the device, it is a common practice to put on top of the semiconductor a semi-transparent thin film (10 nm or less) (**Figure 3.2(a)**) or a metal grid (**Figure 3.2(b)**) and an

antireflection coating to reduce light loss in the metal. In this context, transparent electrodes, such as graphene, should be used to have a rectifying junction.

Another way to improve the device performance is to use a pair of Schottky photodiodes together, built in a so-called interdigital electrode structure on the same semiconductor **Figure 3.2(c)**. Here, we have two electrodes of opposite bias sign. If we consider a n-type substrate, a reverse biased junction forms at the negative electrode, while the other electrode forms a forward biased junction (respectively A and B in **Figure 3.2(d)**). In this way, the leakage current is suppressed by the presence of a blocking junction. Moreover, you can apply a sufficient large voltage to widen the two depletion layers, making reach themselves, achieving the reach-through configuration. In this way, all the electron-hole pairs photogenerated in the semiconductor region between the two electrodes will contribute to the photocurrent.

Schottky photodetectors are negative biased, whereby the diode dark current is low and the extra current due to light is more distinguishable. Photodetectors can operate with two different mechanisms, depending on the radiation energy $h\nu$. One comes from photons with energy lower than E_g (but higher than the semiconductor work function), which excite the electrons from the metal, injecting them into the semiconductor (**Figure 3.3(a)**). The other mechanism is instead showed in **Figure 3.3(b)**: if photons have energy greater than E_g, they can generate electron-hole pairs into the depletion layer in the semiconductor, increasing carriers and thus conductivity, contributing to the photocurrent.
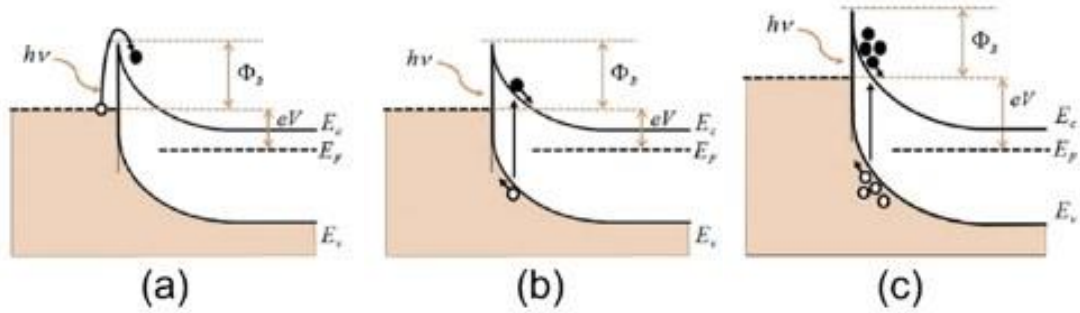
Figure 3.3 – (a) *Photons with energy less than E_g excite metal electrons injecting them into the semiconductor.* **(b)** *Photons with energy greater than E_g can generate hole-electron pairs in the semiconductor depletion layer.* **(c)** *Avalanche mode operation.*

Thanks to the first mechanism, if the Schottky barrier height is small enough, suppressing the reverse leakage current operating at cryogenic temperatures (below 77K), photodetectors can detect long infrared radiation (IR). The second mechanism, on the other hand, enable high speed detection since the time response of the Schottky diode is only limited by the carrier flow across the depletion region and by the RC time constant of the circuit.

Figure 3.3(c) shows a device operated in avalanche mode, reached at very high negative voltage, close to the semiconductor breakdown voltage. This operating mode gives high internal gain and both high-speed and sensitivity to low intensity light.

3.2.1. Figures of merit

The basic metric of a photodetector is the external quantum efficiency EQE (sometimes referred to as incident photon conversion efficiency IPCE), defined as the number of carriers produced per photon,

$$EQE = \frac{I_{ph}/e}{\Phi_{in}} = \frac{I_{ph}}{e}\frac{hv}{P_{in}}$$

(3.1)

In **Equation(3.1)** $I_{ph} = I_{light} - I_{dark}$ is the photocurrent, $\Phi_{in} = P_{in}/hv$ is the incoming photon flux and P_{in} is the incident optical power. The ideal quantum efficiency is unity. This value can be affected by current loss due to recombination, incomplete absorption, reflection, etc. The

internal quantum efficiency IQE, instead, is calculated in a similar way, substituting the incoming photon flux with the absorbed photon flux ($\Phi_{abs} = \Phi_{in}A_{abs}$, with A_{abs} the absorbed fraction):

$$IQE = \frac{I_{ph}/e}{\Phi_{abs}} \qquad (3.2)$$

Related to EQE is the responsivity, R_I, which is the photocurrent divided by the incident optical power:

$$R_I = \frac{I_{ph}}{P_{in}} = EQE \cdot \frac{e}{h\nu} \left(\frac{A}{W}\right) \qquad (3.3)$$

In many applications, measuring a photovoltage is preferred rather than a photocurrent. Indeed, measuring a voltage can have the advantage of eliminating the power consumption associated to Joule-heating. In such case, the responsivity R_V (photovoltage responsivity) is defined as photovoltage V_{ph} divided by the incident optical power:

$$R_V = \frac{V_{ph}}{P_{in}} \left(\frac{V}{W}\right) \qquad (3.4)$$

Other figures of merit related to photodetectors concern the noise. The noise, which should be kept as low as possible, determines the minimum detectable signal. Usually there are many factors which contribute to the total noise (dark current, thermal noise, shot noise, flicker noise, etc.). The noise-equivalent power (NEP) is the relevant figure of merit in this context. It corresponds to the incident RMS optical power required to produce a signal-to-noise ratio of 1 in a 1Hz bandwidth. The NEP is expressed in units of $WHz^{-0.5}$ and represents the minimum detectable power. If

$$S_I = \sqrt{\overline{I_{noise}^2}/1Hz} \qquad (3.5)$$

is the RMS dark noise density ($\overline{I_{noise}^2}$ is the average of the square of the current noise I_{noise} measured with 0.5 s integration time, which corresponds to a bandwidth of 1 Hz (Nyquist criterion)) then

$$NEP = S_I/R_I \qquad\qquad (3.6)$$

with R_I is the photocurrent responsivity of **Equation(3.3)**. A similar definition of NEP can be given for the photovoltage responsivity:

$$NEP = S_V/R_V \qquad\qquad (3.7)$$

With $S_V = \sqrt{\bar{V}^2_{noise}/1Hz}$ the analogous of S_I for the voltage noise V_{noise}. Finally, the detectivity D^* (measured in Jones – named after R.C. Jones) is defined as

$$D^* = \frac{\sqrt{AB}}{NEP}\left(cm\frac{\sqrt{Hz}}{W} \equiv Jones\right) \qquad\qquad (3.8)$$

where A is the area of the photosensitive region and B is the frequency bandwidth of the photodetector. The detectivity encloses simultaneously the information of detector sensitivity, spectral response and noise.

3.2.2. Graphene-Silicon Schottky Diode

Silicon has been holding a dominant position in the microelectronics field for decades, leading the development of the semiconductor technology. However, silicon has some limitations as an optoelectronic material for photodetection. Indeed, it has short bandwidth and a large surface reflectivity, making it not a great choice as near-infrared (NIR) photodetector. As NIR photodetection is crucial for a variety of applications, from optical communication[171–173] (1550nm) to remote sensing[174–176] , there is the need to find a silicon-based device with broader bandwidth and high responsivity.

Graphene is very attractive for advanced optoelectronic applications due to its chemical stability, zero bandgap, high conductivity, flexibility, low noise, and other extraordinary properties[177–180]. Indeed, thanks to its semimetal behavior and tunable energy Fermi level, it can enable new features in traditional electronic and optoelectronic devices[21,181]. For instance, graphene can be

put on silicon forming a Schottky photodiode[181–184]. Hence, graphene can replace the metal contact of a Schottky junction and make shallow junctions with excellent photodetection properties[185,186]. The Gr-Si junction is therefore a basic element for novel electronic devices, identifying graphene as the favorite candidate that can improve the existing semiconductor technology[187–189].

Gr-Si junctions are usually fabricated on a Si substrate covered by an SiO_2 dielectric layer. An etched window in the SiO_2 cap layer opens a Si area for the formation of the Gr-Si junction. In fact, graphene is transferred on top, covering the bare Si area. Besides, graphene also encroaches upon the oxide layer for the formation of contacts with metal leads. Such an encroachment of graphene over SiO_2 results in a Gr-SiO_2-Si structure in parallel with the Gr-Si junction. This heterostructure is actually a Metal-Insulator-Semiconductor (MIS) structure. It has been shown in literature that the MIS structure affects the current-voltage (IV) and capacitance-voltage characteristics of the junction[190] and enhances its photodetection performance[113,191,192]. The MIS capacitor plays a significant role in improving the optical and electronic properties of Gr-Si photodiodes, as reported in recent studies[191,193–195].Therefore, to really understand the physics behind Gr-Si junction, it is essential to study the MIS structure and how it can affect the device performance in the detail.

For this reason, we have transferred graphene monolayers, produced by chemical vapor deposition (CVD), onto a n-Si wafer covered by a patterned silicon nitride (Si_3N_4) layer that replaces the traditional SiO_2 dielectric. Si_3N_4 films, indeed, are excellent diffusion barriers (for metal, water, oxygen, etc.) and allows us to enhance the MIS capacitance by increasing the dielectric constant. For the same reason, we also made the insulator just thick 15 nm. In such a way, we have formed a Gr-Si junction in parallel with Gr-Si_3N_4-Si MIS structures. This special layout leads to the observation of an unreported feature, namely a "kink", in the reverse-bias current-voltage characteristics. Characterizing such device, we also demonstrate that the MIS structure is a

booster for the photo response as it becomes the reservoir of photogenerated holes that contribute to the photocurrent in reverse bias. Indeed, photogenerated holes, accumulated at the Si₃N₄-Si interface, tunnel through the Si₃N₄ by FN mechanism, increasing the photocurrent and enhancing the responsivity of the device.

3.2.2.1. Fabrication details and device layout

Samples were fabricated on doped n-Si (100) wafers with resistivity of ~10 Wcm, corresponding to a phosphorus dopant density of $\sim 4.5 \times 10^{14} \; cm^{-3}$. A $15 \; nm$ thick Si₃N₄ was deposited by CVD. Then, a $3x3 \; mm^2$ squared window was patterned by lithography and wet etching of the silicon nitride. The window was further cleaned by hydrofluoric acid immediately before the Gr deposition to prevent or limit the formation of native silicon oxide.

Graphene sheets of about $5 \times 7 \; mm^2$ area have been transferred onto the Si substrates by a wet method to cover the Si trench while extending over the surrounding Si₃N₄ layer, thus acting both as the anode of the Gr-Si junction and as the top electrode of the Gr-Si₃N₄-Si MIS structure. Contacts to graphene were realized by Ag paste of about 1 mm diameter. It has been verified, indeed, that Ag paste on graphene gives low-resistance ohmic contacts[74]. In the same way, Ag paste was also spread on the scratched backside of the Si-substrate to guarantee an ohmic back contact.

A device schematic is reported in **Figure 3.4(a)**. The Raman spectrum (**Figure 3.4(b)**) provides a clear evidence of a high-quality monolayer Gr layer, confirmed by the high 2D/G intensity peak ratio and the negligible defect-related D-peak ($\sim 1350 \; cm^{-1}$).
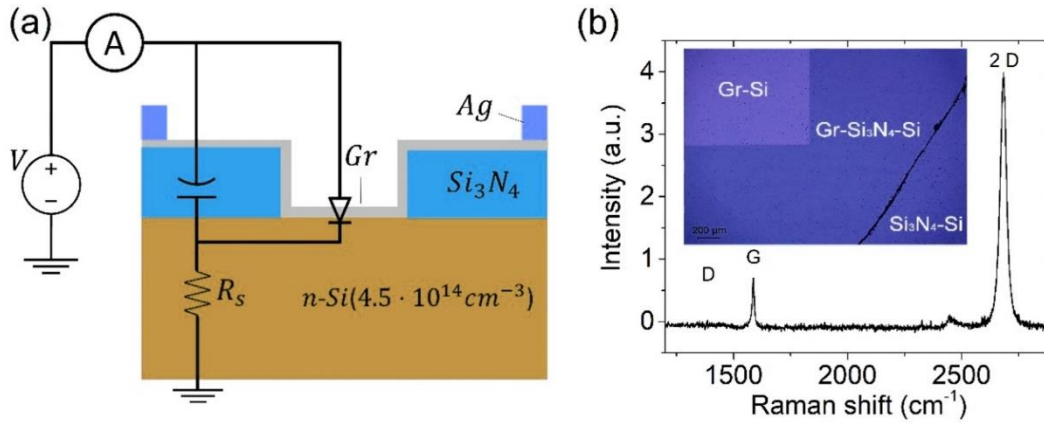
Figure 3.4 – (a) *Device layout.* **(b)** *Raman spectroscopy and optical image in the inset.*

3.2.2.2. Evaluation of Schottky diodes parameters

There are many ways to evaluate Schottky diodes parameters, such as ideality factor (n), Schottky barrier height (SBH, φ_{b0}), Richardson' s constant (A^*). Among all the techniques, the Cheung's method distinguish itself for ease and accuracy.

Figure 3.5(a) shows the semi-logarithmic plot of the current-voltage characteristic of the Gr-Si device in dark at $300\ K$ and atmospheric pressure.

As displayed, the device shows a rectifying behavior (with rectification ratio $\sim 10^4$ at $V = \pm 2.5\ V$) and a diode-like shape that suggests using the ideal diode equation for fitting the current flow:

$$I = I_0 \left[\exp\left(\frac{qV}{nkT}\right) - 1 \right]$$

$$(3.9)$$

where I_0 is the reverse saturation current, q is the electron charge, n the ideality factor, k the Boltzmann constant and T the temperature. The ideality factor in **Equation(3.9)** includes deviations from pure thermoelectric transport ($n = 1$) which can take place in a Schottky diode. Indeed, in Schottky diodes, high ideality factor can occur due to the presence of defects or unwanted insulating layers which can cause Schottky barrier inhomogeneities[196–198].

However, a more realistic model includes a series resistance R_s. We then follow Cheung's method[199] for evaluating the diode parameters. According to Cheung's method, **Equation(3.9)** with a series resistance becomes:

$$I = I_0 \left[\exp \left(\frac{q(V - R_s I)}{nkT} \right) - 1 \right]$$

(3.10)

which, for $V - R_s I \gg nkT/q$, provides:

$$\frac{dV}{dlnI} = R_s I + \frac{nkT}{q}$$

(3.11)

From the fit of **Equation(3.11)**, we can evaluate R_s and n, which can be used to estimate φ_{b0}, defining the following function:

$$H(I) = V - \frac{nkT}{q} \ln \left(\frac{I}{SA^* T^2} \right) = R_s I + \frac{n}{q} \varphi_{b0}$$

(5)

Figure 3.5(b) shows the plots of $\frac{dV}{dlnI}$ and $H(I)$ a function of I from which we extract the following parameters: $n = 2.8$, $R_s = 85 \; k\Omega$ and $\varphi_{b0} = 0.87 \; eV$.

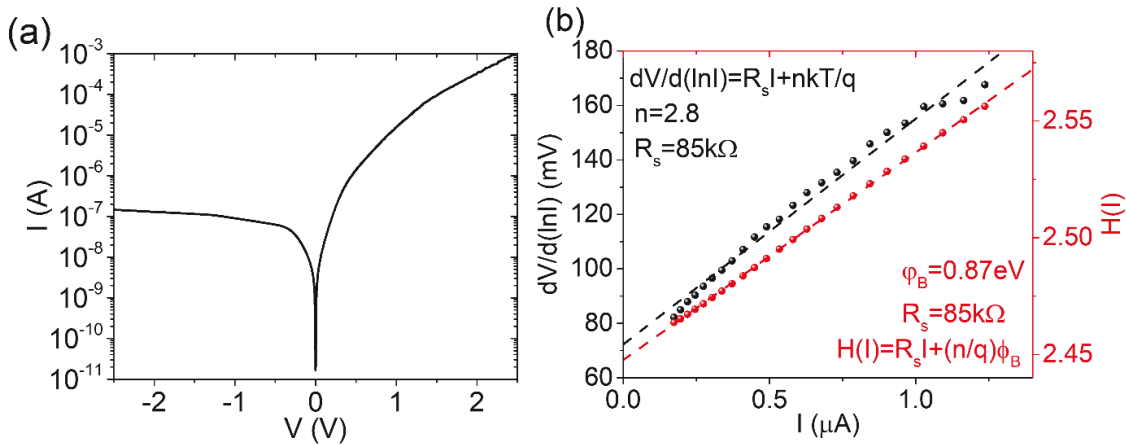*Figure 3.5 (a) Measured IV characteristic of the device in dark (b) Cheung's method plots for evaluation of Schottky barrier height, ideality factor and series resistance.*

Figure 3.6(a-b) display the I-V characteristics of the Gr-Si device at different temperatures, from $T = 400 \; K$ to $T = 220 \; K$, in dark and under illumination by a supercontinuum laser with $3 \; mm$

diameter spot (incident power $1\ mW/cm^2$, wavelenght $\lambda = 500\ nm$), respectively. As predicted by the thermionic theory (**Equation(3.9)** and **Equation(3.10)**), the curves show that lowering the temperature suppresses both the forward and the reverse currents.

Signals of photocurrent only appear in reverse bias and at temperatures below $320\ K$. Moreover, at low temperatures, the I-V curves present sudden curvature changes (one or more kinks) in reverse bias, probably caused by the parallel MIS capacitor, as explained next.

Figure 3.6(c) shows the rectification ratio at $V = \pm 2.5\ V$. In dark, the rectification ratio increases with the decreasing temperature, indicating that, when the temperature is lowered, the Schottky barrier becomes more efficient in suppressing the electron flow from graphene to silicon (reverse current). The rectification ratio under illumination overlaps that measured in dark for temperatures higher than $320\ K$, because there, thermal generation overcomes photogeneration. Below $320\ K$, instead, the rectification ratio decreases with the decreasing temperature, because the reverse current becomes highly dominated by the photogeneration. This result indicates that the photodetection is favourable when the device is negative biased at low temperature. Indeed, at low temperature, the reverse current is substantially enhanced by the electron-hole photogeneration.

From the Cheung's method, we obtained value of n, R_s, and φ_{b0} as function of the temperature, respectively reported in **Figure 3.6(d-e-f)**, in dark (black dot-lines) and under light (red dot-lines). The temperature dependence of the ideality factor in **Figure 3.6(d)** shows a descending behaviour for increasing temperature. This feature indicates that deviations from the ideal thermionic behaviour of the diode are more effective at lower temperatures when thermionic emission is suppressed, and tunneling and diffusion might become comparatively relevant. The dependence on the temperature of the series resistance showed in **Figure 3.6(e)** is typical of a semiconductor and is probably dominated by the silicon substrate.
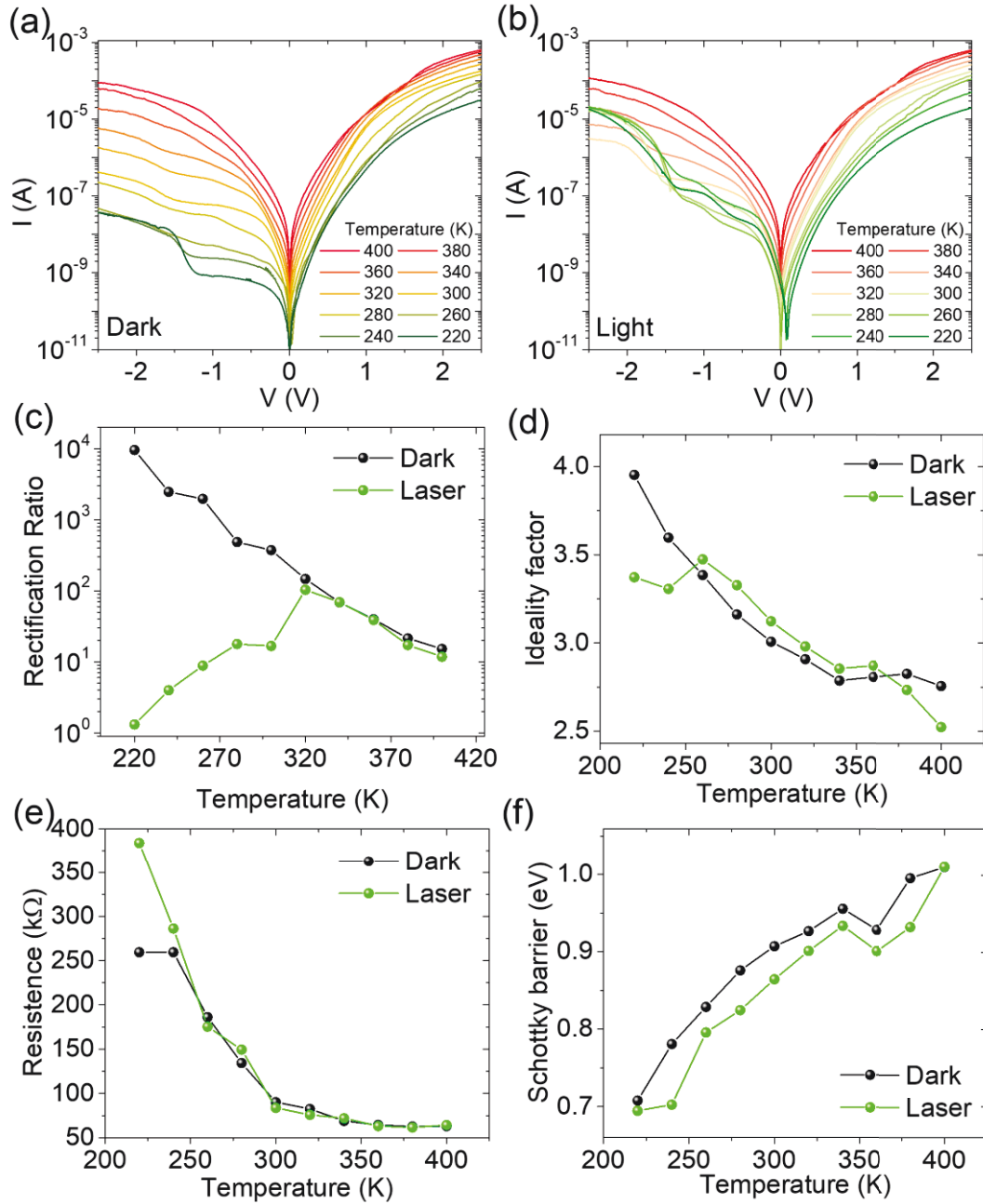
Figure 3.6 - *IV characteristics versus the temperature ranging from 400 K to 220 K in **(a)** dark and **(b)** light. **(c)** Rectification ratio at V=±2.5 V, **(d)** ideality factor, **(e)** series resistance, **(f)** Schottky barrier height versus temperature, evaluated using the Cheung's method.*

Finally, **Figure 3.6(f)** shows that the SBH growths with the increasing temperature. This is a well-known effect when there is barrier inhomogeneity[200–202]. Indeed, at low temperature, the reduced thermal energy makes carrier cross the barrier mainly in the position where the SBH is lower, thus resulting in a reduced SBH. The obtained zero bias SBH, $\varphi_{b0} = 0.87\ eV$, is consistent with some previous works[203,204].

3.2.2.3. Optical Response

Figure 3.7(a) shows the IV characteristics in dark and under illumination by a supercontinuum white laser. The emission power of the laser was tuned from 0 to $180\ mW$, which, considering a light loss factor of 85% in our measurement setup over all the spectral range, corresponds to $0 - 240\ mW/cm^2$ intensity on the device. The obtained normalized photoresponse of the device, defined as $(I_{light} - I_{dark})/I_{dark}$ at $V = -2.5\ V$, is plotted in **Figure 3.7(b)** in function of the laser power and the laser intensity. The data follow an exponential law with the e-folding factor $x_0 = 56\ mW$, which ensures that a maximum light effect is reached above $\sim 170\ mW$. Accordingly, the laser has been set to the maximum power of $180\ mW$ for further tests of the Gr-Si device in photodetection. Particularly, the device has been tested for operating in both photocurrent and photovoltage mode. Setting the voltage to $V = -2.5\ V$, we performed a series of measurements exposing it to the laser beam with wavelength emission of $\lambda = 1000\ nm$, as representative of near-IR light above the silicon bandgap. In **Figure 3.7(c)** the device photocurrent is reported: the photo signal is fast and repeatable. Furthermore, at zero current, we also observed a photovoltaic effect, as reported in **Figure 3.7(d)**. A photovoltage signal appears around 12 mV in response to the incident laser pulse. Possible thermal effects can be neglected, due to the low incident power ($950\ \mu W/cm^2$).
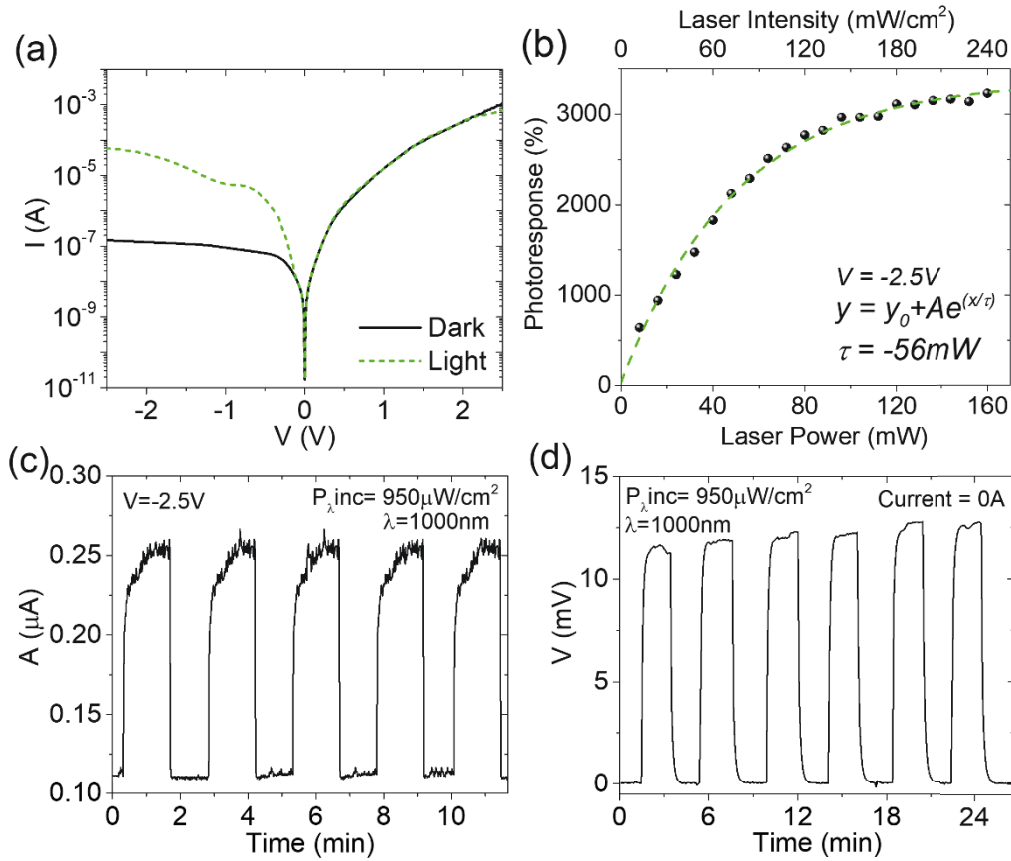
Figure 3.7 – *(a) IV characteristics in dark and with incident white laser. (b) Normalized photoresponse as a function of the laser emitted power and the laser intensity incident on the device. (c) Photodetector operating in photocurrent mode at $V = -2.5\,V$ and (d) photovoltage mode at $I = 0\,A$ under laser beam with $1000\,nm$ wavelength and $950\,\mu W/cm^2$ laser intensity on the device.*

To complete the optoelectronic characterization of the device, the standard photodetector figures

of merit have been investigated over the wavelength range of 500-2000 nm range by sampling

the spectrum of the supercontinuum laser in intervals of 50 nm and 20 nm bandwidth. **Figure**

3.8(a) reports the responsivity of the device along with EQE (see **Equation(3.3)**). It shows an EQE

around 75% for $\lambda < 1100\,nm$, i.e., when photoconversion occurs mainly in Si, followed by a

sudden drop to 0.03% when the energy of the incident light is below the bandgap of Si. For $\lambda >$

1100 nm, indeed, photoexcitation occurs mainly in graphene, as reported in literature[179,205,206],

lowering responsivity and EQE. The obtained results about external quantum efficiency and

responsivity are consistent with the highest reported in the literature over the investigated

spectral range[207–213]. Moreover, **Figure 3.8(b)** shows the $NEP = \frac{\sqrt{2qI_{dark}}}{R}$ (see **Equation(3.6)**). Obviously, the higher EQE corresponds to lower detection power.

With the aim of investigate on the photodetection properties of the device over the already mentioned wavelength range, IV characteristics measurements under light at different wavelengths have been performed (**Figure 3.8(c)** and **Figure 3.8(d)**). Surprisingly, a kink forms at about $V = -1.2\ V$ in the reverse curves.
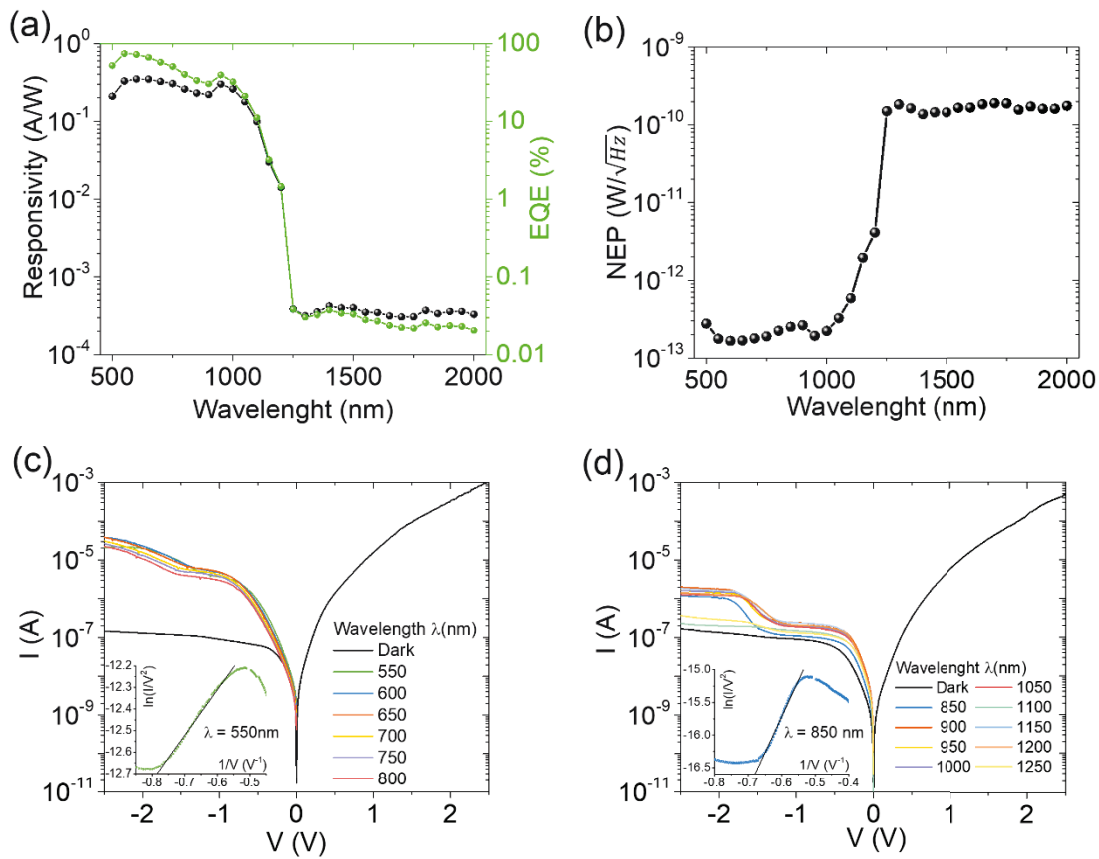
Figure 3.8 - ***(a)*** *Responsivity and EQE of the device in the visible and IR spectral region.* ***(b)*** *NEP and* ***(c)*** *IV characteristics in dark and under light at different wavelengths in the* ***(c)*** *visible and* ***(d)*** *near spectral IR regions. Insets of* ***(c)*** *and* ***(d)*** *show Fowler-Nordheim plots of the reverse IV characteristic at 550 nm and 850 nm, respectively.*

3.2.2.4. How the parallel MIS junction works

The observed kink and the entire optoelectronic behavior of the Gr-Si device can be understood by considering the parallel Gr-Si₃N₄-n-Si structure, which in forward behaves like a MIS capacitor charged by electrons on the Si side. They easily diffuse to the Gr-n-Si junction and contribute to

the forward current. In reverse bias, instead, the negative voltage attracts holes at the Si-Si$_3$N$_4$ interface. As the holes accumulate, the Si undergoes an inversion and becomes p-type. When the voltage is high enough, tunneling through the insulator enables, and a p-type Schottky diode is formed in the MIS region. This means that, in reverse bias, the device behaves as two parallel and opposite diodes: a reverse Schottky diode due to the Gr-Si junction and a forward MIS diode formed by the Gr-Si$_3$N$_4$-p-Si structure.

This parallel configuration explains the kinks at about $V = -1.2\,V$. Indeed, for $-1.2\,V < V < 0\,V$, the holes accumulated at the interface Si-Si$_3$N$_4$ can only diffuse towards the Gr-Si junction, contributing to its reverse current (**Figure 3.9(a)**) and originating the current of $\sim 10^{-7}\,A$. For $V < -1.2\,V$, FN tunneling[124,214] through the Si$_3$N$_4$ layer is enabled by the high electric field (**Figure 3.9(b)**), resulting in an increase of current, which generates the aforementioned kink. Besides, due to the thermal and/or photo generation limited rate in Si, the current reaches a current plateau at high reverse voltage. The insets in **Figure 3.9(a-b)** show the FN analysis of the reverse IV characteristics, confirming the tunneling mechanism. Indeed, the linear behaviour of the FN plot over the range $-0.8\,V^{-1} < V^{-1} < -0.5\,V^{-1}$ (corresponding to -2.0 V to -1.25 V) demonstrates that FN tunneling starts around the kink voltage.
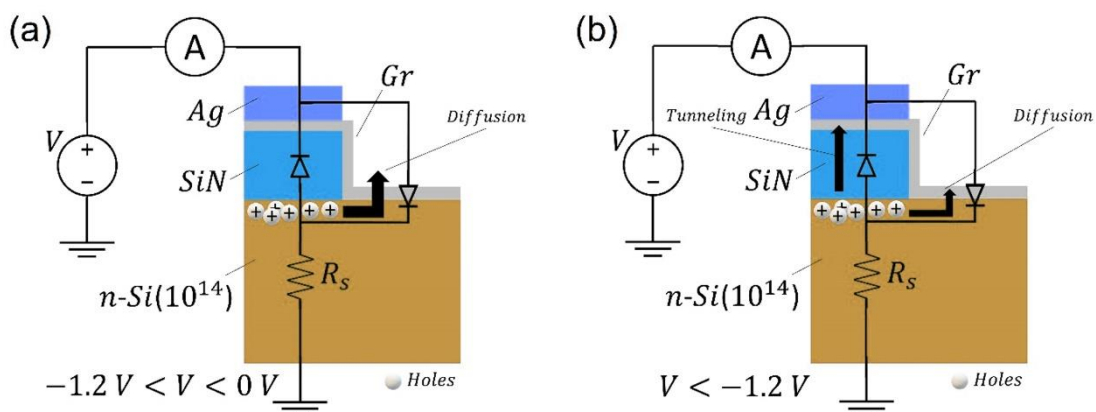

Figure 3.9 - *Schematic model of the Gr-Si device and charge carrier transport in reverse bias, for (a) $-1.2\,V < V < 0\,V$ and (b) $V < -1.2\,V$.*

3.2.3. CNT-Si photodetector with tuneable photocurrent

Carbon nanotubes have a high electrical conductivity. For this reason, CNT based photodetectors have a high dark current. However, combining CNTs with semiconductors (like Silicon) can suppress the dark current, enhancing photodetector's sensitivity[215–220]. Usually, CNTs-Si heterostructures are made including an insulating intra-layer; it eliminates the pinning of the Fermi level, improving the optoelectronic properties of the device[4,221,222]. Hence, it affects the current voltage characteristics of any metal-semiconductor structure and enhances its photodetection properties[193,195,223–226]. For instance, Jia et al. showed that the formation of an oxide layer at the interface of a CNT/Si heterostructure switches charge transport from thermionic emission to a mixture of thermionic emission and tunneling and improves the overall diode properties[227]. Filatzikioti et al. fabricated a hybrid multi-walled CNT/Si3N4/n-Si photodetector with adequate responsivity in the UV and visible part of the spectrum and promising for the IR region due to the CNT bandgap[228].

Moreover, CNT/Si device can be used also in heterogeneous logic circuits[229], such as Boolean optoelectronic circuits. Y.L. Kim et al. proposed a logic device based on a single walled CNT/Si heterojunction photodiode, in which the optical and electrical inputs can control the output current[230].

In the following sections, a CNT-Si device with a special layout is analysed. Single-walled CNTs are used to realize a CNT/Si_3N_4/Si capacitor with enhanced capacitance due to the high dielectric constant of Si_3N_4. The CNT/Si_3N_4/Si capacitor is in parallel to a pre-existing Pt-Ti/Si_3N_4/Si structure. The device behaves like the Gr-Si junction showed in previous paragraph. Indeed, it shows a kink in the reverse-bias IV characteristics of the device. In such a way, when used as a photodetector, the device is endowed with extended functionalities compared to traditional photodiodes. In fact, the

device shows a different photoresponse when light is focussed on the CNT/Si$_3$N$_4$/Si capacitor or around the Pt-Ti/Si$_3$N$_4$/Si region. Furthermore, reverse biasing with different voltages, the device changes its output, suggesting it can be used for several applications, from voltage tuneable photodetection to Boolean logic.

Finally, the device can work as photodetector in self-powered mode, as light generates a photocurrent at zero voltage and a photovoltage at zero current.

3.2.3.1. Fabrication details and device layout

A film of single-wall CNTs has been deposited on a Si$_3$N$_4$/Si substrate endowed with Pt-Ti/Si$_3$N$_4$/Si MIS structures using a dry transfer process[231]. The substrate consists of an n-doped silicon wafer (300 μm thickness, 2300–3150 Ωcm resistivity) with the top surface covered by a 60 nm Si$_3$N$_4$ insulating layer. The CNT film is patterned in a T-shape (see **Figure 3.10(a)**), and the two preexisting top Pt-Ti pads contact it directly. **Figure 3.10** shows a 3D schematic view and a cross-section of the device.

The Pt-Ti/Si$_3$N$_4$/Si and CNT/Si$_3$N$_4$/Si heterostructures, after that the Si$_3$N$_4$ underneath the Pt-Ti pad had been broken by electrical stress, can be modelled as a MIS diode in parallel to a MIS capacitor, with a resistance in series (see **Figure 3.10(b)**). Indeed, the repeated electrical stress between the top Pt-Ti pad and the Si substrate makes the nitride barrier thinner, so that tunneling can occur, letting us model the Pt-Ti/Si3N4/Si structure as a stable MIS diode[102,222,231–234]. To keep a light notation, from now on, we will refer to Pt-Ti/Si$_3$N$_4$/Si structure as the MIS diode and to CNT/Si$_3$N$_4$/Si structure as the MIS capacitor, while the parallel combination of the MIS diode and capacitor will be designated as the CNT-Si device.

The CNT film was obtained by filtering a liquid solution of CNTs through a filter membrane, in low vacuum. The liquid solution was made of CNT powder diluted to 80 μg/mL with distilled water and

sodium dodecyl sulfate (SDS, 2% solution weight ratio), which surrounds the CNTs and prevent their aggregation and precipitation. The mixture was then tip-ultrasonicated for 1 h and left for about 10 h to let the bundled nanotubes precipitate. Then, they are removed until getting a stable mixture without any kind of further CNT precipitation (it requires several months). Once we obtained a stable mixture, it was deposited on a filter membrane (Durapore PVDF, pore size 0.22 µm, diameter 47 mm) using vacuum filtration and rinsed with a solution of ethanol, methanol, and water (15%–15%–70%) to remove all the surfactant from the CNT film.

After the CNT filter was dried, transfer process can start. The transfer is accomplished by placing a piece of CNT film over the substrate, wetting the membrane with water and ethanol, and then pressing it to improve the adhesion of the film to the substrate. After few minutes, the dried membrane was peeled off and the CNT film was left over the substrate.

The electrical measurements were realized in a Janis 500 high vacuum cryogenic probe station connected to a semiconductor parameter analyzer Keithley 4200-SCS. The photoresponse was investigated using a super continuous light source (1 mm^2 spot) with wavelength in the 450-2400 nm range (SuperK compact by NKT photonics) as light source, which was focused either around the Pt-Ti pad or over the CNT film.
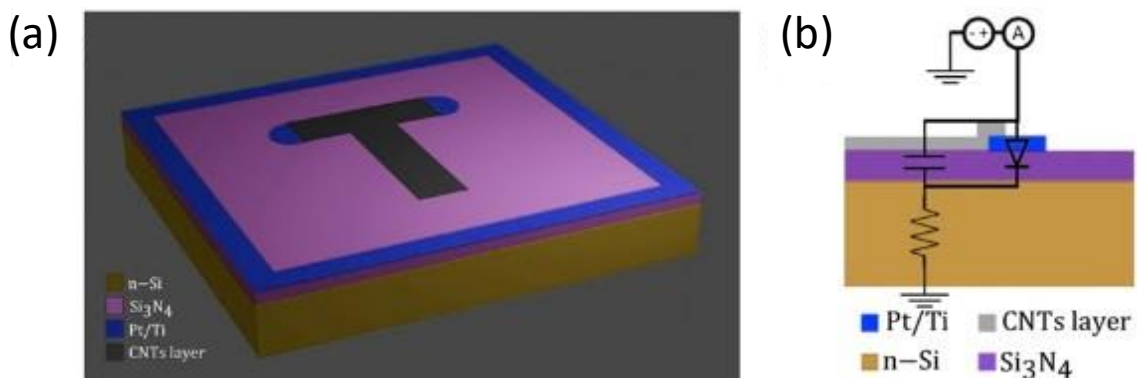

Figure 3.10 - **(a)** 3D schematic view and **(b)** cross-section of the device under study.

The morphology of the film was checked using a field-emission scanning electron microscope (SEM, Zeiss LEO 1530) using an acceleration voltage of 5 kV. As displayed in **Figure 3.11(a),** the film is homogeneous and does not present visible holes. **Figure 3.11(b)** shows the film at higher magnification. It reveals that the nanotubes are randomly oriented and cover completely the substrate.

Then, the film was analyzed with an X-Ray photoelectron spectroscope (PHI 1257, using Al Kα radiation), to get information about its chemical composition, and with micro-Raman (LABRAM, λ=633 nm), to estimate the quality and the nature of the nanotubes. **Figure 3.11(c)** show an XPS survey spectrum acquired on the film. The only observable signals detect the carbon, due to the nanotubes, and oxygen, that can be attributed to atmospheric contaminant above the film. Silicon signals are not observable, indicating once more the high level of coverage of the film. **Figure 3.11(d)** shows the Raman spectra acquired on the film. In the high frequency region, we can observe the D and G band typical of carbon materials, while in the low frequency region are the Radial Breathing Mode (RBM) of the single-walled CNT. The D band, that is due the presence of amorphous carbon and crystallographic defects, is less intense than the G band. This highlights the good quality of the nanotubes used for the film. Thanks to the RBM, we have estimated the diameter (d), the chiral vector index (n,m) and the type of nanotubes ($d_1 = 1.303\ nm$, $(n,m)_1 = (14,4)$, Type = Semiconductor ; $d_2 = 0.908$, $(n,m)_2 = (8,5)$, Type = Metallic).
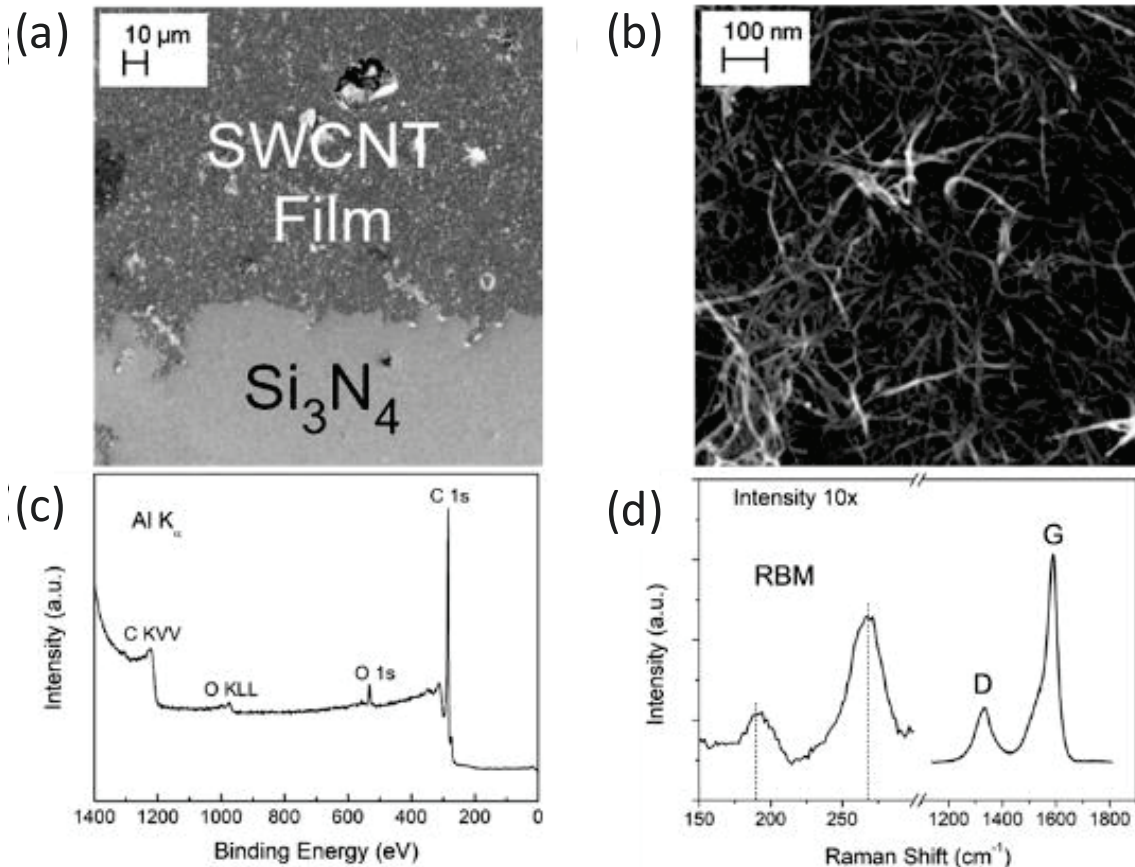
Figure 3.11 - *(a)* *SEM image of the CNT film above the substrate at low magnification.* *(b)* *Single-walled CNT film at high magnification.* *(c)* *XPS survey spectrum and* *(d)* *RAMAN spectrum of the CNT film.*

3.2.3.2. MIS Diode Parameters

To evaluate the MIS diode parameters, we measured the output characteristics at different temperatures (**Figure 3.12(a)**). To understand the role of the CNTs, we also studied a similar device (Ag-Si device), obtained by substituting the CNT layer with an Ag film (**Figure 3.12(b)**). The plots show that for both devices, there is a suppression of both the forward and reverse currents at low temperature, as predicted by the thermionic theory. However, the reverse current of the CNT-Si device shows a step up around V = -7 V at any temperature.

A possible explanation is that the CNTs, due to their aspect ratio, locally enhance the electric field, activating FN tunneling through the Si_3N_4 layer in the CNT-device MIS capacitor[102,125,235]. The FN mechanism activates at any temperature when the reverse voltage is less than -7V (corresponding

to Zone II in **Figure 3.12**). In the Ag-Si device, instead, there is no field amplification and carriers cannot tunnel through the insulator layer.

Figure 3.13(a) shows the rectification (on/off) ratio at V = ± 4 V for both devices as a function of the temperature. The On/Off ratio decrease with rising the temperature. Indeed, the reverse current increases at higher temperatures because of the increasing of thermal generation. Also, CNTs film also enhances the diode performance, as demonstrated by the higher on/off ratio of the CNT-Si device over the Ag-Si device. The I-V curves at different temperatures can be used to extract the SBH, ideality factor, and series resistance following the already described Cheung's method[199](**Figure 3.13(b-c-d)**).
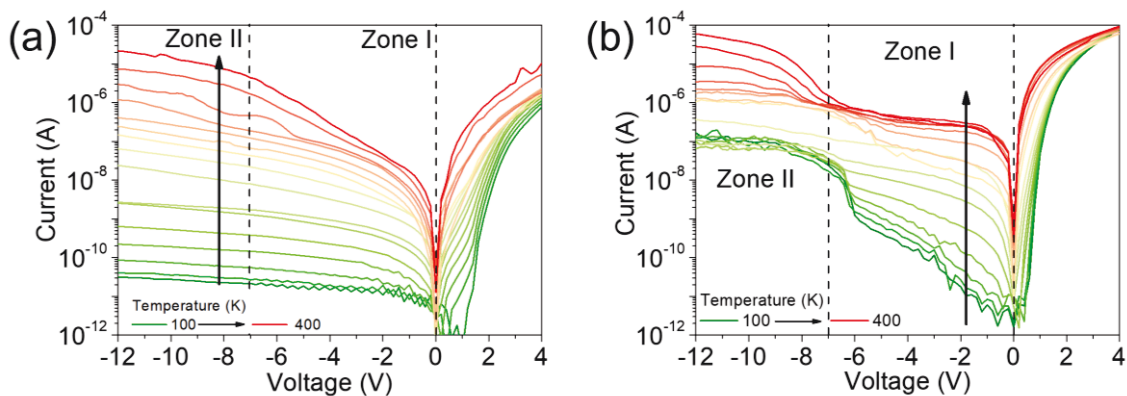
Figure 3.12 - *IV characteristics at different temperatures for the (a) Ag-Si device and the (b) CNT-Si device.*

Figure 3.13(b) shows that the ideality factor decreases for increasing temperature. Indeed, deviations from the ideal thermionic behavior of the diode occur mainly at lower temperatures when thermionic emission is suppressed, and tunneling or diffusion might become comparatively relevant. **Figure 3.13(c)** shows that the SBH decreases with the decreasing temperature. The obtained barrier (around 0.7 eV at room temperature) is consistent with other works using similar devices[236,237]. The difference in Schottky barrier heights of the CNT-Si device and the Ag-Si device can be easily attributed to the natural device-to-device fluctuations. The temperature behavior,

instead, it is a well-known effect we have already mentioned in the previous paragraph, due to spatial barrier inhomogeneity[200,201,238].

Finally, **Figure 3.13(d)** shows the temperature behavior of the series resistance, which is almost constant over the explored temperature range. The series resistance of the CNT-Si device is lower, highlighting another advantage in the use of the CNTs film.
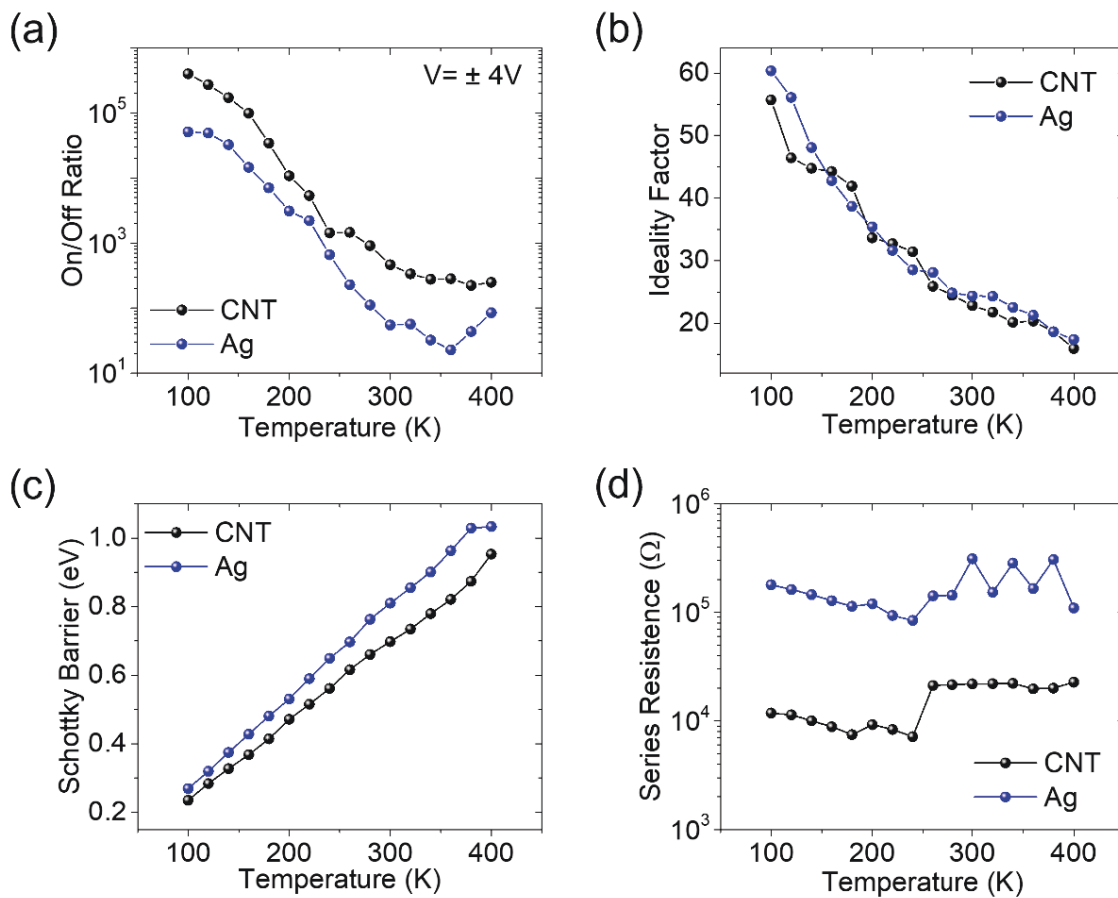
Figure 3.13 - *(a) On/off ratio at V= ± 4V, (b) ideality factor, (c) Schottky barrier height, and (d) series resistance, as a function of the temperature for the CNT-Si device (labelled as CNT, black) and the Ag-Si device (labelled as Ag, blue).*

3.2.3.3. Optical Response

We investigated the photodetection properties of CNT-Si device focusing the light over the MIS capacitor and over the MIS diode, highlighting differences. The device has been illuminated by a supercontinuum white source, with 8 mW/cm2 intensity. The IV characteristics in dark and under

light in different position are shown in **Figure 3.14(a)**. When the light is on the MIS diode, the

photogeneration in the depletion region of the MIS diode appears already at low voltages,

resulting in an already high photocurrent in Zone I. Increasing the negative voltage (Zone II), the

FN tunneling of photogenerated carriers activates in the MIS capacitor, thus showing the already

mentioned current set up. When instead the light is focused on the MIS capacitor,

photogeneration in the depletion region of the MIS diode is lower, and the photogenerated

charges in the area below the MIS capacitor mainly contribute to the total photocurrent.

Moreover, in such case, the total current is lower due to the thicker Si_3N_4 layer. Indeed, the Si_3N_4

layer under the Pt-Ti pad has been previously broken by the electrical stress.

Zone I and Zone II represent voltage ranges with two different output photocurrents. This

behavior allows the photodetector to operate in two different current regimes according to the

requirement of the specific application.

Remarkably, **Figure 3.14(b)**, that shows the photocurrent at different negative biases, confirms

that the photoresponse is faster than the limit of 500 ms set by our measurement setup, no

matter if the light is focused around the Pt-Ti pad or the CNT film.

Figure 3.14(c-d) show the photocurrent maps of the CNT-Si and the Ag-Si devices in Zone II (at $V = -12.5\ V$) and fixed wavelength and incident power ($\lambda = 640\ nm$; $P_\lambda = 1.2\ \mu W$). The CNT film

enhances the photoresponse of the device, extending the photosensitive area to the entire "T",

while the Ag paste shuts out the light under the "T", thus resulting in suppressed photocurrent

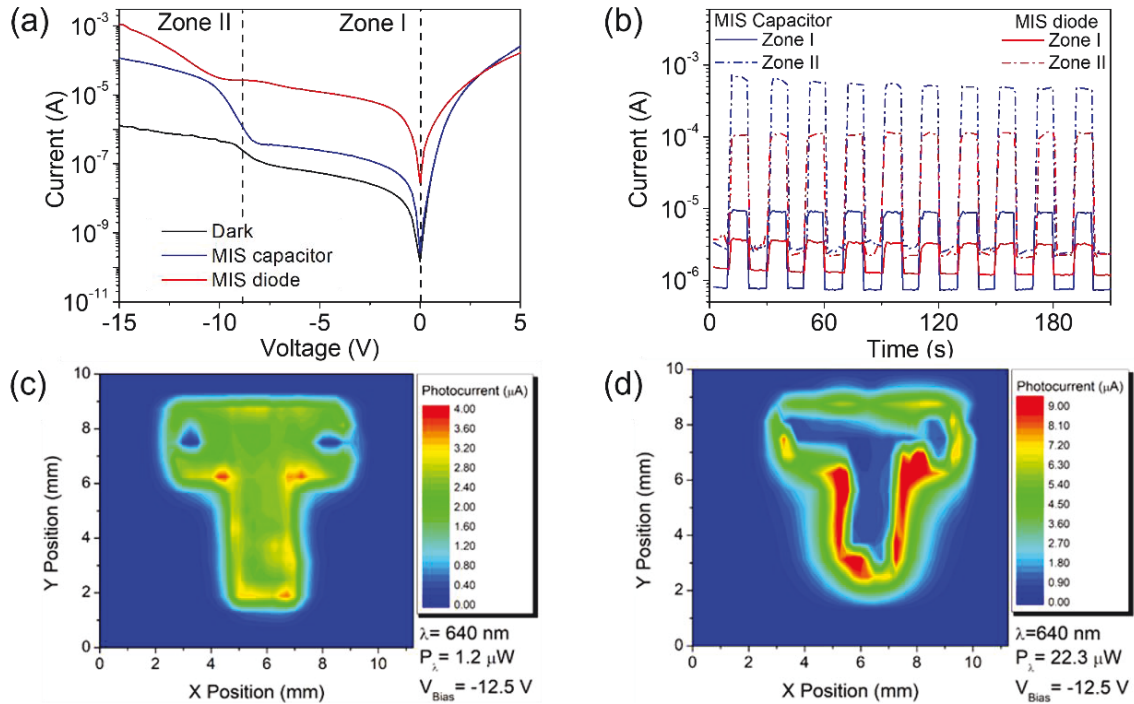(even with increased light incident power, $P_\lambda = 22.3\ \mu W$).

Figure 3.14 - **(a)** CNT-Si device IV characteristics under illumination on the MIS diode (green curve) and the MIS capacitor (red curve). **(b)** Extracted photocurrent at different biases and in different configurations. **(c)** CNT-device and **(d)** Ag-device photocurrent maps.

We completed the optoelectronic characterization of the CNT-Si device, investigating the spectral response in the 500–1100 nm wavelength range by sampling the spectrum of the supercontinuum source in intervals of 50 nm with 20 nm bandwidth and evaluating some figures of merit. **Figure 3.15(a)** reports the responsivity and the EQE of the device biased at V = -14 V (Zone II) and with light focused on the MIS diode. It shows a peak in EQE around 50% for 800 nm < λ< 1100 nm suggesting that photoconversion occurs mainly in Si. The weaker photoresponse for λ < 800 nm can be attributed to the increased electron-hole recombination rate. High energy light is absorbed closer to the Si/Si_3N_4 interface where the high concentration of intragap states and the lower mobility favor the recombination of photogenerated electron-hole pairs.

Moreover, **Figure 3.15(b)** shows the noise equivalent power (NEP). As expected, the higher quantum efficiency corresponds to the lower detection power. The obtained EQE is on the low side of the distribution of values typically reported in the literature.[239,240]

To investigate the photodetection properties in self-powered mode, the CNT-Si device photo response has been tested at zero current and zero voltage bias, focusing the light on the MIS diode. The device reacts to light with fast and repeatable photocurrent and photovoltage. **Figure 3.15(c-d)** show that under illumination, the device generates both a current and a voltage, specifically 40 nA at 0 V and 20 mV at 0 A.
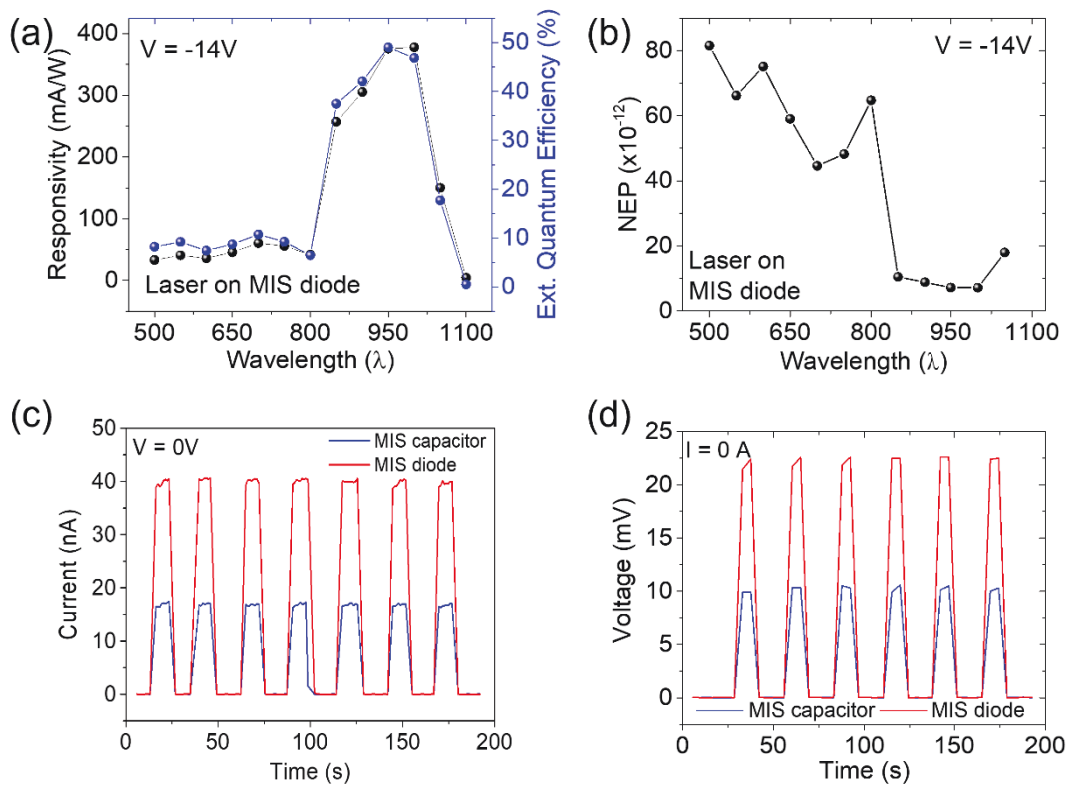
Figure 3.15 - *(a) Responsivity and external quantum efficiency, (b) noise equivalent power, (c) photocurrent at 0 V and (d) photovoltage at 0 A of the CNT-Si device.*

3.2.3.4. Boolean Logic Application

Furthermore, the photocurrent dependence on the voltage bias and the light spot position suggests the use of the device for Boolean logic applications. Indeed, we can associate a binary variable (x) to the applied voltage (for instance, with value "0" for -8V < V < -6V and "1" for -14V < V < -12V), and a second variable (y) to the position of the incident light spot ("0" for light spot over the MIS capacitor, "1" for light spot over the MIS diode). **Figure 3.16** shows that the device can

operate as an exclusive OR (XOR). Indeed, when the photocurrent is in the range 10^{-5} A < I < 10^{-4} A, the output is assumed to be "1", while elsewhere it is considered as a "0". The position of the light spot as a variable for a Boolean device is an original approach in our study.

x (Vbias)	y (Light on)	x ⊕ y
-8V<V<-6V	MIS capacitor	0
-8V<V<-6V	MIS diode	1
-14V<V<-12V	MIS capacitor	1
-14V<V<-12V	MIS diode	0
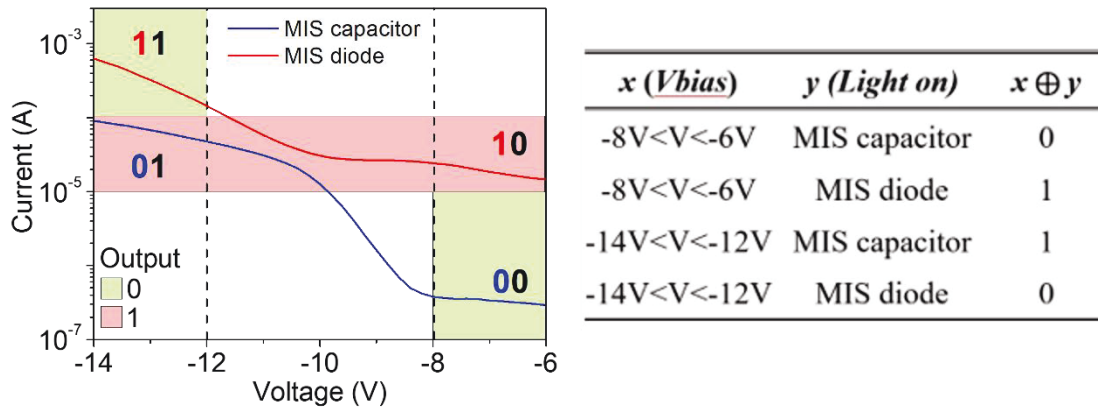
Figure 3.16 - CNT-Si device suitable for optoelectronic Boolean logic application, working as a XOR.

3.3. MoS$_2$/WSe$_2$ heterostructures for photodetection

In the last part of my PhD years, I have spent about 6 months to learn about 2D devices fabrication in Aachen, Germany, at the RWTH University. The aim of this collaboration was to let me have a first approach to 2D material-based devices fabrication, producing some TMD (MoS$_2$ and WSe$_2$) standard FETs and some MoS$_2$/WSe$_2$ heterostructures. In this paragraph, I briefly report the optical images and some standard electrical characterization of the devices I have fabricated by myself. It is important to highlight that, as the reader should have already got an idea looking at this PhD thesis, these chips contain my first and only fabricated devices.

First, I have fabricated several MoS$_2$ and WSe$_2$ FETs. A schematic layout of these devices and some optical images are reported in **Figure 3.17**.
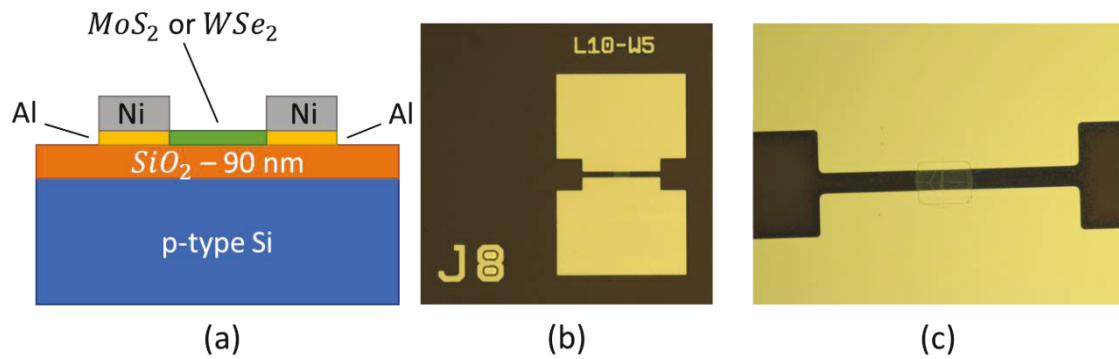
Figure 3.17 – (a) Schematic layout of a standard 2D-based field effect transistor. *(b)* Optical image of one of the several fabricated devices and *(c)* a close picture of the channel.

Figure 3.18 shows the device fabrication process flow. After a substrate (blue box is silicon, orange box is silicon dioxide) cleaning with plasma oxygen, the 2D TMD (green box) is wet transferred onto it. Then, the device is patterned, with a positive lithography process, in order to have a portion of the TMD covered by the photoresist (black box): this part will be our channel. Soon after that, indeed, the rest of uncovered TMD is etched into a Reactive Ion chamber. To made up source and drain of the transistor, a negative lithography process is performed to cover the channel and all the other parts where metal isn't needed. Finally, 12.5 nm of nichel (yellow box) and 100 nm of aluminium (grey box) are deposited onto the chip and the unwanted part get lifted off in acetone.
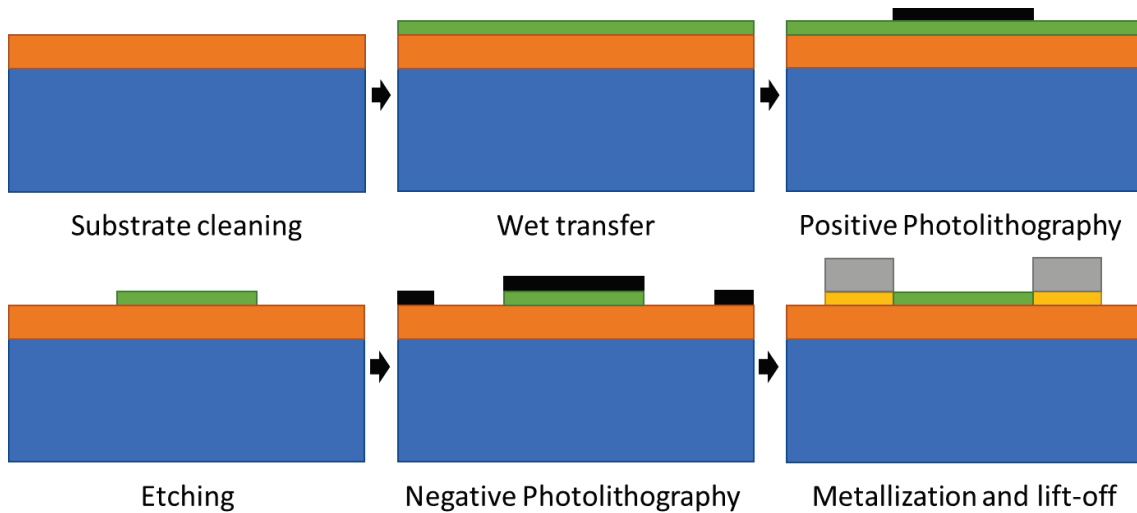
Figure 3.18 – Process flow of a standard 2D FET fabrication.

Below, a standard characterization of a WSe$_2$ FET with channel dimension of $3\mu m \times 50\mu m$ is reported. **Figure 3.19(a)** shows current-voltage characteristics varying the applied gate voltage, suggesting a high current modulation. This is confirmed by the transfer characteristic in **Figure 3.19(b)**, which reports an on/off ratio of almost five orders of magnitude in the range of $V = \pm 40V$.
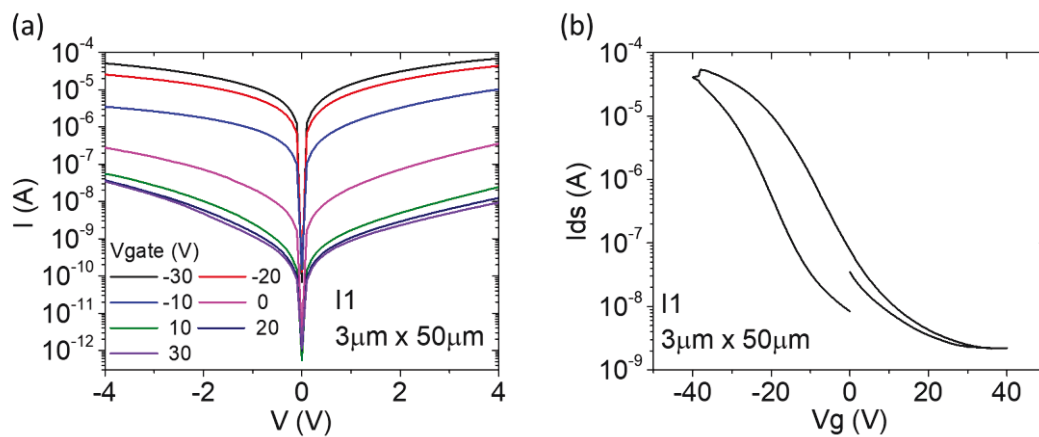
Figure 3.19 – (a) Output characteristics varying the applied gate voltage. *(b)* Transfer characteristic.

Then, MoS$_2$/WSe$_2$ heterostructures have been fabricated. The schematic layout of the fabricated device and some optical images are shown in **Figure 3.20**. After a first deposition of Aluminum/Palladium contacts, 2D materials (synthetized with chemical vapor deposition, CVD)

have been wet transferred on a quartz substrate. Finally, a side Aluminum/Nichel contact has been made. Different metals have been used to contact MoS_2 and WSe_2 to achieve ohmic condition at both sides.

(a)　　　　　　　　(b)　　　　　　　　(c)
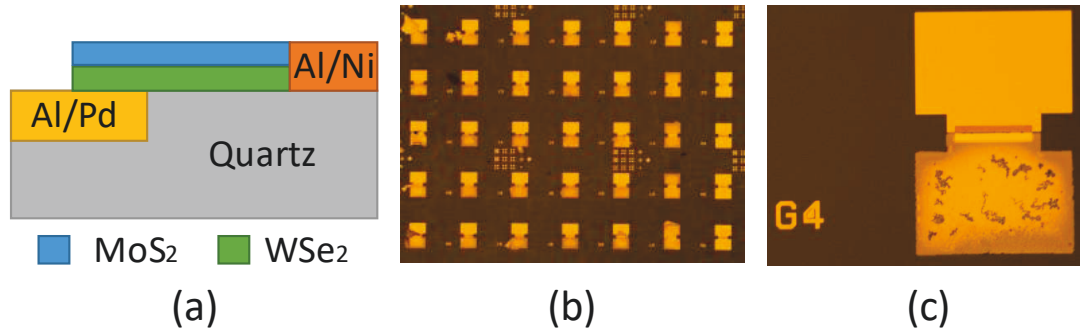
Figure 3.20 – (a) Schematic layout of the TMD lateral heterostructure. (b) Optical image of the entire chip with several devices and (c) of a single device.

The optoelectrical measurements are reported in **Figure 3.21**. The output characteristic displayed in **Figure 3.21(a)** shows that the device responds to light. **Figure 3.21(b-c)** report the photocurrent signals generated by laser irradiations (of 30s and 1 minute respectively) with incident power of 180mW. The device shows a responsivity of about $1\mu A/W$ and a slow response time of several minutes.

(a)　　　　　　　　(b)　　　　　　　　(c)
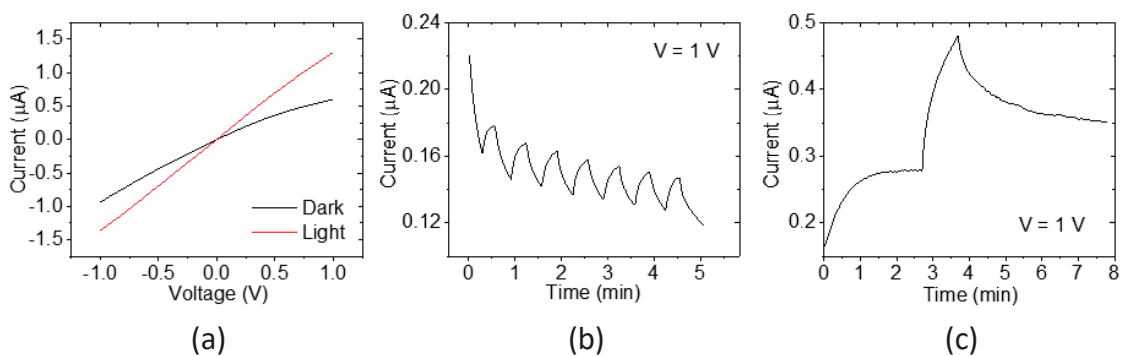
Figure 3.21 – (a) Output characteristic of MoS₂/WSe₂ heterojunction. (b) Measured photocurrent

However, the layout of the device is quite tricky. The charge transport could not flow through both TMDs, and the current can be short circuited into the WSe_2 layer. For this reason, and also to

103

improve the obtained optoelectronic results, a new layout has been taken under consideration (**Figure 3.22**). Collaboration with RWTH University is still in progress and this work will be further improved the next year.
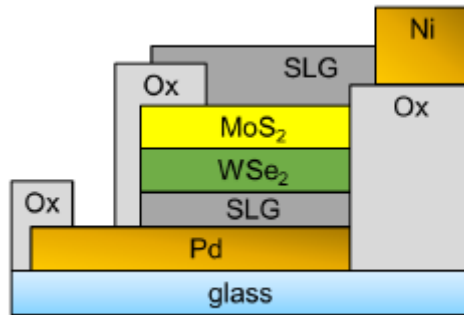
Figure 3.22 – Improved schematic layout. SLG is single layer graphene.

Summary

In Summary, my PhD thesis shows the opto-electronical characterization of low-dimensional materials-based devices. In particular, in the first chapter a wide view of low dimensional electronics basic concepts has been reported, from the materials properties to the standard operation of Schottky diodes, Field Effect Transistors, Heterostructures and Field Emission devices.

Chapter 2 deals with Transition Metal Dichalcogenides FETs and how light, electron beam and applied external field can affect their characteristics. Molybdenum disulphide and Platinum diselenide FETs are investigated. It is demonstrated that electron beam contact irradiation can enhance conductivity, lowering energy barriers at the contacts, and left-shifting the threshold voltage because of the piling up of positive charge at the interface Si/SiO_2[1]. Field emission from a flake of MoS_2 is also reported in Chapter 2. It is demonstrated that field emission current can be modulated by an applied voltage on the gate oxide, paving the way for innovative field emission transistors[2]. Coexistence of negative and positive photoconductivity in Platinum diselenide FETs has been demonstrated. Light focused on the material can favor adsorbate desorption and consequent n-doping and at the same time causes the standard photogeneration process. These two opposite processes dominate at different pressure conditions. At ambient pressure, where density of adsorbate is high, n-doping dominate the photogeneration process, and it results in a decrease of current (negative photocurrent). In high vacuum, instead, almost all the adsorbates have been evacuated, and the photogeneration process dominates, resulting in an increase of current (positive photocurrent)[3].

In Chapter 3 a Graphene-Silicon Schottky diode, a CNT-Silicon Schottky diode and a MoS_2/WSe_2 heterostructure are investigated for photodetection. The fabrication of a Graphene-Silicon Schottky diode often involves the formation of a parallel metal-insulator-semiconductor structure which affects the current voltage characteristic with a kink in the reverse current. This is fully explained by a tunneling process, also supported by a Fowler-Nordheim analysis. The studied device also shows good photodetection properties, like an external quantum efficiency around 75% for $\lambda < 1100 \, nm$[4]. Then,

exploiting the formation of the kink in the reverse current due to a parallel MIS structure, a CNT-Si device has been fabricated to have a MIS diode (Pt-Ti/Si_3N_4/Si) in parallel to a MIS capacitor (CNT/Si_3N_4/Si). This particular layout makes the device suitable for several innovative applications, like a photodetector with tunable bias or a Boolean logic device using the position of light as input variable[5]. Finally, hosted by Prof. Max Lemme at the RWTH University in Aachen, I have learnt how to fabricate standard 2D materials-based FETs and TMDs heterostructures. The last part of this Chapter shows some optical images of the fabricated devices and some optoelectronic characterization to investigate their photodetection properties.

References

(1) Pelella, A.; Kharsah, O.; Grillo, A.; Urban, F.; Passacantando, M.; Giubileo, F.; Iemmo, L.; Sleziona, S.; Pollmann, E.; Madauß, L. Electron Irradiation of Metal Contacts in Monolayer MoS2 Field-Effect Transistors. *ACS Applied Materials & Interfaces* **2020**, *12* (36), 40532–40540.

(2) Pelella, A.; Grillo, A.; Urban, F.; Giubileo, F.; Passacantando, M.; Pollmann, E.; Sleziona, S.; Schleberger, M.; Di Bartolomeo, A. Gate-controlled Field Emission Current from MoS2 Nanosheets. *Advanced Electronic Materials* **2021**, *7* (2), 2000838.

(3) Grillo, A.; Faella, E.; Pelella, A.; Giubileo, F.; Ansari, L.; Gity, F.; Hurley, P. K.; McEvoy, N.; Di Bartolomeo, A. Coexistence of Negative and Positive Photoconductivity in Few-Layer PtSe2 Field-Effect Transistors. *Advanced Functional Materials* **2021**, *31* (43), 2105722. https://doi.org/10.1002/adfm.202105722.

(4) Pelella, A.; Grillo, A.; Faella, E.; Luongo, G.; Askari, M. B.; Di Bartolomeo, A. Graphene–Silicon Device for Visible and Infrared Photodetection. *ACS Appl. Mater. Interfaces* **2021**, acsami.1c12050. https://doi.org/10.1021/acsami.1c12050.

(5) Pelella, A.; Capista, D.; Passacantando, M.; Faella, E.; Grillo, A.; Giubileo, F.; Martucciello, N.; Di Bartolomeo, A. A Self-Powered CNT–Si Photodetector with Tuneable Photocurrent. *Advanced Electronic Materials n/a* (n/a), 2200919. https://doi.org/10.1002/aelm.202200919.

(6) Novoselov, K. S.; Geim, A. K.; Morozov, S. V.; Jiang, D.; Zhang, Y.; Dubonos, S. V.; Grigorieva, I. V.; Firsov, A. A. Electric Field Effect in Atomically Thin Carbon Films. *Science* **2004**, *306* (5696), 666–669. https://doi.org/10.1126/science.1102896.

(7) Novoselov, K. S.; Geim, A. K.; Morozov, S. V.; Jiang, D.; Katsnelson, M. I.; Grigorieva, I. V.; Dubonos, S. V.; Firsov, A. A. Two-Dimensional Gas of Massless Dirac Fermions in Graphene. *Nature* **2005**, *438* (7065), 197–200. https://doi.org/10.1038/nature04233.

(8) Frank, I. W.; Tanenbaum, D. M.; van der Zande, A. M.; McEuen, P. L. Mechanical Properties of Suspended Graphene Sheets. *Journal of Vacuum Science & Technology B: Microelectronics and Nanometer Structures Processing, Measurement, and Phenomena* **2007**, *25* (6), 2558–2561. https://doi.org/10.1116/1.2789446.

(9) Lee, C.; Wei, X.; Kysar, J. W.; Hone, J. Measurement of the Elastic Properties and Intrinsic Strength of Monolayer Graphene. *Science* **2008**, *321* (5887), 385–388. https://doi.org/10.1126/science.1157996.

(10) Wallace, P. R. The Band Theory of Graphite. *Phys. Rev.* **1947**, *71* (9), 622–634. https://doi.org/10.1103/PhysRev.71.622.

(11) Mina, A. N.; Awadallah, A. A.; Phillips, A. H.; Ahmed, R. R. Simulation of the Band Structure of Graphene and Carbon Nanotube. *J. Phys.: Conf. Ser.* **2012**, *343*, 012076. https://doi.org/10.1088/1742-6596/343/1/012076.

(12) Yankowitz, M.; Jung, J.; Laksono, E.; Leconte, N.; Chittari, B. L.; Watanabe, K.; Taniguchi, T.; Adam, S.; Graf, D.; Dean, C. R. Dynamic Band-Structure Tuning of Graphene Moiré Superlattices with Pressure. *Nature* **2018**, *557* (7705), 404–408. https://doi.org/10.1038/s41586-018-0107-1.

(13) Sahu, S.; Rout, G. C. Band Gap Opening in Graphene: A Short Theoretical Study. *Int Nano Lett* **2017**, *7* (2), 81–89. https://doi.org/10.1007/s40089-017-0203-5.

(14) Murali, R.; Yang, Y.; Brenner, K.; Beck, T.; Meindl, J. D. Breakdown Current Density of Graphene Nanoribbons. *Appl. Phys. Lett.* **2009**, *94* (24), 243114. https://doi.org/10.1063/1.3147183.

(15) Balandin, A. A.; Ghosh, S.; Bao, W.; Calizo, I.; Teweldebrhan, D.; Miao, F.; Lau, C. N. Superior Thermal Conductivity of Single-Layer Graphene. *Nano Lett.* **2008**, *8* (3), 902–907. https://doi.org/10.1021/nl0731872.

(16) Los, J. H.; Zakharchenko, K. V.; Katsnelson, M. I.; Fasolino, A. Melting Temperature of Graphene. *Phys. Rev. B* **2015**, *91* (4), 045415. https://doi.org/10.1103/PhysRevB.91.045415.

(17) Su, P.-G.; Chiou, C.-F. Electrical and Humidity-Sensing Properties of Reduced Graphene Oxide Thin Film Fabricated by Layer-by-Layer with Covalent Anchoring on Flexible Substrate. *Sensors and Actuators B: Chemical* **2014**, *200*, 9–18. https://doi.org/10.1016/j.snb.2014.04.035.

(18)   Wehenkel, D. J.; Bointon, T. H.; Booth, T.; Bøggild, P.; Craciun, M. F.; Russo, S. Unforeseen High Temperature and Humidity Stability of FeCl3 Intercalated Few Layer Graphene. *Sci Rep* **2015**, *5* (1), 7609. https://doi.org/10.1038/srep07609.

(19)   Leong, W. S.; Gong, H.; Thong, J. T. L. Low-Contact-Resistance Graphene Devices with Nickel-Etched-Graphene Contacts. *ACS Nano* **2014**, *8* (1), 994–1001. https://doi.org/10.1021/nn405834b.

(20)   Xia, F.; Perebeinos, V.; Lin, Y.; Wu, Y.; Avouris, P. The Origins and Limits of Metal–Graphene Junction Resistance. *Nature Nanotech* **2011**, *6* (3), 179–184. https://doi.org/10.1038/nnano.2011.6.

(21)   Di Bartolomeo, A.; Santandrea, S.; Giubileo, F.; Romeo, F.; Petrosino, M.; Citro, R.; Barbara, P.; Lupina, G.; Schroeder, T.; Rubino, A. Effect of Back-Gate on Contact Resistance and on Channel Conductance in Graphene-Based Field-Effect Transistors. *Diamond and Related Materials* **2013**, *38*, 19–23. https://doi.org/10.1016/j.diamond.2013.06.002.

(22)   Russo, S.; Craciun, M. F.; Yamamoto, M.; Morpurgo, A. F.; Tarucha, S. Contact Resistance in Graphene-Based Devices. *Physica E: Low-dimensional Systems and Nanostructures* **2010**, *42* (4), 677–679. https://doi.org/10.1016/j.physe.2009.11.080.

(23)   Iijima, S. Helical Microtubules of Graphitic Carbon. *Nature* **1991**, *354* (6348), 56–58. https://doi.org/10.1038/354056a0.

(24)   Kroto, H. W.; Heath, J. R.; O'Brien, S. C.; Curl, R. F.; Smalley, R. E. C60: Buckminsterfullerene. *Nature* **1985**, *318* (6042), 162–163. https://doi.org/10.1038/318162a0.

(25)   Iijima, S.; Ichihashi, T. Single-Shell Carbon Nanotubes of 1-Nm Diameter. *Nature* **1993**, *363* (6430), 603–605. https://doi.org/10.1038/363603a0.

(26)   Terrones, M.; Terrones, H.; Dresselhaus, M. S.; Dresselhaus, G.; Charlier, J. C.; Hernández, E. Electronic, Thermal and Mechanical Properties of Carbon Nanotubes. *Philosophical Transactions of the Royal Society of London. Series A: Mathematical, Physical and Engineering Sciences* **2004**, *362* (1823), 2065–2098. https://doi.org/10.1098/rsta.2004.1430.

(27)   Saito, R.; Dresselhaus, G.; Dresselhaus, M. S. *Physical Properties of Carbon Nanotubes*; PUBLISHED BY IMPERIAL COLLEGE PRESS AND DISTRIBUTED BY WORLD SCIENTIFIC PUBLISHING CO., 1998. https://doi.org/10.1142/p080.

(28)   Li, H. J.; Lu, W. G.; Li, J. J.; Bai, X. D.; Gu, C. Z. Multichannel Ballistic Transport in Multiwall Carbon Nanotubes. *Phys. Rev. Lett.* **2005**, *95* (8), 086601. https://doi.org/10.1103/PhysRevLett.95.086601.

(29)   Heer, W. A. de. Nanotubes and the Pursuit of Applications. *MRS Bulletin* **2004**, *29* (4), 281–285. https://doi.org/10.1557/mrs2004.81.

(30)   Kaul, A. B. Two-Dimensional Layered Materials: Structure, Properties, and Prospects for Device Applications. *Journal of Materials Research* **2014**, *29* (3), 348–361. https://doi.org/10.1557/jmr.2014.6.

(31)   Lee, J. Y.; Shin, J.-H.; Lee, G.-H.; Lee, C.-H. Two-Dimensional Semiconductor Optoelectronics Based on van Der Waals Heterostructures. *Nanomaterials* **2016**, *6* (11), 193. https://doi.org/10.3390/nano6110193.

(32)   Manzeli, S.; Ovchinnikov, D.; Pasquier, D.; Yazyev, O. V.; Kis, A. 2D Transition Metal Dichalcogenides. *Nat Rev Mater* **2017**, *2* (8), 1–15. https://doi.org/10.1038/natrevmats.2017.33.

(33)   Cowley, A. M.; Sze, S. M. Surface States and Barrier Height of Metal-Semiconductor Systems. *Journal of Applied Physics* **1965**, *36* (10), 3212–3220. https://doi.org/10.1063/1.1702952.

(34)   Hökelek, E.; Robinson, G. Y. Schottky Contacts on Chemically Etched P- and N-type Indium Phosphide. *Appl. Phys. Lett.* **1982**, *40* (5), 426–428. https://doi.org/10.1063/1.93101.

(35)   Rickert, K. A.; Ellis, A. B.; Kim, J. K.; Lee, J.-L.; Himpsel, F. J.; Dwikusuma, F.; Kuech, T. F. X-Ray Photoemission Determination of the Schottky Barrier Height of Metal Contacts to n–GaN and p–GaN. *Journal of Applied Physics* **2002**, *92* (11), 6671–6678. https://doi.org/10.1063/1.1518129.

(36)   Monch, W. On the Physics of Metal-Semiconductor Interfaces. *Rep. Prog. Phys.* **1990**, *53* (3), 221–278. https://doi.org/10.1088/0034-4885/53/3/001.

(37)   Bardeen, J. Surface States and Rectification at a Metal Semi-Conductor Contact. *Phys. Rev.* **1947**, *71* (10), 717–727. https://doi.org/10.1103/PhysRev.71.717.

(38)   Frisenda, R.; Navarro-Moratalla, E.; Gant, P.; Lara, D. P. D.; Jarillo-Herrero, P.; Gorbachev, R. V.; Castellanos-Gomez, A. Recent Progress in the Assembly of Nanodevices and van Der Waals

Heterostructures by Deterministic Placement of 2D Materials. *Chem. Soc. Rev.* **2018**, *47* (1), 53–68. https://doi.org/10.1039/C7CS00556C.

(39) Wang, H.; Liu, F.; Fu, W.; Fang, Z.; Zhou, W.; Liu, Z. Two-Dimensional Heterostructures: Fabrication, Characterization, and Application. *Nanoscale* **2014**, *6* (21), 12250–12272. https://doi.org/10.1039/C4NR03435J.

(40) Novoselov, K. S.; Mishchenko, A.; Carvalho, A.; Castro Neto, A. H. 2D Materials and van Der Waals Heterostructures. *Science* **2016**, *353* (6298), aac9439. https://doi.org/10.1126/science.aac9439.

(41) Hunt, B.; Sanchez-Yamagishi, J. D.; Young, A. F.; Yankowitz, M.; LeRoy, B. J.; Watanabe, K.; Taniguchi, T.; Moon, P.; Koshino, M.; Jarillo-Herrero, P.; Ashoori, R. C. Massive Dirac Fermions and Hofstadter Butterfly in a van Der Waals Heterostructure. *Science* **2013**, *340* (6139), 1427–1430. https://doi.org/10.1126/science.1237240.

(42) Britnell, L.; Ribeiro, R. M.; Eckmann, A.; Jalil, R.; Belle, B. D.; Mishchenko, A.; Kim, Y.-J.; Gorbachev, R. V.; Georgiou, T.; Morozov, S. V.; Grigorenko, A. N.; Geim, A. K.; Casiraghi, C.; Neto, A. H. C.; Novoselov, K. S. Strong Light-Matter Interactions in Heterostructures of Atomically Thin Films. *Science* **2013**, *340* (6138), 1311–1314. https://doi.org/10.1126/science.1235547.

(43) Geim, A. K.; Grigorieva, I. V. Van Der Waals Heterostructures. *Nature* **2013**, *499* (7459), 419–425. https://doi.org/10.1038/nature12385.

(44) Zhang, W.; Wang, Q.; Chen, Y.; Wang, Z.; Wee, A. T. S. Van Der Waals Stacked 2D Layered Materials for Optoelectronics. *2D Mater.* **2016**, *3* (2), 022001. https://doi.org/10.1088/2053-1583/3/2/022001.

(45) Britnell, L.; Gorbachev, R. V.; Jalil, R.; Belle, B. D.; Schedin, F.; Mishchenko, A.; Georgiou, T.; Katsnelson, M. I.; Eaves, L.; Morozov, S. V.; Peres, N. M. R.; Leist, J.; Geim, A. K.; Novoselov, K. S.; Ponomarenko, L. A. Field-Effect Tunneling Transistor Based on Vertical Graphene Heterostructures. *Science* **2012**, *335* (6071), 947–950. https://doi.org/10.1126/science.1218461.

(46) Georgiou, T.; Jalil, R.; Belle, B. D.; Britnell, L.; Gorbachev, R. V.; Morozov, S. V.; Kim, Y.-J.; Gholinia, A.; Haigh, S. J.; Makarovsky, O.; Eaves, L.; Ponomarenko, L. A.; Geim, A. K.; Novoselov, K. S.; Mishchenko, A. Vertical Field-Effect Transistor Based on Graphene–WS2 Heterostructures for Flexible and Transparent Electronics. *Nature Nanotech* **2013**, *8* (2), 100–103. https://doi.org/10.1038/nnano.2012.224.

(47) Xue, Y.; Zhang, Y.; Liu, Y.; Liu, H.; Song, J.; Sophia, J.; Liu, J.; Xu, Z.; Xu, Q.; Wang, Z.; Zheng, J.; Liu, Y.; Li, S.; Bao, Q. Scalable Production of a Few-Layer MoS2/WS2 Vertical Heterojunction Array and Its Application for Photodetectors. *ACS Nano* **2016**, *10* (1), 573–580. https://doi.org/10.1021/acsnano.5b05596.

(48) Duan, X.; Wang, C.; Shaw, J. C.; Cheng, R.; Chen, Y.; Li, H.; Wu, X.; Tang, Y.; Zhang, Q.; Pan, A.; Jiang, J.; Yu, R.; Huang, Y.; Duan, X. Lateral Epitaxial Growth of Two-Dimensional Layered Semiconductor Heterojunctions. *Nature Nanotech* **2014**, *9* (12), 1024–1030. https://doi.org/10.1038/nnano.2014.222.

(49) Chen, X.; Qiu, Y.; Yang, H.; Liu, G.; Zheng, W.; Feng, W.; Cao, W.; Hu, W.; Hu, P. In-Plane Mosaic Potential Growth of Large-Area 2D Layered Semiconductors MoS2–MoSe2 Lateral Heterostructures and Photodetector Application. *ACS Appl. Mater. Interfaces* **2017**, *9* (2), 1684–1691. https://doi.org/10.1021/acsami.6b13379.

(50) Li, M.-Y.; Pu, J.; Huang, J.-K.; Miyauchi, Y.; Matsuda, K.; Takenobu, T.; Li, L.-J. Self-Aligned and Scalable Growth of Monolayer WSe2–MoS2 Lateral Heterojunctions. *Advanced Functional Materials* **2018**, *28* (17), 1706860. https://doi.org/10.1002/adfm.201706860.

(51) Urban, F.; Lupina, G.; Grillo, A.; Martucciello, N.; Di Bartolomeo, A. Contact Resistance and Mobility in Back-Gate Graphene Transistors. *Nano Express* **2020**, *1* (1), 010001. https://doi.org/10.1088/2632-959X/ab7055.

(52) Bolotin, K. I. Electronic Transport in Graphene: Towards High Mobility. In *Graphene*; Elsevier, 2014; pp 199–227. https://doi.org/10.1533/9780857099334.3.199.

(53) Wilmart, Q.; Boukhicha, M.; Graef, H.; Mele, D.; Palomo, J.; Rosticher, M.; Taniguchi, T.; Watanabe, K.; Bouchiat, V.; Baudin, E.; Berroir, J.-M.; Bocquillon, E.; Fève, G.; Pallecchi, E.; Plaçais, B. High-

Frequency Limits of Graphene Field-Effect Transistors with Velocity Saturation. *Applied Sciences* **2020**, *10* (2), 446. https://doi.org/10.3390/app10020446.

(54) Piccinini, E.; Alberti, S.; Longo, G. S.; Berninger, T.; Breu, J.; Dostalek, J.; Azzaroni, O.; Knoll, W. Pushing the Boundaries of Interfacial Sensitivity in Graphene FET Sensors: Polyelectrolyte Multilayers Strongly Increase the Debye Screening Length. *J. Phys. Chem. C* **2018**, *122* (18), 10181–10188. https://doi.org/10.1021/acs.jpcc.7b11128.

(55) Di Bartolomeo, A.; Giubileo, F.; Iemmo, L.; Romeo, F.; Russo, S.; Unal, S.; Passacantando, M.; Grossi, V.; Cucolo, A. M. Leakage and Field Emission in Side-Gate Graphene Field Effect Transistors. *Appl. Phys. Lett.* **2016**, *109* (2), 023510. https://doi.org/10.1063/1.4958618.

(56) Bartolomeo, A. D.; Giubileo, F.; Romeo, F.; Sabatino, P.; Carapella, G.; Iemmo, L.; Schroeder, T.; Lupina, G. Graphene Field Effect Transistors with Niobium Contacts and Asymmetric Transfer Characteristics. *Nanotechnology* **2015**, *26* (47), 475202. https://doi.org/10.1088/0957-4484/26/47/475202.

(57) Li, F.; Gao, F.; Xu, M.; Liu, X.; Zhang, X.; Wu, H.; Qi, J. Tuning Transport and Photoelectric Performance of Monolayer MoS_2 Device by E-Beam Irradiation. *Adv. Mater. Interfaces* **2018**, *5* (14), 1800348. https://doi.org/10.1002/admi.201800348.

(58) Wang, J.; Yao, Q.; Huang, C.-W.; Zou, X.; Liao, L.; Chen, S.; Fan, Z.; Zhang, K.; Wu, W.; Xiao, X.; Jiang, C.; Wu, W.-W. High Mobility MoS_2 Transistor with Low Schottky Barrier Contact by Using Atomic Thick h-BN as a Tunneling Layer. *Adv. Mater.* **2016**, *28* (37), 8302–8308. https://doi.org/10.1002/adma.201602757.

(59) Fiori, G.; Bonaccorso, F.; Iannaccone, G.; Palacios, T.; Neumaier, D.; Seabaugh, A.; Banerjee, S. K.; Colombo, L. Electronics Based on Two-Dimensional Materials. *Nature Nanotech* **2014**, *9* (10), 768–779. https://doi.org/10.1038/nnano.2014.207.

(60) Kim, M. J.; Choi, Y.; Seok, J.; Lee, S.; Kim, Y. J.; Lee, J. Y.; Cho, J. H. Defect-Free Copolymer Gate Dielectrics for Gating MoS_2 Transistors. *J. Phys. Chem. C* **2018**, *122* (23), 12193–12199. https://doi.org/10.1021/acs.jpcc.8b03092.

(61) Rasmussen, F. A.; Thygesen, K. S. Computational 2D Materials Database: Electronic Structure of Transition-Metal Dichalcogenides and Oxides. *J. Phys. Chem. C* **2015**, *119* (23), 13169–13183. https://doi.org/10.1021/acs.jpcc.5b02950.

(62) Di Bartolomeo, A.; Pelella, A.; Liu, X.; Miao, F.; Passacantando, M.; Giubileo, F.; Grillo, A.; Iemmo, L.; Urban, F.; Liang, S. Pressure-Tunable Ambipolar Conduction and Hysteresis in Thin Palladium Diselenide Field Effect Transistors. *Adv. Funct. Mater.* **2019**, *29* (29), 1902483. https://doi.org/10.1002/adfm.201902483.

(63) Di Bartolomeo, A.; Luongo, G.; Iemmo, L.; Urban, F.; Giubileo, F. Graphene–Silicon Schottky Diodes for Photodetection. *IEEE Trans. Nanotechnology* **2018**, *17* (6), 1133–1137. https://doi.org/10.1109/TNANO.2018.2853798.

(64) Jin, C.; Rasmussen, F. A.; Thygesen, K. S. Tuning the Schottky Barrier at the Graphene/MoS_2 Interface by Electron Doping: Density Functional Theory and Many-Body Calculations. *J. Phys. Chem. C* **2015**, *119* (34), 19928–19933. https://doi.org/10.1021/acs.jpcc.5b05580.

(65) Grillo, A.; Di Bartolomeo, A.; Urban, F.; Passacantando, M.; Caridad, J. M.; Sun, J.; Camilli, L. Observation of 2D Conduction in Ultrathin Germanium Arsenide Field-Effect Transistors. *ACS Appl. Mater. Interfaces* **2020**, acsami.0c00348. https://doi.org/10.1021/acsami.0c00348.

(66) Madauß, L.; Zegkinoglou, I.; Vázquez Muiños, H.; Choi, Y.-W.; Kunze, S.; Zhao, M.-Q.; Naylor, C. H.; Ernst, P.; Pollmann, E.; Ochedowski, O.; Lebius, H.; Benyagoub, A.; Ban-d'Etat, B.; Johnson, A. T. C.; Djurabekova, F.; Roldan Cuenya, B.; Schleberger, M. Highly Active Single-Layer MoS_2 Catalysts Synthesized by Swift Heavy Ion Irradiation. *Nanoscale* **2018**, *10* (48), 22908–22916. https://doi.org/10.1039/C8NR04696D.

(67) Schleberger, M.; Kotakoski, J. 2D Material Science: Defect Engineering by Particle Irradiation. *Materials* **2018**, *11* (10), 1885. https://doi.org/10.3390/ma11101885.

(68) Giubileo, F.; Iemmo, L.; Passacantando, M.; Urban, F.; Luongo, G.; Sun, L.; Amato, G.; Enrico, E.; Di Bartolomeo, A. Effect of Electron Irradiation on the Transport and Field Emission Properties of Few-

Layer MoS $_2$ Field-Effect Transistors. *J. Phys. Chem. C* **2019**, *123* (2), 1454–1461. https://doi.org/10.1021/acs.jpcc.8b09089.

(69)   Di Bartolomeo, A.; Urban, F.; Pelella, A.; Grillo, A.; Passacantando, M.; Liu, X.; Giubileo, F. Electron Irradiation of Multilayer PdSe$_2$ Field Effect Transistors. *Nanotechnology* **2020**, *31* (37), 375204. https://doi.org/10.1088/1361-6528/ab9472.

(70)   Ochedowski, O.; Marinov, K.; Wilbs, G.; Keller, G.; Scheuschner, N.; Severin, D.; Bender, M.; Maultzsch, J.; Tegude, F. J.; Schleberger, M. Radiation Hardness of Graphene and MoS $_2$ Field Effect Devices against Swift Heavy Ion Irradiation. *Journal of Applied Physics* **2013**, *113* (21), 214306. https://doi.org/10.1063/1.4808460.

(71)   Ernst, P.; Kozubek, R.; Madauß, L.; Sonntag, J.; Lorke, A.; Schleberger, M. Irradiation of Graphene Field Effect Transistors with Highly Charged Ions. *Nuclear Instruments and Methods in Physics Research Section B: Beam Interactions with Materials and Atoms* **2016**, *382*, 71–75. https://doi.org/10.1016/j.nimb.2016.03.043.

(72)   Madauß, L.; Ochedowski, O.; Lebius, H.; Ban-d'Etat, B.; Naylor, C. H.; Johnson, A. T. C.; Kotakoski, J.; Schleberger, M. Defect Engineering of Single- and Few-Layer MoS $_2$ by Swift Heavy Ion Irradiation. *2D Mater.* **2016**, *4* (1), 015034. https://doi.org/10.1088/2053-1583/4/1/015034.

(73)   Kozubek, R.; Tripathi, M.; Ghorbani-Asl, M.; Kretschmer, S.; Madauß, L.; Pollmann, E.; O'Brien, M.; McEvoy, N.; Ludacka, U.; Susi, T.; Duesberg, G. S.; Wilhelm, R. A.; Krasheninnikov, A. V.; Kotakoski, J.; Schleberger, M. Perforating Freestanding Molybdenum Disulfide Monolayers with Highly Charged Ions. *J. Phys. Chem. Lett.* **2019**, *10* (5), 904–910. https://doi.org/10.1021/acs.jpclett.8b03666.

(74)   Giubileo, F.; Di Bartolomeo, A. The Role of Contact Resistance in Graphene Field-Effect Devices. *Progress in Surface Science* **2017**, *92* (3), 143–175. https://doi.org/10.1016/j.progsurf.2017.05.002.

(75)   Shahzad, K.; Jia, K.; Zhao, C.; Wang, D.; Usman, M.; Luo, J. Effects of Different Ion Irradiation on the Contact Resistance of Pd/Graphene Contacts. *Materials* **2019**, *12* (23), 3928. https://doi.org/10.3390/ma12233928.

(76)   Yan, X.; Jia, K.; Su, Y.; Ma, Y.; Luo, J.; Zhu, H.; Wei, Y. Edge-Contact Formed by Oxygen Plasma and Rapid Thermal Annealing to Improve Metal-Graphene Contact Resistance. *ECS J. Solid State Sci. Technol.* **2018**, *7* (2), M11–M15. https://doi.org/10.1149/2.0251802jss.

(77)   Choi, B. Y.; Cho, K.; Pak, J.; Kim, T.-Y.; Kim, J.-K.; Shin, J.; Seo, J.; Chung, S.; Lee, T. Effects of Electron Beam Irradiation and Thiol Molecule Treatment on the Properties of MoS2 Field Effect Transistors. *J. Korean Phys. Soc.* **2018**, *72* (10), 1203–1208. https://doi.org/10.3938/jkps.72.1203.

(78)   Zhou, W.; Zou, X.; Najmaei, S.; Liu, Z.; Shi, Y.; Kong, J.; Lou, J.; Ajayan, P. M.; Yakobson, B. I.; Idrobo, J.-C. Intrinsic Structural Defects in Monolayer Molybdenum Disulfide. *Nano Lett.* **2013**, *13* (6), 2615–2622. https://doi.org/10.1021/nl4007479.

(79)   Durand, C.; Zhang, X.; Fowlkes, J.; Najmaei, S.; Lou, J.; Li, A.-P. Defect-Mediated Transport and Electronic Irradiation Effect in Individual Domains of CVD-Grown Monolayer MoS $_2$. *Journal of Vacuum Science & Technology B, Nanotechnology and Microelectronics: Materials, Processing, Measurement, and Phenomena* **2015**, *33* (2), 02B110. https://doi.org/10.1116/1.4906331.

(80)   Rice, C.; Young, R. J.; Zan, R.; Bangert, U.; Wolverson, D.; Georgiou, T.; Jalil, R.; Novoselov, K. S. Raman-Scattering Measurements and First-Principles Calculations of Strain-Induced Phonon Shifts in Monolayer MoS 2. *Phys. Rev. B* **2013**, *87* (8), 081307. https://doi.org/10.1103/PhysRevB.87.081307.

(81)   Chakraborty, B.; Bera, A.; Muthu, D. V. S.; Bhowmick, S.; Waghmare, U. V.; Sood, A. K. Symmetry-Dependent Phonon Renormalization in Monolayer MoS 2 Transistor. *Phys. Rev. B* **2012**, *85* (16), 161403. https://doi.org/10.1103/PhysRevB.85.161403.

(82)   Scheuschner, N.; Ochedowski, O.; Kaulitz, A.-M.; Gillen, R.; Schleberger, M.; Maultzsch, J. Photoluminescence of Freestanding Single- and Few-Layer MoS 2. *Phys. Rev. B* **2014**, *89* (12), 125406. https://doi.org/10.1103/PhysRevB.89.125406.

(83)   Conley, H. J.; Wang, B.; Ziegler, J. I.; Haglund, R. F.; Pantelides, S. T.; Bolotin, K. I. Bandgap Engineering of Strained Monolayer and Bilayer MoS $_2$. *Nano Lett.* **2013**, *13* (8), 3626–3630. https://doi.org/10.1021/nl4014748.

(84)   Mak, K. F.; He, K.; Lee, C.; Lee, G. H.; Hone, J.; Heinz, T. F.; Shan, J. Tightly Bound Trions in Monolayer MoS2. *Nature Mater* **2013**, *12* (3), 207–211. https://doi.org/10.1038/nmat3505.

(85)   Pollmann, E.; Madauß, L.; Schumacher, S.; Kumar, U.; Heuvel, F.; Ende, C. vom; Yilmaz, S.; Güngörmüs, S.; Schleberger, M. Apparent Differences between Single Layer Molybdenum Disulphide Fabricated via Chemical Vapour Deposition and Exfoliation. *Nanotechnology* **2020**, *31* (50), 505604. https://doi.org/10.1088/1361-6528/abb5d2.

(86)   Di Bartolomeo, A.; Grillo, A.; Urban, F.; Iemmo, L.; Giubileo, F.; Luongo, G.; Amato, G.; Croin, L.; Sun, L.; Liang, S.-J.; Ang, L. K. Asymmetric Schottky Contacts in Bilayer MoS2 Field Effect Transistors. *Advanced Functional Materials* **2018**, *28* (28), 1800657. https://doi.org/10.1002/adfm.201800657.

(87)   Di Bartolomeo, A.; Urban, F.; Passacantando, M.; McEvoy, N.; Peters, L.; Iemmo, L.; Luongo, G.; Romeo, F.; Giubileo, F. A WSe2 Vertical Field Emission Transistor. *Nanoscale* **2019**, *11* (4), 1538–1548. https://doi.org/10.1039/C8NR09068H.

(88)   Smyth, C. M.; Addou, R.; McDonnell, S.; Hinkle, C. L.; Wallace, R. M. Contact Metal–MoS$_2$ Interfacial Reactions and Potential Implications on MoS$_2$-Based Device Performance. *J. Phys. Chem. C* **2016**, *120* (27), 14719–14729. https://doi.org/10.1021/acs.jpcc.6b04473.

(89)   English, C. D.; Shine, G.; Dorgan, V. E.; Saraswat, K. C.; Pop, E. Improved Contacts to MoS$_2$ Transistors by Ultra-High Vacuum Metal Deposition. *Nano Lett.* **2016**, *16* (6), 3824–3830. https://doi.org/10.1021/acs.nanolett.6b01309.

(90)   Wang, Q.; Deng, B.; Shi, X. A New Insight for Ohmic Contacts to MoS$_2$: By Tuning MoS$_2$ Affinity Energies but Not Metal Work-Functions. *Phys. Chem. Chem. Phys.* **2017**, *19* (38), 26151–26157. https://doi.org/10.1039/C7CP05109C.

(91)   Kim, C.; Moon, I.; Lee, D.; Choi, M. S.; Ahmed, F.; Nam, S.; Cho, Y.; Shin, H.-J.; Park, S.; Yoo, W. J. Fermi Level Pinning at Electrical Metal Contacts of Monolayer Molybdenum Dichalcogenides. *ACS Nano* **2017**, *11* (2), 1588–1596. https://doi.org/10.1021/acsnano.6b07159.

(92)   Guo, Y.; Liu, D.; Robertson, J. 3D Behavior of Schottky Barriers of 2D Transition-Metal Dichalcogenides. *ACS Appl. Mater. Interfaces* **2015**, *7* (46), 25709–25715. https://doi.org/10.1021/acsami.5b06897.

(93)   Pan, Y.; Gu, J.; Tang, H.; Zhang, X.; Li, J.; Shi, B.; Yang, J.; Zhang, H.; Yan, J.; Liu, S.; Hu, H.; Wu, M.; Lu, J. Reexamination of the Schottky Barrier Heights in Monolayer MoS$_2$ Field-Effect Transistors. *ACS Appl. Nano Mater.* **2019**, *2* (8), 4717–4726. https://doi.org/10.1021/acsanm.9b00200.

(94)   Gong, C.; Colombo, L.; Wallace, R. M.; Cho, K. The Unusual Mechanism of Partial Fermi Level Pinning at Metal–MoS$_2$ Interfaces. *Nano Lett.* **2014**, *14* (4), 1714–1720. https://doi.org/10.1021/nl403465v.

(95)   Zhong, H.; Quhe, R.; Wang, Y.; Ni, Z.; Ye, M.; Song, Z.; Pan, Y.; Yang, J.; Yang, L.; Lei, M.; Shi, J.; Lu, J. Interfacial Properties of Monolayer and Bilayer MoS2 Contacts with Metals: Beyond the Energy Band Calculations. *Sci Rep* **2016**, *6* (1), 21786. https://doi.org/10.1038/srep21786.

(96)   Sze, S. M.; Ng, K. K. *Physics of Semiconductor Devices: Sze/Physics*; John Wiley & Sons, Inc.: Hoboken, NJ, USA, 2006. https://doi.org/10.1002/0470068329.

(97)   Cheng, Y. J.; Yan, L.; Shi, F.; Liu, F.; Li, M.; Shi, H. L.; Hou, Z. P. Monte Carlo Simulation of Electron Scattering in Ion Barrier Film in Generation III Image Intensifier. *KEM* **2013**, *552*, 193–200. https://doi.org/10.4028/www.scientific.net/KEM.552.193.

(98)   Movla, H.; Babazadeh, M. Simulation Analysis of the Aluminum Thin Film Thickness Measurement by Using Low Energy Electron Beam. *Optik* **2014**, *125* (1), 71–74. https://doi.org/10.1016/j.ijleo.2013.06.033.

(99)   Drouin, D.; Couture, A. R.; Joly, D.; Tastet, X.; Aimez, V.; Gauvin, R. CASINO V2.42—A Fast and Easy-to-Use Modeling Tool for Scanning Electron Microscopy and Microanalysis Users. *Scanning* **2007**, *29* (3), 92–101. https://doi.org/10.1002/sca.20000.

(100)   Abraham, M.; Mohney, S. E. Annealed Ag Contacts to MoS$_2$ Field-Effect Transistors. *Journal of Applied Physics* **2017**, *122* (11), 115306. https://doi.org/10.1063/1.4991961.

(101)   Goyal, N.; Mackenzie, D. M. A.; Panchal, V.; Jawa, H.; Kazakova, O.; Petersen, D. H.; Lodha, S. Enhanced Thermally Aided Memory Performance Using Few-Layer ReS$_2$ Transistors. *Appl. Phys. Lett.* **2020**, *116* (5), 052104. https://doi.org/10.1063/1.5126809.

(102)   Di Bartolomeo, A.; Rücker, H.; Schley, P.; Fox, A.; Lischke, S.; Na, K.-Y. A Single-Poly EEPROM Cell for Embedded Memory Applications. *Solid-State Electronics* **2009**, *53* (6), 644–648. https://doi.org/10.1016/j.sse.2009.04.007.

(103) Lam, S.-T. Overview of Field-Emission Information Storage Devices. *J. Vac. Sci. Technol. B* **2003**, *21* (1), 479. https://doi.org/10.1116/1.1541603.

(104) Li, Y.; Sun, Y.; Jaffray, D. A.; Yeow, J. T. W. A Novel Field Emission Microscopy Method to Study Field Emission Characteristics of Freestanding Carbon Nanotube Arrays. *Nanotechnology* **2017**, *28* (15), 155704. https://doi.org/10.1088/1361-6528/aa613e.

(105) Wieland, M. J.; Kampherbeek, B. J.; Addessi, P.; Kruit, P. Field Emission Photocathode Array for Multibeam Electron Lithography. *Microelectronic Engineering* **2001**, *57–58*, 155–161. https://doi.org/10.1016/S0167-9317(01)00507-X.

(106) Talin, A. A.; Dean, K. A.; Jaskie, J. E. Field Emission Displays: A Critical Review. *Solid-State Electronics* **2001**, *45* (6), 963–976. https://doi.org/10.1016/S0038-1101(00)00279-3.

(107) Fursey, G. N. Field Emission in Vacuum Micro-Electronics. *Applied Surface Science* **2003**, *215* (1–4), 113–134. https://doi.org/10.1016/S0169-4332(03)00315-5.

(108) Late, D. J.; Shaikh, P. A.; Khare, R.; Kashid, R. V.; Chaudhary, M.; More, M. A.; Ogale, S. B. Pulsed Laser-Deposited MoS_2 Thin Films on W and Si: Field Emission and Photoresponse Studies. *ACS Appl. Mater. Interfaces* **2014**, *6* (18), 15881–15888. https://doi.org/10.1021/am503464h.

(109) Kashid, R. V.; Late, D. J.; Chou, S. S.; Huang, Y.-K.; De, M.; Joag, D. S.; More, M. A.; Dravid, V. P. Enhanced Field-Emission Behavior of Layered MoS_2 Sheets. *Small* **2013**, *9* (16), 2730–2734. https://doi.org/10.1002/smll.201300002.

(110) Iemmo, L.; Urban, F.; Giubileo, F.; Passacantando, M.; Di Bartolomeo, A. Nanotip Contacts for Electric Transport and Field Emission Characterization of Ultrathin MoS2 Flakes. *Nanomaterials* **2020**, *10* (1), 106. https://doi.org/10.3390/nano10010106.

(111) Di Bartolomeo, A.; Urban, F.; Passacantando, M.; McEvoy, N.; Peters, L.; Iemmo, L.; Luongo, G.; Romeo, F.; Giubileo, F. A WSe_2 Vertical Field Emission Transistor. *Nanoscale* **2019**, *11* (4), 1538–1548. https://doi.org/10.1039/C8NR09068H.

(112) Urban, F.; Giubileo, F.; Grillo, A.; Iemmo, L.; Luongo, G.; Passacantando, M.; Foller, T.; Madauß, L.; Pollmann, E.; Geller, M. P.; Oing, D.; Schleberger, M.; Di Bartolomeo, A. Gas Dependent Hysteresis in MoS_2 Field Effect Transistors. *2D Mater.* **2019**, *6* (4), 045049. https://doi.org/10.1088/2053-1583/ab4020.

(113) Di Bartolomeo, A.; Luongo, G.; Giubileo, F.; Funicello, N.; Niu, G.; Schroeder, T.; Lisker, M.; Lupina, G. Hybrid Graphene/Silicon Schottky Photodiode with Intrinsic Gating Effect. *2D Mater.* **2017**, *4* (2), 025075. https://doi.org/10.1088/2053-1583/aa6aa0.

(114) Hoffman, A. N.; Gu, Y.; Liang, L.; Fowlkes, J. D.; Xiao, K.; Rack, P. D. Exploring the Air Stability of PdSe2 via Electrical Transport Measurements and Defect Calculations. *npj 2D Mater Appl* **2019**, *3* (1), 50. https://doi.org/10.1038/s41699-019-0132-4.

(115) Gong, C.; Colombo, L.; Wallace, R. M.; Cho, K. The Unusual Mechanism of Partial Fermi Level Pinning at Metal–MoS_2 Interfaces. *Nano Lett.* **2014**, *14* (4), 1714–1720. https://doi.org/10.1021/nl403465v.

(116) Di Bartolomeo, A.; Grillo, A.; Urban, F.; Iemmo, L.; Giubileo, F.; Luongo, G.; Amato, G.; Croin, L.; Sun, L.; Liang, S.-J.; Ang, L. K. Asymmetric Schottky Contacts in Bilayer MoS_2 Field Effect Transistors. *Adv. Funct. Mater.* **2018**, *28* (28), 1800657. https://doi.org/10.1002/adfm.201800657.

(117) Kim, C.; Moon, I.; Lee, D.; Choi, M. S.; Ahmed, F.; Nam, S.; Cho, Y.; Shin, H.-J.; Park, S.; Yoo, W. J. Fermi Level Pinning at Electrical Metal Contacts of Monolayer Molybdenum Dichalcogenides. *ACS Nano* **2017**, *11* (2), 1588–1596. https://doi.org/10.1021/acsnano.6b07159.

(118) Liu, D.; Guo, Y.; Fang, L.; Robertson, J. Sulfur Vacancies in Monolayer MoS_2 and Its Electrical Contacts. *Appl. Phys. Lett.* **2013**, *103* (18), 183113. https://doi.org/10.1063/1.4824893.

(119) Urban, F.; Martucciello, N.; Peters, L.; McEvoy, N.; Di Bartolomeo, A. Environmental Effects on the Electrical Characteristics of Back-Gated WSe2 Field-Effect Transistors. *Nanomaterials* **2018**, *8* (11), 901. https://doi.org/10.3390/nano8110901.

(120) Di Bartolomeo, A.; Pelella, A.; Liu, X.; Miao, F.; Passacantando, M.; Giubileo, F.; Grillo, A.; Iemmo, L.; Urban, F.; Liang, S. Pressure-Tunable Ambipolar Conduction and Hysteresis in Thin Palladium Diselenide Field Effect Transistors. *Adv. Funct. Mater.* **2019**, *29* (29), 1902483. https://doi.org/10.1002/adfm.201902483.

(121) Ahn, J.-H.; Parkin, W. M.; Naylor, C. H.; Johnson, A. T. C.; Drndić, M. Ambient Effects on Electrical Characteristics of CVD-Grown Monolayer MoS2 Field-Effect Transistors. *Sci Rep* **2017**, *7* (1), 4075. https://doi.org/10.1038/s41598-017-04350-z.

(122) Czerniak-Łosiewicz, K.; Gertych, A. P.; Świniarski, M.; Judek, J.; Zdrojek, M. Time Dependence of Photocurrent in Chemical Vapor Deposition MoS $_2$ Monolayer—Intrinsic Properties and Environmental Effects. *J. Phys. Chem. C* **2020**, acs.jpcc.0c04452. https://doi.org/10.1021/acs.jpcc.0c04452.

(123) Giubileo, F.; Grillo, A.; Iemmo, L.; Luongo, G.; Urban, F.; Passacantando, M.; Di Bartolomeo, A. Environmental Effects on Transport Properties of PdSe2 Field Effect Transistors. *Materials Today: Proceedings* **2020**, *20*, 50–53. https://doi.org/10.1016/j.matpr.2019.08.226.

(124) Jensen, K. L. Electron Emission Theory and Its Application: Fowler–Nordheim Equation and Beyond. *J. Vac. Sci. Technol. B* **2003**, *21* (4), 1528. https://doi.org/10.1116/1.1573664.

(125) Di Bartolomeo, A.; Scarfato, A.; Giubileo, F.; Bobba, F.; Biasiucci, M.; Cucolo, A. M.; Santucci, S.; Passacantando, M. A Local Field Emission Study of Partially Aligned Carbon-Nanotubes by Atomic Force Microscope Probe. *Carbon* **2007**, *45* (15), 2957–2971. https://doi.org/10.1016/j.carbon.2007.09.049.

(126) Sun, S.; Ang, L. K. Analysis of Nonuniform Field Emission from a Lorentzian or Hyperboloid Shape Emitter. In *2013 Abstracts IEEE International Conference on Plasma Science (ICOPS)*; IEEE: San Francisco, CA, USA, 2013; pp 1–1. https://doi.org/10.1109/PLASMA.2013.6634949.

(127) Chen, E.; Xu, W.; Chen, J.; Warner, J. H. 2D Layered Noble Metal Dichalcogenides (Pt, Pd, Se, S) for Electronics and Energy Applications. *Materials Today Advances* **2020**, *7*, 100076. https://doi.org/10.1016/j.mtadv.2020.100076.

(128) Avsar, A.; Ciarrocchi, A.; Pizzochero, M.; Unuchek, D.; Yazyev, O. V.; Kis, A. Defect Induced, Layer-Modulated Magnetism in Ultrathin Metallic PtSe2. *Nat. Nanotechnol.* **2019**, *14* (7), 674–678. https://doi.org/10.1038/s41565-019-0467-1.

(129) Zhao, Y.; Qiao, J.; Yu, Z.; Yu, P.; Xu, K.; Lau, S. P.; Zhou, W.; Liu, Z.; Wang, X.; Ji, W.; Chai, Y. High-Electron-Mobility and Air-Stable 2D Layered PtSe $_2$ FETs. *Adv. Mater.* **2017**, *29* (5), 1604230. https://doi.org/10.1002/adma.201604230.

(130) Guo, G. Y.; Liang, W. Y. The Electronic Structures of Platinum Dichalcogenides: PtS $_2$, PtSe $_2$ and PtTe $_2$. *J. Phys. C: Solid State Phys.* **1986**, *19* (7), 995–1008. https://doi.org/10.1088/0022-3719/19/7/011.

(131) Zhuang, H. L.; Hennig, R. G. Computational Search for Single-Layer Transition-Metal Dichalcogenide Photocatalysts. *J. Phys. Chem. C* **2013**, *117* (40), 20440–20445. https://doi.org/10.1021/jp405808a.

(132) Wang, Y.; Li, L.; Yao, W.; Song, S.; Sun, J. T.; Pan, J.; Ren, X.; Li, C.; Okunishi, E.; Wang, Y.-Q.; Wang, E.; Shao, Y.; Zhang, Y. Y.; Yang, H.; Schwier, E. F.; Iwasawa, H.; Shimada, K.; Taniguchi, M.; Cheng, Z.; Zhou, S.; Du, S.; Pennycook, S. J.; Pantelides, S. T.; Gao, H.-J. Monolayer PtSe $_2$, a New Semiconducting Transition-Metal-Dichalcogenide, Epitaxially Grown by Direct Selenization of Pt. *Nano Lett.* **2015**, *15* (6), 4013–4018. https://doi.org/10.1021/acs.nanolett.5b00964.

(133) Ansari, L.; Monaghan, S.; McEvoy, N.; Coileáin, C. Ó.; Cullen, C. P.; Lin, J.; Siris, R.; Stimpel-Lindner, T.; Burke, K. F.; Mirabelli, G.; Duffy, R.; Caruso, E.; Nagle, R. E.; Duesberg, G. S.; Hurley, P. K.; Gity, F. Quantum Confinement-Induced Semimetal-to-Semiconductor Evolution in Large-Area Ultra-Thin PtSe2 Films Grown at 400 °C. *npj 2D Mater Appl* **2019**, *3* (1), 33. https://doi.org/10.1038/s41699-019-0116-4.

(134) Zhang, W.; Qin, J.; Huang, Z.; Zhang, W. The Mechanism of Layer Number and Strain Dependent Bandgap of 2D Crystal PtSe $_2$. *Journal of Applied Physics* **2017**, *122* (20), 205701. https://doi.org/10.1063/1.5000419.

(135) Chia, X.; Adriano, A.; Lazar, P.; Sofer, Z.; Luxa, J.; Pumera, M. Layered Platinum Dichalcogenides (PtS $_2$, PtSe $_2$, and PtTe $_2$) Electrocatalysis: Monotonic Dependence on the Chalcogen Size. *Adv. Funct. Mater.* **2016**, *26* (24), 4306–4318. https://doi.org/10.1002/adfm.201505402.

(136) Su, T.-Y.; Medina, H.; Chen, Y.-Z.; Wang, S.-W.; Lee, S.-S.; Shih, Y.-C.; Chen, C.-W.; Kuo, H.-C.; Chuang, F.-C.; Chueh, Y.-L. Phase-Engineered PtSe $_2$ -Layered Films by a Plasma-Assisted Selenization Process toward All PtSe $_2$ -Based Field Effect Transistor to Highly Sensitive, Flexible, and Wide-Spectrum

Photoresponse Photodetectors. *Small* **2018**, *14* (19), 1800032.
https://doi.org/10.1002/smll.201800032.

(137) Yim, C.; Lee, K.; McEvoy, N.; O'Brien, M.; Riazimehr, S.; Berner, N. C.; Cullen, C. P.; Kotakoski, J.; Meyer, J. C.; Lemme, M. C.; Duesberg, G. S. High-Performance Hybrid Electronic Devices from Layered PtSe $_2$ Films Grown at Low Temperature. *ACS Nano* **2016**, *10* (10), 9550–9558. https://doi.org/10.1021/acsnano.6b04898.

(138) Sajjad, M.; Montes, E.; Singh, N.; Schwingenschlögl, U. Superior Gas Sensing Properties of Monolayer PtSe $_2$. *Adv. Mater. Interfaces* **2017**, *4* (5), 1600911. https://doi.org/10.1002/admi.201600911.

(139) Su, T.-Y.; Chen, Y.-Z.; Wang, Y.-C.; Tang, S.-Y.; Shih, Y.-C.; Cheng, F.; Wang, Z. M.; Lin, H.-N.; Chueh, Y.-L. Highly Sensitive, Selective and Stable NO $_2$ Gas Sensors with a Ppb-Level Detection Limit on 2D-Platinum Diselenide Films. *J. Mater. Chem. C* **2020**, *8* (14), 4851–4858. https://doi.org/10.1039/C9TC05747A.

(140) Liang, Q.; Gou, J.; Arramel; Zhang, Q.; Zhang, W.; Wee, A. T. S. Oxygen-Induced Controllable p-Type Doping in 2D Semiconductor Transition Metal Dichalcogenides. *Nano Res.* **2020**, *13* (12), 3439–3444. https://doi.org/10.1007/s12274-020-3038-8.

(141) Yim, C.; Passi, V.; Lemme, M. C.; Duesberg, G. S.; Ó Coileáin, C.; Pallecchi, E.; Fadil, D.; McEvoy, N. Electrical Devices from Top-down Structured Platinum Diselenide Films. *npj 2D Mater Appl* **2018**, *2* (1), 5. https://doi.org/10.1038/s41699-018-0051-9.

(142) Zheng, H.; Choi, Y.; Baniasadi, F.; Hu, D.; Jiao, L.; Park, K.; Tao, C. Visualization of Point Defects in Ultrathin Layered 1T-PtSe $_2$. *2D Mater.* **2019**, *6* (4), 041005. https://doi.org/10.1088/2053-1583/ab3beb.

(143) Smidstrup, S.; Markussen, T.; Vancraeyveld, P.; Wellendorff, J.; Schneider, J.; Gunst, T.; Verstichel, B.; Stradi, D.; Khomyakov, P. A.; Vej-Hansen, U. G.; Lee, M.-E.; Chill, S. T.; Rasmussen, F.; Penazzi, G.; Corsetti, F.; Ojanperä, A.; Jensen, K.; Palsgaard, M. L. N.; Martinez, U.; Blom, A.; Brandbyge, M.; Stokbro, K. QuantumATK: An Integrated Platform of Electronic and Atomic-Scale Modelling Tools. *J. Phys.: Condens. Matter* **2020**, *32* (1), 015901. https://doi.org/10.1088/1361-648X/ab4007.

(144) van Setten, M. J.; Giantomassi, M.; Bousquet, E.; Verstraete, M. J.; Hamann, D. R.; Gonze, X.; Rignanese, G.-M. The PseudoDojo: Training and Grading a 85 Element Optimized Norm-Conserving Pseudopotential Table. *Computer Physics Communications* **2018**, *226*, 39–54. https://doi.org/10.1016/j.cpc.2018.01.012.

(145) Monkhorst, H. J.; Pack, J. D. Special Points for Brillouin-Zone Integrations. *Phys. Rev. B* **1976**, *13* (12), 5188–5192. https://doi.org/10.1103/PhysRevB.13.5188.

(146) Ansari, L.; Fagas, G.; Gity, F.; Greer, J. C. A Sub k $_B$ T/q Semimetal Nanowire Field Effect Transistor. *Appl. Phys. Lett.* **2016**, *109* (6), 063108. https://doi.org/10.1063/1.4960709.

(147) Dion, M.; Rydberg, H.; Schröder, E.; Langreth, D. C.; Lundqvist, B. I. Van Der Waals Density Functional for General Geometries. *Phys. Rev. Lett.* **2004**, *92* (24), 246401. https://doi.org/10.1103/PhysRevLett.92.246401.

(148) Neugebauer, J.; Scheffler, M. Adsorbate-Substrate and Adsorbate-Adsorbate Interactions of Na and K Adlayers on Al(111). *Phys. Rev. B* **1992**, *46* (24), 16067–16080. https://doi.org/10.1103/PhysRevB.46.16067.

(149) Gong, Y.; Lin, Z.; Chen, Y.-X.; Khan, Q.; Wang, C.; Zhang, B.; Nie, G.; Xie, N.; Li, D. Two-Dimensional Platinum Diselenide: Synthesis, Emerging Applications, and Future Challenges. *Nano-Micro Lett.* **2020**, *12* (1), 174. https://doi.org/10.1007/s40820-020-00515-0.

(150) Zhang, Z.-X.; Long-Hui Zeng; Tong, X.-W.; Gao, Y.; Xie, C.; Tsang, Y. H.; Luo, L.-B.; Wu, Y.-C. Ultrafast, Self-Driven, and Air-Stable Photodetectors Based on Multilayer PtSe $_2$ /Perovskite Heterojunctions. *J. Phys. Chem. Lett.* **2018**, *9* (6), 1185–1194. https://doi.org/10.1021/acs.jpclett.8b00266.

(151) Urban, F.; Gity, F.; Hurley, P. K.; McEvoy, N.; Di Bartolomeo, A. Isotropic Conduction and Negative Photoconduction in Ultrathin PtSe $_2$ Films. *Appl. Phys. Lett.* **2020**, *117* (19), 193102. https://doi.org/10.1063/5.0021009.

(152) Giannazzo, F.; Fisichella, G.; Piazza, A.; Di Franco, S.; Greco, G.; Agnello, S.; Roccaforte, F. Impact of Contact Resistance on the Electrical Properties of MoS $_2$ Transistors at Practical Operating Temperatures. *Beilstein J. Nanotechnol.* **2017**, *8*, 254–263. https://doi.org/10.3762/bjnano.8.28.

(153) Jiang, J.; Ling, C.; Xu, T.; Wang, W.; Niu, X.; Zafar, A.; Yan, Z.; Wang, X.; You, Y.; Sun, L.; Lu, J.; Wang, J.; Ni, Z. Defect Engineering for Modulating the Trap States in 2D Photoconductors. *Adv. Mater.* **2018**, *30* (40), 1804332. https://doi.org/10.1002/adma.201804332.

(154) Shen, W.-C.; Chen, R.-S.; Huang, Y.-S. Photoconductivities in MoS2 Nanoflake Photoconductors. *Nanoscale Res Lett* **2016**, *11* (1), 124. https://doi.org/10.1186/s11671-016-1331-y.

(155) Kang, M.-A.; Kim, S.; Jeon, I.-S.; Lim, Y. R.; Park, C.-Y.; Song, W.; Lee, S. S.; Lim, J.; An, K.-S.; Myung, S. Highly Efficient and Flexible Photodetector Based on MoS $_2$ –ZnO Heterostructures. *RSC Adv.* **2019**, *9* (34), 19707–19711. https://doi.org/10.1039/C9RA00578A.

(156) Liu, E.; Long, M.; Zeng, J.; Luo, W.; Wang, Y.; Pan, Y.; Zhou, W.; Wang, B.; Hu, W.; Ni, Z.; You, Y.; Zhang, X.; Qin, S.; Shi, Y.; Watanabe, K.; Taniguchi, T.; Yuan, H.; Hwang, H. Y.; Cui, Y.; Miao, F.; Xing, D. High Responsivity Phototransistors Based on Few-Layer ReS $_2$ for Weak Signal Detection. *Adv. Funct. Mater.* **2016**, *26* (12), 1938–1944. https://doi.org/10.1002/adfm.201504408.

(157) Wang, Y.; Yu, Z.; Tong, Y.; Sun, B.; Zhang, Z.; Xu, J.-B.; Sun, X.; Tsang, H. K. High-Speed Infrared Two-Dimensional Platinum Diselenide Photodetectors. *Appl. Phys. Lett.* **2020**, *116* (21), 211101. https://doi.org/10.1063/5.0010034.

(158) Yu, Z.; Wang, Y.; Sun, B.; Tong, Y.; Xu, J.; Tsang, H. K.; Sun, X. Hybrid 2D-Material Photonics with Bound States in the Continuum. *Adv. Optical Mater.* **2019**, *7* (24), 1901306. https://doi.org/10.1002/adom.201901306.

(159) Li, L.; Wang, W.; Chai, Y.; Li, H.; Tian, M.; Zhai, T. Few-Layered PtS $_2$ Phototransistor on h-BN with High Gain. *Adv. Funct. Mater.* **2017**, *27* (27), 1701011. https://doi.org/10.1002/adfm.201701011.

(160) Furchi, M.; Urich, A.; Pospischil, A.; Lilley, G.; Unterrainer, K.; Detz, H.; Klang, P.; Andrews, A. M.; Schrenk, W.; Strasser, G.; Mueller, T. Microcavity-Integrated Graphene Photodetector. *Nano Lett.* **2012**, *12* (6), 2773–2777. https://doi.org/10.1021/nl204512x.

(161) Huang, M.; Wang, M.; Chen, C.; Ma, Z.; Li, X.; Han, J.; Wu, Y. Broadband Black-Phosphorus Photodetectors with High Responsivity. *Adv. Mater.* **2016**, *28* (18), 3481–3485. https://doi.org/10.1002/adma.201506352.

(162) Liu, G. Z.; Zhao, R.; Qiu, J.; Jiang, Y. C.; Gao, J. Negative Photoconductivity under Visible Light Illumination in LaAlO $_3$ /SrTiO $_3$ Heterostructures. *J. Phys. D: Appl. Phys.* **2019**, *52* (9), 095302. https://doi.org/10.1088/1361-6463/aaf8f6.

(163) Zhang, Y.; Li, X.; Lin, X.; Li, G.; Cai, Y.; Wen, C.; Wang, K.; Liu, D.; Hu, S.; Hu, Y. Negative Photoconductivity in Sulfur-Hyperdoped Silicon Film. *Materials Science in Semiconductor Processing* **2019**, *98*, 106–112. https://doi.org/10.1016/j.mssp.2019.04.002.

(164) Xiao, X.; Li, J.; Wu, J.; Lu, D.; Tang, C. Negative Photoconductivity Observed in Polycrystalline Monolayer Molybdenum Disulfide Prepared by Chemical Vapor Deposition. *Appl. Phys. A* **2019**, *125* (11), 765. https://doi.org/10.1007/s00339-019-3054-2.

(165) Han, Y.; Zheng, X.; Fu, M.; Pan, D.; Li, X.; Guo, Y.; Zhao, J.; Chen, Q. Negative Photoconductivity of InAs Nanowires. *Phys. Chem. Chem. Phys.* **2016**, *18* (2), 818–826. https://doi.org/10.1039/C5CP06139C.

(166) Liu, Y.; Fu, P.; Yin, Y.; Peng, Y.; Yang, W.; Zhao, G.; Wang, W.; Zhou, W.; Tang, D. Positive and Negative Photoconductivity Conversion Induced by H2O Molecule Adsorption in WO3 Nanowire. *Nanoscale Res Lett* **2019**, *14* (1), 144. https://doi.org/10.1186/s11671-019-2978-y.

(167) Wang, Y.; He, Z.; Zhang, J.; Liu, H.; Lai, X.; Liu, B.; Chen, Y.; Wang, F.; Zhang, L. UV Illumination Enhanced Desorption of Oxygen Molecules from Monolayer MoS2 Surface. *Nano Res.* **2020**, *13* (2), 358–365. https://doi.org/10.1007/s12274-020-2614-2.

(168) Han, P.; Adler, E. R.; Liu, Y.; St Marie, L.; El Fatimy, A.; Melis, S.; Van Keuren, E.; Barbara, P. Ambient Effects on Photogating in MoS $_2$ Photodetectors. *Nanotechnology* **2019**, *30* (28), 284004. https://doi.org/10.1088/1361-6528/ab149e.

(169) Lee, C.-C.; Yamada-Takamura, Y.; Ozaki, T. Unfolding Method for First-Principles LCAO Electronic Structure Calculations. *J. Phys.: Condens. Matter* **2013**, *25* (34), 345501. https://doi.org/10.1088/0953-8984/25/34/345501.

(170) Gity, F.; Meaney, F.; Curran, A.; Hurley, P. K.; Fahy, S.; Duffy, R.; Ansari, L. Doping of Ultra-Thin Si Films: Combined First-Principles Calculations and Experimental Study. *Journal of Applied Physics* **2021**, *129* (1), 015701. https://doi.org/10.1063/5.0035693.

(171) Ijaz, M.; Ghassemlooy, Z.; Rajbhandari, S.; Minh, H. L.; Perez, J.; Gholami, A. Comparison of 830 Nm and 1550 Nm Based Free Space Optical Communications Link under Controlled Fog Conditions. In *2012 8th International Symposium on Communication Systems, Networks Digital Signal Processing (CSNDSP)*; 2012; pp 1–5. https://doi.org/10.1109/CSNDSP.2012.6292739.

(172) Wang, J.; Xing, Z.; Chen, X.; Cheng, Z.; Li, X.; Liu, T. Recent Progress in Waveguide-Integrated Graphene Photonic Devices for Sensing and Communication Applications. *Front. Phys.* **2020**, *8*, 37. https://doi.org/10.3389/fphy.2020.00037.

(173) Zhou, H.; Zhu, X.; Gu, T.; Wu, J.; Deng, G.; Huang, S.-W.; Ophir, N.; Yu, M.; Kwong, D.-L.; Zhou, S.; Bergman, K.; Wong, C. W. Error-Free Data Transmission through Fast Broadband All-Optical Modulation in Graphene–Silicon Optoelectronics. *Appl. Phys. Lett.* **2020**, *116* (22), 221106. https://doi.org/10.1063/5.0006596.

(174) Blackett, M. An Overview of Infrared Remote Sensing of Volcanic Activity. *J. Imaging* **2017**, *3* (2), 13. https://doi.org/10.3390/jimaging3020013.

(175) Goddijn-Murphy, L.; Williamson, B. On Thermal Infrared Remote Sensing of Plastic Pollution in Natural Waters. *Remote Sensing* **2019**, *11* (18), 2159. https://doi.org/10.3390/rs11182159.

(176) Hua, L.; Shao, G. The Progress of Operational Forest Fire Monitoring with Infrared Remote Sensing. *J. For. Res.* **2017**, *28* (2), 215–229. https://doi.org/10.1007/s11676-016-0361-8.

(177) Geim, A. K. Graphene: Status and Prospects. *Science* **2009**, *324* (5934), 1530–1534. https://doi.org/10.1126/science.1158877.

(178) Wang, J.; Mu, X.; Sun, M.; Mu, T. Optoelectronic Properties and Applications of Graphene-Based Hybrid Nanomaterials and van Der Waals Heterostructures. *Applied Materials Today* **2019**, *16*, 1–20. https://doi.org/10.1016/j.apmt.2019.03.006.

(179) Luo, F.; Zhu, M.; tan, Y.; Sun, H.; Luo, W.; Peng, G.; Zhu, Z.; Zhang, X.-A.; Qin, S. High Responsivity Graphene Photodetectors from Visible to Near-Infrared by Photogating Effect. *AIP Advances* **2018**, *8* (11), 115106. https://doi.org/10.1063/1.5054760.

(180) Urban, F.; Lupina, G.; Grillo, A.; Martucciello, N.; Di Bartolomeo, A. Contact Resistance and Mobility in Back-Gate Graphene Transistors. *Nano Express* **2020**, *1* (1), 010001. https://doi.org/10.1088/2632-959X/ab7055.

(181) Di Bartolomeo, A. Graphene Schottky Diodes: An Experimental Review of the Rectifying Graphene/Semiconductor Heterojunction. *Physics Reports* **2016**, *606*, 1–58. https://doi.org/10.1016/j.physrep.2015.10.003.

(182) Liang, S.-J.; Ang, L. K. Electron Thermionic Emission from Graphene and a Thermionic Energy Converter. *Phys. Rev. Applied* **2015**, *3* (1), 014002. https://doi.org/10.1103/PhysRevApplied.3.014002.

(183) Casalino, M.; Sassi, U.; Goykhman, I.; Eiden, A.; Lidorikis, E.; Milana, S.; De Fazio, D.; Tomarchio, F.; Iodice, M.; Coppola, G.; Ferrari, A. C. Vertically Illuminated, Resonant Cavity Enhanced, Graphene– Silicon Schottky Photodetectors. *ACS Nano* **2017**, *11* (11), 10955–10963. https://doi.org/10.1021/acsnano.7b04792.

(184) Alvarado Chavarin, C.; Strobel, C.; Kitzmann, J.; Di Bartolomeo, A.; Lukosius, M.; Albert, M.; Bartha, J.; Wenger, C. Current Modulation of a Heterojunction Structure by an Ultra-Thin Graphene Base Electrode. *Materials* **2018**, *11* (3), 345. https://doi.org/10.3390/ma11030345.

(185) Casalino, M.; Crisci, T.; Moretti, L.; Gioffre, M.; Iodice, M.; Coppola, G.; Maccagnani, P.; Rizzoli, R.; Bonafe, F.; Summonte, C.; Morandi, V. Silicon Meet Graphene for a New Family of Near-Infrared Resonant Cavity Enhanced Photodetectors. In *2020 22nd International Conference on Transparent Optical Networks (ICTON)*; IEEE: Bari, Italy, 2020; pp 1–4. https://doi.org/10.1109/ICTON51198.2020.9203222.

(186) Di Bartolomeo, A.; Luongo, G.; iemmo, L.; Urban, F.; Giubileo, F. Graphene–Silicon Schottky Diodes for Photodetection. *IEEE Trans. Nanotechnology* **2018**, *17* (6), 1133–1137. https://doi.org/10.1109/TNANO.2018.2853798.

(187) Wu, H.-Q.; Linghu, C.-Y.; Lu, H.-M.; Qian, H. Graphene Applications in Electronic and Optoelectronic Devices and Circuits. *Chinese Physics B* **2013**, *22*, 098106. https://doi.org/10.1088/1674-1056/22/9/098106.

(188) Hong, S. K.; Kim, C. S.; Hwang, W. S.; Cho, B. J. Hybrid Integration of Graphene Analog and Silicon Complementary Metal–Oxide–Semiconductor Digital Circuits. *ACS Nano* **2016**, *10* (7), 7142–7146. https://doi.org/10.1021/acsnano.6b03382.

(189) Luongo, G.; Grillo, A.; Giubileo, F.; Iemmo, L.; Lukosius, M.; Alvarado Chavarin, C.; Wenger, C.; Di Bartolomeo, A. Graphene Schottky Junction on Pillar Patterned Silicon Substrate. *Nanomaterials* **2019**, *9* (5), 659. https://doi.org/10.3390/nano9050659.

(190) Luongo, G.; Giubileo, F.; Genovese, L.; Iemmo, L.; Martucciello, N.; Di Bartolomeo, A. I-V and C-V Characterization of a High-Responsivity Graphene/Silicon Photodiode with Embedded MOS Capacitor. *Nanomaterials* **2017**, *7* (7), 158. https://doi.org/10.3390/nano7070158.

(191) Riazimehr, S.; Kataria, S.; Bornemann, R.; Haring Bolívar, P.; Ruiz, F. J. G.; Engström, O.; Godoy, A.; Lemme, M. C. High Photocurrent in Gated Graphene–Silicon Hybrid Photodiodes. *ACS Photonics* **2017**, *4* (6), 1506–1514. https://doi.org/10.1021/acsphotonics.7b00285.

(192) Luongo, G.; Di Bartolomeo, A.; Giubileo, F.; Chavarin, C. A.; Wenger, C. Electronic Properties of Graphene/p-Silicon Schottky Junction. *J. Phys. D: Appl. Phys.* **2018**, *51* (25), 255305. https://doi.org/10.1088/1361-6463/aac562.

(193) Riazimehr, S.; Belete, M.; Kataria, S.; Engström, O.; Lemme, M. C. Capacitance–Voltage (C–V) Characterization of Graphene–Silicon Heterojunction Photodiodes. *Advanced Optical Materials* **2020**, *8* (13), 2000169. https://doi.org/10.1002/adom.202000169.

(194) Riazimehr, S.; Bablich, A.; Schneider, D.; Kataria, S.; Passi, V.; Yim, C.; Duesberg, G. S.; Lemme, M. C. Spectral Sensitivity of Graphene/Silicon Heterojunction Photodetectors. *Solid-State Electronics* **2016**, *115*, 207–212. https://doi.org/10.1016/j.sse.2015.08.023.

(195) Riazimehr, S.; Kataria, S.; Gonzalez-Medina, J. M.; Wagner, S.; Shaygan, M.; Suckow, S.; Ruiz, F. G.; Engström, O.; Godoy, A.; Lemme, M. C. High Responsivity and Quantum Efficiency of Graphene/Silicon Photodiodes Achieved by Interdigitating Schottky and Gated Regions. *ACS Photonics* **2019**, *6* (1), 107–115. https://doi.org/10.1021/acsphotonics.8b00951.

(196) Tyagi, M. S. Physics of Schottky Barrier Junctions. In *Metal-Semiconductor Schottky Barrier Junctions and Their Applications*; Sharma, B. L., Ed.; Springer US: Boston, MA, 1984; pp 1–60. https://doi.org/10.1007/978-1-4684-4655-5_1.

(197) Mönch, W. Barrier Heights of Real Schottky Contacts Explained by Metal-Induced Gap States and Lateral Inhomogeneities. *Journal of Vacuum Science & Technology B: Microelectronics and Nanometer Structures Processing, Measurement, and Phenomena* **1999**, *17* (4), 1867–1876. https://doi.org/10.1116/1.590839.

(198) Neetika; Kumar, S.; Sanger, A.; Chourasiya, H. K.; Kumar, A.; Asokan, K.; Chandra, R.; Malik, V. K. Influence of Barrier Inhomogeneities on Transport Properties of Pt/MoS2 Schottky Barrier Junction. *Journal of Alloys and Compounds* **2019**, *797*, 582–588. https://doi.org/10.1016/j.jallcom.2019.05.028.

(199) Cheung, S. K.; Cheung, N. W. Extraction of Schottky Diode Parameters from Forward Current-voltage Characteristics. *Appl. Phys. Lett.* **1986**, *49* (2), 85–87. https://doi.org/10.1063/1.97359.

(200) Bartolomeo, A. D.; Giubileo, F.; Luongo, G.; Iemmo, L.; Martucciello, N.; Niu, G.; Fraschke, M.; Skibitzki, O.; Schroeder, T.; Lupina, G. Tunable Schottky Barrier and High Responsivity in Graphene/Si-Nanotip Optoelectronic Device. *2D Mater.* **2016**, *4* (1), 015024. https://doi.org/10.1088/2053-1583/4/1/015024.

(201) Tomer, D.; Rajput, S.; Hudy, L. J.; Li, C. H.; Li, L. Inhomogeneity in Barrier Height at Graphene/Si (GaAs) Schottky Junctions. *Nanotechnology* **2015**, *26* (21), 215702. https://doi.org/10.1088/0957-4484/26/21/215702.

(202) Werner, J. H.; Güttler, H. H. Barrier Inhomogeneities at Schottky Contacts. *Journal of Applied Physics* **1991**, *69* (3), 1522–1533. https://doi.org/10.1063/1.347243.

(203) Parui, S.; Ruiter, R.; Zomer, P. J.; Wojtaszek, M.; van Wees, B. J.; Banerjee, T. Temperature Dependent Transport Characteristics of Graphene/n-Si Diodes. *Journal of Applied Physics* **2014**, *116* (24), 244505. https://doi.org/10.1063/1.4905110.

(204) Shi, E.; Li, H.; Yang, L.; Zhang, L.; Li, Z.; Li, P.; Shang, Y.; Wu, S.; Li, X.; Wei, J.; Wang, K.; Zhu, H.; Wu, D.; Fang, Y.; Cao, A. Colloidal Antireflection Coating Improves Graphene–Silicon Solar Cells. *Nano Lett.* **2013**, *13* (4), 1776–1781. https://doi.org/10.1021/nl400353f.

(205) Wang, C.; Dong, Y.; Lu, Z.; Chen, S.; Xu, K.; Ma, Y.; Xu, G.; Zhao, X.; Yu, Y. High Responsivity and High-Speed 1.55 Mm Infrared Photodetector from Self-Powered Graphene/Si Heterojunction. *Sensors and Actuators A: Physical* **2019**, *291*, 87–92. https://doi.org/10.1016/j.sna.2019.03.054.

(206) Riazimehr, S.; Bablich, A.; Schneider, D.; Kataria, S.; Passi, V.; Yim, C.; Duesberg, G. S.; Lemme, M. C. Spectral Sensitivity of Graphene/Silicon Heterojunction Photodetectors. *Solid-State Electronics* **2016**, *115*, 207–212. https://doi.org/10.1016/j.sse.2015.08.023.

(207) Riazimehr, S.; Kataria, S.; Gonzalez-Medina, J. M.; Wagner, S.; Shaygan, M.; Suckow, S.; Ruiz, F. G.; Engström, O.; Godoy, A.; Lemme, M. C. High Responsivity and Quantum Efficiency of Graphene/Silicon Photodiodes Achieved by Interdigitating Schottky and Gated Regions. *ACS Photonics* **2019**, *6* (1), 107–115. https://doi.org/10.1021/acsphotonics.8b00951.

(208) Tang, Y.; Chen, J. High Responsivity of Gr/ n-Si Schottky Junction near-Infrared Photodetector. *Superlattices and Microstructures* **2021**, *150*, 106803. https://doi.org/10.1016/j.spmi.2021.106803.

(209) *High Efficiency Graphene Solar Cells by Chemical Doping | Nano Letters*. https://pubs.acs.org/doi/pdf/10.1021/nl204414u (accessed 2021-05-05).

(210) Feng, S.; Dong, B.; Lu, Y.; Yin, L.; Wei, B.; Wang, J.; Lin, S. Graphene/p-AlGaN/p-GaN Electron Tunneling Light Emitting Diodes with High External Quantum Efficiency. *Nano Energy* **2019**, *60*, 836–840. https://doi.org/10.1016/j.nanoen.2019.04.007.

(211) Ruan, K.; Ding, K.; Wang, Y.; Diao, S.; Shao, Z.; Zhang, X.; Jie, J. Flexible Graphene/Silicon Heterojunction Solar Cells. *J. Mater. Chem. A* **2015**, *3* (27), 14370–14377. https://doi.org/10.1039/C5TA03652F.

(212) Wang, Y.; Yang, S.; Lambada, D. R.; Shafique, S. A Graphene-Silicon Schottky Photodetector with Graphene Oxide Interlayer. *Sensors and Actuators A: Physical* **2020**, *314*, 112232. https://doi.org/10.1016/j.sna.2020.112232.

(213) Fidan, M.; Ünverdi, Ö.; Çelebi, C. Junction Area Dependent Performance of Graphene/Silicon Based Self-Powered Schottky Photodiodes. *Sensors and Actuators A: Physical* **2021**, *331*, 112829. https://doi.org/10.1016/j.sna.2021.112829.

(214) Di Bartolomeo, A.; Yang, Y.; Rinzan, M. B. M.; Boyd, A. K.; Barbara, P. Record Endurance for Single-Walled Carbon Nanotube–Based Memory Cell. *Nanoscale Research Letters* **2010**, *5* (11), 1852. https://doi.org/10.1007/s11671-010-9727-6.

(215) Melisi, D.; Nitti, M. A.; Valentini, M.; Valentini, A.; Ligonzo, T.; Pascali, G. D.; Ambrico, M. Photodetectors Based on Carbon Nanotubes Deposited by Using a Spray Technique on Semi-Insulating Gallium Arsenide. *Beilstein J. Nanotechnol.* **2014**, *5* (1), 1999–2006. https://doi.org/10.3762/bjnano.5.208.

(216) Tinti, A.; Righetti, F.; Ligonzo, T.; Valentini, A.; Nappi, E.; Ambrosio, A.; Ambrosio, M.; Aramo, C.; Maddalena, P.; Castrucci, P.; Scarselli, M.; De Crescenzi, M.; Fiandrini, E.; Grossi, V.; Santucci, S.; Passacantando, M. Electrical Analysis of Carbon Nanostructures/Silicon Heterojunctions Designed for Radiation Detection. *Nuclear Instruments and Methods in Physics Research Section A: Accelerators, Spectrometers, Detectors and Associated Equipment* **2011**, *629* (1), 377–381. https://doi.org/10.1016/j.nima.2010.11.097.

(217) Passacantando, M.; Bussolotti, F.; Grossi, V.; Santucci, S.; Ambrosio, A.; Ambrosio, M.; Ambrosone, G.; Carillo, V.; Coscia, U.; Maddalena, P.; Perillo, E.; Raulo, A. Photoconductivity in Defective Carbon Nanotube Sheets under Ultraviolet–Visible–near Infrared Radiation. *Appl. Phys. Lett.* **2008**, *93* (5), 051911. https://doi.org/10.1063/1.2968203.

(218) Passacantando, M.; Grossi, V.; Santucci, S. High Photocurrent from Planar Strips of Vertical and Horizontal Aligned Multi Wall Carbon Nanotubes. *Appl. Phys. Lett.* **2012**, *100* (16), 163119. https://doi.org/10.1063/1.4704569.

(219) Di Bartolomeo, A. Graphene Schottky Diodes: An Experimental Review of the Rectifying Graphene/Semiconductor Heterojunction. *Physics Reports* **2016**, *606*, 1–58. https://doi.org/10.1016/j.physrep.2015.10.003.

(220) Scagliotti, M.; Salvato, M.; Frezza, F.; Catone, D.; Di Mario, L.; Boscardin, M.; De Crescenzi, M.; Castrucci, P. Carbon Nanotube Film/Silicon Heterojunction Photodetector for New Cutting-Edge Technological Devices. *Applied Sciences* **2021**, *11* (2), 606. https://doi.org/10.3390/app11020606.

(221) Hu, X.; Hou, P.; Liu, C.; Cheng, H. Carbon Nanotube/Silicon Heterojunctions for Photovoltaic Applications. *Nano Materials Science* **2019**, *1* (3), 156–172. https://doi.org/10.1016/j.nanoms.2019.03.001.

(222) Di Bartolomeo, A.; Giubileo, F.; Grillo, A.; Luongo, G.; Iemmo, L.; Urban, F.; Lozzi, L.; Capista, D.; Nardone, M.; Passacantando, M. Bias Tunable Photocurrent in Metal-Insulator-Semiconductor Heterostructures with Photoresponse Enhanced by Carbon Nanotubes. *Nanomaterials* **2019**, *9* (11), 1598. https://doi.org/10.3390/nano9111598.

(223) Bartolomeo, A. D.; Luongo, G.; Giubileo, F.; Funicello, N.; Niu, G.; Schroeder, T.; Lisker, M.; Lupina, G. Hybrid Graphene/Silicon Schottky Photodiode with Intrinsic Gating Effect. *2D Mater.* **2017**, *4* (2), 025075. https://doi.org/10.1088/2053-1583/aa6aa0.

(224) Riazimehr, S.; Kataria, S.; Bornemann, R.; Haring Bolívar, P.; Ruiz, F. J. G.; Engström, O.; Godoy, A.; Lemme, M. C. High Photocurrent in Gated Graphene–Silicon Hybrid Photodiodes. *ACS Photonics* **2017**, *4* (6), 1506–1514. https://doi.org/10.1021/acsphotonics.7b00285.

(225) Luongo, G.; Bartolomeo, A. D.; Giubileo, F.; Chavarin, C. A.; Wenger, C. Electronic Properties of Graphene/p-Silicon Schottky Junction. *J. Phys. D: Appl. Phys.* **2018**, *51* (25), 255305. https://doi.org/10.1088/1361-6463/aac562.

(226) Ouyang, W.; Teng, F.; He, J.-H.; Fang, X. Enhancing the Photoelectric Performance of Photodetectors Based on Metal Oxide Semiconductors by Charge-Carrier Engineering. *Advanced Functional Materials* **2019**, *29* (9), 1807672. https://doi.org/10.1002/adfm.201807672.

(227) Jia, Y.; Cao, A.; Kang, F.; Li, P.; Gui, X.; Zhang, L.; Shi, E.; Wei, J.; Wang, K.; Zhu, H.; Wu, D. Strong and Reversible Modulation of Carbon Nanotube–Silicon Heterojunction Solar Cells by an Interfacial Oxide Layer. *Phys. Chem. Chem. Phys.* **2012**, *14* (23), 8391–8396. https://doi.org/10.1039/C2CP23639G.

(228) Filatzikioti, A.; Glezos, N.; Kantarelou, V.; Kyriakis, A.; Pilatos, G.; Romanos, G.; Speliotis, T.; Stathopoulou, D. J. Carbon Nanotube Schottky Type Photodetectors for UV Applications. *Solid-State Electronics* **2019**, *151*, 27–35. https://doi.org/10.1016/j.sse.2018.10.018.

(229) Shah, K. A.; Parvaiz, M. S.; Dar, G. N.; Misra, P. Carbon Nanotube Logic Gates: An Interplay of Spin and Light. *Journal of Applied Physics* **2022**, *131* (20), 204301. https://doi.org/10.1063/5.0090951.

(230) Kim, Y. L.; Jung, H. Y.; Park, S.; Li, B.; Liu, F.; Hao, J.; Kwon, Y.-K.; Jung, Y. J.; Kar, S. Voltage-Switchable Photocurrents in Single-Walled Carbon Nanotube–Silicon Junctions for Analog and Digital Optoelectronics. *Nature Photon* **2014**, *8* (3), 239–243. https://doi.org/10.1038/nphoton.2014.1.

(231) Capista, D.; Passacantando, M.; Lozzi, L.; Faella, E.; Giubileo, F.; Di Bartolomeo, A. Easy Fabrication of Performant SWCNT-Si Photodetector. *Electronics* **2022**, *11*, 271. https://doi.org/10.3390/electronics11020271.

(232) Buyukbas-Ulusan, A.; Tataroglu, A. Electrical Characterization of Silicon Nitride Interlayer-Based MIS Diode. *J Mater Sci: Mater Electron* **2020**, *31* (12), 9888–9893. https://doi.org/10.1007/s10854-020-03533-1.

(233) Pür, F. Z.; Tataroğlu, A. Analysis of the Series Resistance and Interface States of Au/Si$_3$N$_4$/n-Si (Metal–Insulator–Semiconductor) Schottky Diodes Using $I–V$ characteristics in a Wide Temperature Range. *Phys. Scr.* **2012**, *86* (3), 035802. https://doi.org/10.1088/0031-8949/86/03/035802.

(234) Yigiterol, F.; Güllü, H. H.; Bayraklı, Ö.; Yıldız, D. E. Temperature-Dependent Electrical Characteristics of Au/Si3N4/4H n-SiC MIS Diode. *J. Electron. Mater.* **2018**, *47* (5), 2979–2987. https://doi.org/10.1007/s11664-018-6155-3.

(235) Grillo, A.; Passacantando, M.; Zak, A.; Pelella, A.; Di Bartolomeo, A. WS2 Nanotubes: Electrical Conduction and Field Emission Under Electron Irradiation and Mechanical Stress. *Small* **2020**, *16* (35), 2002880. https://doi.org/10.1002/smll.202002880.

(236) Ertürk, K.; Bektöre, Y.; Cüneyt Haciismailoglu, M. Electrical and Schottky Contact Properties of Pt/n-Si1–XGex/n-Si(100) Heterostructure. *physica status solidi (c)* **2005**, *2* (4), 1428–1432. https://doi.org/10.1002/pssc.200460480.

(237) Tataroğlu, A.; Pür, F. Z. The Richardson Constant and Barrier Inhomogeneity at Au/Si$\less$sub$\greater$3$\less$/Sub$\greater$N$\less$sub$\greater$4$\less$/Sub$\greater$/n-Si (MIS) Schottky Diodes. *Phys. Scr.* **2013**, *88* (1), 015801. https://doi.org/10.1088/0031-8949/88/01/015801.

(238) Werner, J. H.; Güttler, H. H. Barrier Inhomogeneities at Schottky Contacts. *Journal of Applied Physics* **1991**, *69* (3), 1522–1533. https://doi.org/10.1063/1.347243.

(239) Salvato, M.; Scagliotti, M.; Crescenzi, M. D.; Crivellari, M.; Prosposito, P.; Cacciotti, I.; Castrucci, P. Single Walled Carbon Nanotube/Si Heterojunctions for High Responsivity Photodetectors. *Nanotechnology* **2017**, *28* (43), 435201. https://doi.org/10.1088/1361-6528/aa8797.

(240) Shin, D. H.; Choi, S.-H. Graphene-Based Semiconductor Heterostructures for Photodetectors. *Micromachines* **2018**, *9* (7), 350. https://doi.org/10.3390/mi9070350.